TECHNISCHE UNIVERSITÄT BERLIN

Non-invasive Depth Recovery for *in vivo* Optical Imaging

von
Dipl.-Phys. Sophie Käthe Piper, geb. Schuster
geboren am 23. März 1982 in Berlin

Von der Fakultät IV - Elektrotechnik und Informatik der Technischen Universität Berlin zur Erlangung des akademischen Grades Doktor der Naturwissenschaften - *Dr. rer. nat.* - genehmigte Dissertation in Zusammenarbeit mit der Charité Universitätsmedizin Berlin.

Promotionsausschuss:

Vorsitzender:	Prof. Dr. B. Blankertz
Gutachter:	Prof. Dr. K.-R. Müller
	Prof. Dr. H. Obrig
	Dr. J. Steinbrink

Tag der wissenschaftlichen Aussprache: 2. Juni 2014
Berlin 2014
D 83

To the ones I love and cherish.

Abstract

Clinicians as well as biomedical researchers, who care for the detection of disease progression or the monitoring of responses to therapeutic intervention over time, desire a non-invasive, longitudinal visualization method for physiological and pathophysiological processes inside the living object. Optical microscopic techniques including fluorescence imaging, which use safe (non-ionizing) light, already fulfil this desire when imaging tissue slices of a few µm thickness *in vitro* or invasively *in vivo*. However, when translated to non-invasive measurements in humans or animals, scattering and absorption of light in tissue have been major obstacles when the region of interest is more than 1 mm in depth. My research aimed to improve *in vivo* optical imaging to allow for recovering and visualizing information of tissue in several mm to cm depth. Three physical principles have been investigated to achieve this aim, making use of (i) multiple excitation wavelengths with different penetration depths, (ii) time-resolved measurements that principally allow for depth ranging by measuring the time of flight of photons in tissue, and (iii) optical tomography which incorporates multiple source and detector sites to yield a three-dimensional image reconstruction.

With the first approach (i) of multiple excitation wavelengths, a surface-stripping algorithm was developed enabling the visualisation of focal targets located 4-8 mm deep inside tissue which would have escaped conventional fluorescence reflectance imaging. The method was verified by computer simulations, corresponding phantom experiments as well as *in vivo* measurements. The area of infarction within the living small animal model of stroke was detectable even when fluorescence from the overlying well-perfused intact scalp and skull outweighed the signal of interest.

While approach (i) derives depth-weighted images by reducing the non-target signal from superficial layers, absolute quantification of the target's depth is not possible. However, when detecting the time of flight which fluorescence photons have travelled through tissue with specialised fast electronics (ii), the depth of a focal fluorescent target in planar *in vivo* small animal imaging can be determined explicitly. Computer simulations showed that within the dimensions of a small animal the depth of a fluorescence object can be recovered with an accuracy of $\pm$ 2 mm. Moreover, the results suggest that depth ranging is also feasible in the presence of unspecific background fluorescence which cannot be neglected in *in vivo* imaging.

With the third approach (iii) not only depth but complete tomographic images were obtained in a clinical pilot study on dynamic contrast-enhanced optical mammography in 22 patients. The reconstructed volume time series were used to derive perfusion related parameters for the detection and characterization of breast occupying lesions in the depth of tissue with high sensitivity (85.7%) and specificity (87.5%). In breast cancer research, non-invasive optical mammography delivers important functional information of the breast tissue, which cannot be accessed by conventional X-ray mammography.

All three physical principles enabled non-invasive imaging in the depth of tissue thereby readying *in vivo* optical imaging for multiple clinical and research roles.

Zusammenfassung

Mediziner und biomedizinische Forscher, die sich mit dem Nachweis und Verlauf von Krankheiten oder der Überwachung einer therapeutischen Intervention beschäftigen, wünschen sich nach Möglichkeit ein wiederholt anwendbares Verfahren, um physiologische und pathologische Prozesse im lebenden Objekt nicht-invasiv, also ohne Schädigung, sichtbar machen zu können. Mit der Verwendung von Licht erfüllen mikroskopische Techniken diesen Wunsch bereits, solange es sich um die Abbildung von µm-dünnen Gewebeschichten handelt. Liegt der für die Untersuchung interessante Bereich in mehr als 1 mm Tiefe, so werden Streuung und Absorption von Licht im Gewebe zu großen Hindernissen.
Meine Forschung hatte zum Ziel, nicht-invasiv Informationen aus mehren Millimetern bis Zentimetern Gewebetiefe zu gewinnen und zu visualisieren, um somit die optische *in vivo* Bildgebung zu verbessern. Im Zuge dieser Arbeit wurden drei physikalische Ansätze untersucht, um dieses Ziel zu erreichen: (i) die Verwendung mehrerer Anregungswellenlängen mit unterschiedlichen Eindringtiefen, (ii) die Nutzung zeitaufgelöster Messsysteme, die es durch die Detektion der Flugzeit der Lichtteilchen im Gewebe erlauben, die Tiefe der Fluoreszenzquelle zu bestimmen, sowie (iii) die optische Tomographie, die durch die Verwendung von mehreren Beleuchtungs- und Detektionswinkeln eine dreidimensionale Bildrekonstruktion ermöglicht.
Mit dem ersten Ansatz verschiedener Anregungswellenlängen (i) wurde ein Surface-Stripping-Algorithmus entwickelt, der die Visualisierung von 4-8 mm tief im Gewebe liegenden, fokalen Fluoreszenzquellen ermöglicht, die der herkömmlichen Fluoreszenz-Reflexions-Bildgebung entgehen würden. Das Verfahren wurde durch Computersimulationen, Phantomexperimente sowie *in vivo* Messungen verifiziert. Dabei gelang es, das Infarktareal im lebenden Kleintier-Schlaganfall-Modell nicht-invasiv, durch die intakte Schädeldecke und Kopfhaut, sichtbar zu machen, obwohl dieses durch das Fluoreszenzsignal der darüber liegenden gut durchbluteten Hirnhaut überdeckt wurde.
Während mit dem ersten Ansatz zwar tiefengewichtete Bilder erzeugt werden können, ist die absolute Quantifizierung der Objekttiefe damit nicht möglich. Erfasst man hingegen die Flugzeit der Fluoreszenz-Photonen im Gewebe mit spezialisierter, schneller Elektronik (ii), so lässt sich daraus die Tiefe des fluoreszierenden Objektes explizit bestimmen. Anhand von Computersimulationen konnte abgeleitet werden, dass sich innerhalb der Abmessungen eines Kleintiers die Tiefe der Fluoreszenzquelle mit einer Genauigkeit von $\pm$ 2 mm bestimmen lässt. Zusätzlich bestätigten Simulationen, dass die Abschätzung der Tiefe auch in Gegenwart von unspezifischer Hintergrundfluoreszenz möglich ist, welche in der *in vivo* Bildgebung meist eine unvermeidliche Störquelle darstellt.
Mit dem dritten Ansatz (iii) kann nicht nur die Tiefe, sondern eine komplette dreidimensionale Darstellung vom Gewebeinneren erreicht werden. Dies wurde in einer klinischen Pilotstudie zur dynamischen, kontrastverstärkten optischen Mammographie bei 22 Patienten durchgeführt. Die rekonstruierten Volumen-Zeitreihen wurden verwendet, um perfusionsbasierte Kenngrößen für den Nachweis und die Charakterisierung von suspekten Raumforderungen in der Brust abzuleiten. Dies gelang mit hoher Sensitivität (85,7%) und Spezifität (87,5%). Hier liefert die nicht-invasive optische Mammographie wichtige funktionelle Informationen über das Brustgewebe, die mit herkömmlicher Röntgenmammographie nicht gewonnen werden können.

Alle drei physikalischen Ansätze erlauben die nicht-invasive Ableitung von Informationen aus der Tiefe des Gewebes. Durch diese Arbeit konnte die optische *in vivo* Bildgebung für mehrere klinische Forschungsbereiche verbessert werden.

Contents

Abstract v
Zusammenfassung vii

1 Introduction **1**
1.1 Motivation and Scientific Background 1
1.2 Outline 5
1.3 Published Work 7

2 Spectral Approach **11**
2.1 Introduction 11
2.1.1 Medical Need: Small Animal Stroke Research 11
2.1.2 Introduction to Fluorescence Imaging 12
2.2 Methods 14
2.2.1 Theory: Non-invasive Surface-Stripping 14
2.2.2 The Surface-Stripping Algorithm 16
2.2.2.1 Region Not Of Interest (RNOI) Equalisation 17
2.2.2.2 Histogram Equalisation/Matching 17
2.2.2.3 Data Acquisition and Preprocessing 22
2.2.3 Phantom Measurements 23
2.2.3.1 Wavelengths Dependence 23
2.2.3.2 Feasibility of the Algorithm 23
2.2.4 Computer Simulations 24
2.2.4.1 General Introduction to Monte Carlo Methods 24
2.2.4.2 Sampling Photon Propagation with MCML 26
2.2.4.3 Simulation of Multispectral Excitation in Fluorescence Reflectance Imaging 29
2.2.5 *In vivo* Application I: Mouse Model of Stroke (Capsule) 30
2.2.6 *In vivo* Application II: Mouse with Stroke 30
2.3 Results 31
2.3.1 RNOI and Histogram Equalisation 31
2.3.2 Results: Wavelength Dependence 33
2.3.3 Simulation Results 35
2.3.4 Results: Phantom Measurements 36
2.3.5 Results *In vivo* I: Mouse Model of Stroke (Capsule) 36
2.3.6 Results *In vivo* II: Mouse with Stroke 40
2.4 Discussion 41

2.4.1 Limitations of the Surface-Stripping Algorithm 42
2.5 Conclusion 43

3 Time-resolved Approach **45**
3.1 Introduction 45
3.1.1 Motivation: Sounding the Depth of Fluorescent Targets 45
3.1.2 Introduction to Time-Resolved Planar (Fluorescence) Imaging . . 46
3.2 Methods 48
3.2.1 The Monte Carlo eXtreme Software for Time-resolved Photon Migration 48
3.2.2 Derivation of the Sensitivity Distribution 52
3.2.3 Simulated Scenarios 54
3.3 Results 56
3.3.1 Simulation Results for Increasingly Realistic Geometries 56
3.3.2 Simulation Results for Heterogeneous Media and Different Levels of Background Fluorescence 59
3.4 Discussion 60
3.4.1 Limitations of the Suggested Depth Ranging Approach 61
3.5 Conclusion 61

4 Tomographic Approach **63**
4.1 Introduction 63
4.1.1 Medical Need: Optical Mammography 63
4.1.2 Introduction to Diffuse Optical Tomography (DOT) 65
4.1.2.1 General Introduction 65
4.1.2.2 Image Reconstruction 67
4.1.2.3 Calculation of Physiological Parameters 73
4.2 Methods 74
4.2.1 Dynamic Contrast-Enhanced Optical Mammography Study . . . 74
4.2.2 Evaluated Dynamic Parameters 77
4.2.3 Reader-Independent Lesion Classification 78
4.2.4 Lesion Localization 80
4.3 Results 80
4.3.1 Mapping Dynamic Features 80
4.3.2 Results: Lesion Localization 83
4.3.3 Results: Reader-Independent Lesion Classification 83
4.4 Discussion 87
4.5 Conclusion 90

5 Conclusions and Outlook **93**

List of Figures **95**

Abbreviations **98**

Bibliography **99**

1 Introduction

1.1 Motivation and Scientific Background

Visualizing physiological and pathological processes inside the living human or animal without doing the subject any harm is most desirable for clinicians and biomedical researchers. It would enable the detection of disease progression and the monitoring of responses to therapeutic intervention over time in a non-invasive[1] manner.

While computed tomography (CT), positron emission tomography (PET) or single-photon emission computed tomography (SPECT) allow for whole-body *in vivo* imaging, they are based on ionizing radiation and therefore can neither be considered non-invasive nor easily applied for repeated measurements over time. Magnetic resonance imaging (MRI) avoids ionizing radiation, but several contra indications as well as considerable costs prohibit the general applicability as a screening modality.

Microscopic techniques, on the other hand, using safe (non-ionizing) light allow high resolution and partly also three-dimensional optical imaging of tissue slices *in vitro* or invasively *in vivo* [Wunder et al., 2005, Patel et al., 2008, Wunder and Klohs, 2008, Castro Lima et al., 2011, Lorbeer et al., 2011, Egawa et al., 2013, Madden et al., 2013, Mahmud et al., 2013, Papayannis et al., 2013, Yang et al., 2013].

When translating these methods to non-invasive measurements in humans or living animals, however, scattering and absorption of visible light in tissue become a major obstacle for optical probing of deeper tissue [Ntziachristos et al., 2003, Jacques and Pogue, 2008, Hillman et al., 2011].

The main intrinsic absorbers of light in the human body are oxygenated (HbO)

[1] Meaning: not penetrating the body, as by incision or ionizing radiation; not invading healthy tissue.

and deoxygenated hemoglobin (HbR), bulk lipids and water [Quaresima et al., 1998, Kukreti et al., 2008]. Near infrared (NIR) light, that is non-ionizing light between the red end of the visible wavelength range and the infrared (between about 650 nm and 900 nm), is an order of magnitude less absorbed by those tissue chromophores than visible light or light at longer wavelengths (see Figure 1.1 B). Different from all other visible colours, red and even more NIR light can propagate up to 10 cm through tissue (Figure 1.1 A) and still be sufficiently detected within this so called diagnostic 'window'. At distances greater than 1 to 2 mm from a source, photons travel randomly through the tissue which can be modelled as particles that behave according to Fick's first law of diffusion [Patterson et al., 1989, Jacques and Pogue, 2008]. The typical mean free path a NIR photon travels in tissue until it is absorbed is approximately 10 cm. The corresponding scattering length, however, is only between 20 to 40 µm [O'Sullivan et al., 2012]. Therefore, even if collimated, coherent laser light enters the tissue, it becomes largely incoherent and nearly isotropic after ∼1 mm of propagation through tissue [Jacques and Pogue, 2008].

As a result, the more tissue layers superpose the relevant region of interest, the more spatial information is lost in non-invasive *in vivo* optical imaging compared to *ex vivo* or in vitro microscopic techniques on thin tissue probes. Figure 1.2 illustrates this issue using the example of a mouse suffering from cerebral ischemia (stroke) in the left hemisphere [Klohs et al., 2008]. At first, the measurement situation in a small animal NIR fluorescence imaging system is sketched. The object (here living animal or extracted brain tissue) is illuminated with NIR light of a steady state excitation source. A high sensitivity camera equipped with appropriate wavelength filters collects the emitted fluorescence light coming from a fluorescent marker that is accumulated at the area of infarction. Subfigure B shows the corresponding *in vivo* fluorescence image of the mouse head while the subfigures in C show the corresponding *ex vivo* NIR fluorescence images of the extracted brain and a brain slice, respectively.

The *ex vivo* images demonstrate that NIR imaging provides a high sensitivity for molecular events that are relatively close to the surface [Ntziachristos et al., 2003, Zavattini et al., 2006, Chaudhari et al., 2009]. However, due to elastic scattering with various cellular components NIR light becomes diffuse within a few

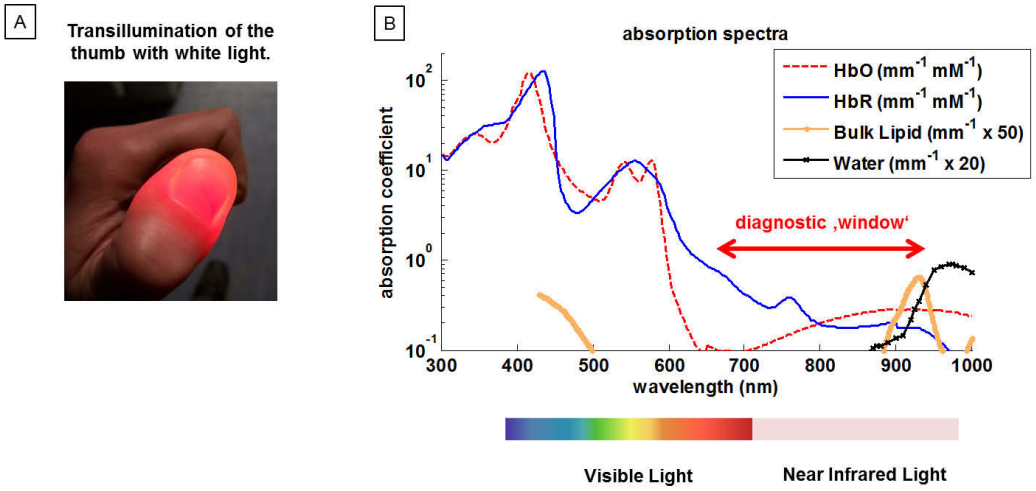

Figure 1.1: *Absorption of light in tissue. A: Transillumination of the thumb with a white flash light. Red light is least absorbed in tissue and can penetrate the thumb after being scattered multiple times. B: Wavelength dependent absorption coefficients of the 4 main absorbers in human tissue. Within the so called diagnostic 'window' near infrared light can penetrate up to 10 cm through tissue while oxygenated hemoglobin (HbO) and deoxygenated hemoglobin (HbR) are the two dominating absorbers. Spectra taken from Ref. [Prahl, 2001]*

.

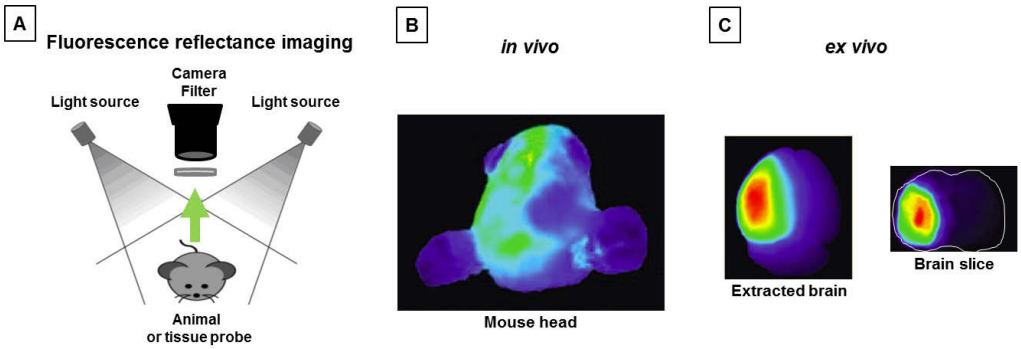

Figure 1.2: *Challenges of in vivo NIR imaging using the example of small animal stroke imaging. A: Basic design of a small animal NIR fluorescence imaging system. In fluorescence reflectance imaging (FRI), the light source for illumination and the detector for collecting the fluorescence light are located on the same side of the object. Appropriate filters are needed to discriminate emission light (fluorescence) from excitation light. Schematic adapted with permission from Ref. [Stemmer et al., 2012]. B: In vivo fluorescence image of a living mouse suffering from cerebral ischemia in the left hemisphere. C: Corresponding ex vivo NIR fluorescence image of the extracted brain and a corresponding brain slice using a fluorescent monoclonal antibody, labeled with the near-infrared fluorescence dye Cy5.5 (Cy5.5-CD40MAb). Adapted with permission from Ref. [Klohs et al., 2008]*

.

millimetres of propagation through tissue [Ntziachristos, 2006, Jacques and Pogue, 2008]. This results in a loss of imaging resolution. Comparing the subfigures 1.2B and C illustrates how imaging through the intact scalp and skull no longer allows exact localization of the ischemic region and how blurring dominates the images with increasing tissue depth.

Both scattering and absorption in overlying tissues non-linearly decreases the number of photons reaching the detector with increasing distance between body surface and the (fluorescent) object of interest. Moreover, the measured spatial photon distribution on the surface of an object could be the same whether it originates from a focal absorbing or fluorescing source in a deep layer or a broader source of equal concentration in a superficial layer [Ntziachristos et al., 2003].

This poor depth resolution is often considered a fundamental drawback of *in vivo* optical imaging and has limited its success when the region of interest is more than 1 mm in depth and moreover covered by bone, blood capillaries or skin.

1.2 Outline

New approaches are required and have been developed herein to non-invasively recover information from the depth of tissue in *in vivo* imaging where numerous tissue layers can impose the relevant region of interest. In the following chapters, I will describe three physical methods that I have investigated to recover information *in vivo* from deeper tissue layers.

Light has different penetration depths depending on the wavelength chosen. Therefore, multiple excitation wavelengths can help to distinguish different depths. A less penetrating wavelength mainly excites superficial fluorescence sources, whereas deeper penetrating light also excites regions of interest in deeper tissue layers. I developed a novel surface-stripping algorithm that enhances image contrast and detectability of fluorochromes located several mm deep inside the living animal [Piper et al., 2010]. In Chapter 2 computer simulations as well as phantom and *in vivo* measurements to this effect will be presented which give evidence that it can be used to reduce overlaying superficial sources of *no* interest as is the case in *in vivo* small animal stroke imaging.

Time-resolved systems, which are measuring time of flight distributions of the excitation and/ or fluorescence photons travelling through tissue, principally con-

tain enough information for a depth-resolved determination of absorption changes at a single wavelength [Steinbrink et al., 2001, Liebert et al., 2006, Jelzow et al., 2012]. In homogeneous infinite media with a focal fluorescent inclusion the mean time of flight of the emitted fluorescence photons is directly proportional to the inclusion's depth [Hall et al., 2004]. I performed Monte Carlo simulations investigating the validity of this proportionality for potential *in vivo* imaging on realistic, inhomogeneous small animal geometries, which are described in Chapter 3. From these I have derived a calibration-approach which is promising to sense the depth of an object with planar time-domain imaging, even in the presence of strong non-specific background fluorescence [Piper et al., 2014b].

Most favourable are three-dimensional imaging techniques that allow for a tomographic image reconstruction. This can be achieved by using multiple source and detector combinations to reconstruct 3D volumes of optical properties. When using safe (non-ionizing) light, image reconstruction is unequally more elaborate because simple back-projection algorithms as used for X-ray CT cannot be applied due to the high scattering of light in tissue. In Chapter 4 tomographic diffuse optical imaging and image reconstruction are introduced using the example of optical mammography. In this emerging field of preclinical research, recent developments in technology have shifted from static to dynamic imaging contrast [Schmitz et al., 2005, Schneider et al., 2011, Schreiter et al., 2013]. Such non-invasive optical imaging applications are expected to deliver important additional functional information of breast tissue properties which cannot be accessed by conventional X-ray mammography or magnetic resonance imaging. In cooperation with the Institute of Radiology, Charité University Medicine Berlin, a prospective patient study was conducted to evaluate fast 3D near-infrared breast imaging using extrinsic dynamic contrast for the detection and characterization of breast occupying lesions [Schneider et al., 2011]. Within this clinical pilot study in 22 patients, volume time series after bolus injection of the blood pool contrast agent ICG were reconstructed. Using these, I developed a computer-aided diagnosis algorithm to *automatically* distinguish between malignant and benign breast tissue without subjective evaluation by a trained reader. The results presented here show that early perfusion analysis of ICG-enhanced fast 3D optical mammography can help to non-invasively detect malignant breast lesions in the depth

of tissue.

1.3 Published Work

Journal Articles

(1) Piper SK, Bahmani P, Klohs J, Bourayou R, Brunecker P, Muller J, Harhausen D, Lindauer U, Dirnagl U, Steinbrink J, Wunder A (2010) *Non-invasive surface-stripping for epifluorescence small animal imaging.* Biomedical optics express 1:97-105.

(2) Schneider P, Piper SK, Schmitz CH, Schreiter NF, Volkwein N, Ludemann L, Malzahn U, Poellinger A (2011) *Fast 3D Near-infrared breast imaging using indocyanine green for detection and characterization of breast lesions.* Rofo 183:956-963

(3) Schreiter NF, Volkwein N, Schneider P, Maurer MH, Piper SK, Schmitz C, Poellinger A (2013) *Optical imaging of breast cancer using hemodynamic changes induced by valsalva maneuver.* RoFo : Fortschritte auf dem Gebiete der Rontgenstrahlen und der Nuklearmedizin 185:358-366.

(4) Piper SK, Krueger A, Koch SP, Mehnert J, Habermehl C, Steinbrink J, Obrig H, Schmitz CH (2014) *A wearable multi-channel fNIRS system for brain imaging in freely moving subjects.* NeuroImage 85:64-71.

(5) Piper SK, Habermehl C, Schmitz CH, Kuebler WM, Obrig H, Steinbrink J, Mehnert J (2013) *Towards Whole-Body Fluorescence Imaging in Humans.* PLoS ONE 8(12): e83749. doi:10.1371/journal.pone.0083749

a) Submitted: Piper SK, Gosmann J, Mehnert J, Betz T, Steinbrink J (2014) *Towards determining the depth of fluorescent targets by time-domain reflectance imaging.* Phys. Med. Biol.

Conference Abstracts

(1) S.K. Piper, T. Nierhaus, S. Holtze, T. Krause, O. Berthold, B. Taskin,J. Steinbrink, and A. Villringer, *Brain responses to subliminal somatosensory stimulation in the EEG,* HBM - Human Brain Mapping (San Francisco, CA USA, June 18-23, 2009). *Trainee Abstract Award Winner*

(2) S.K. Piper, J. Klohs, P.Brunecker, J. Steinbrink, A. Wunder, *Efficient reduction of superficial background signals in non-invasive near-infrared fluorescence (NIRF) imaging of brain pathologies in small animals,* Molekulare Bildgebung 2010 (Chiemsee, Germany, Nov 4-6, 2010).

(3) C. H. Schmitz, S.K. Piper, P. Schneider, N. Volkwein, N. Schreiter, and A. Poellinger, *Diffuse Optical Imaging of ICG Dynamics in the Diseased Breast with High Temporal Resolution,* in Biomedical Optics and 3-D Imaging, OSA Technical Digest (CD) (Optical Society of America, paper BTuD101 (Miami, FL USA, April 11-14 2010).

(4) S.K. Piper, P. Schneider, N. Volkwein, N. Schreiter, A. Poellinger, and C. H. Schmitz, *Fast 3D Optical Mammography using ICG Dynamics for Reader Independent Lesion Differentiation,* Presentation BW4A.1 at Biomedical Optics and Digital Holography and Three-Dimensional Imaging (Miami, FL USA, April 29 - May 2, 2012).

(5) J. Mehnert, S. K. Piper, C. Habermehl, C. H. Schmitz, H. Obrig, and J. Steinbrink, *Whole Body Fluorescence Imaging in Humans,* paper BW4A.6 at Biomedical Optics and Digital Holography and Three-Dimensional Imaging (Miami, FL USA, April 29 - May 2, 2012).

(6) A. Krüger, S. P. Koch, J. Mehnert, C. Habermehl, S.K. Piper, J. Steinbrink, H. Obrig, and C. H. Schmitz, *Imaging of Motor Activity in Freely Moving Subjects Using a Wearable NIRS Imaging System,* paper BM4A.3 at Biomedical Optics and Digital Holography and Three-Dimensional Imaging (Miami, FL USA, April 29 - May 2, 2012).

(7) S.K. Piper, A. Krüger, S.P. Koch, J. Mehnert, C. Habermehl, J. Steinbrink, H. Obrig, and C.H. Schmitz, *A Wearable Multi-channel NIRS Imaging System for Brain Imaging in Freely Moving Subjects,* Poster 7 at Functional Near Infrared Spectroscopy (London, UK, October 26 - 28, 2012).

(8) S.K. Piper, J. Mehnert, C. Habermehl, C.H. Schmitz, W. Kuebler, H. Obrig, J. Steinbrink, *Whole body fluorescence imaging in humans*, SPIE Photonics West 2013, BioS Conference [8578-65] (San Francisco, CA USA, Feb. 2-7, 2013)

(9) S.K. Piper, S. Fazli, P. Schneider, N. Volkwein, N. Schreiter, A. Poellinger, and C.H. Schmitz, *Reader-Independent Classification of Malignant and Benign Breast Lesions Based on Delayed ICG Washout Kinetics,* Presentation ETu1C.5 at the European Conferences on Biomedical Optics (Munich, Germany, May 12-16, 2013).

(10) C.H. Schmitz, S.K. Piper, P. Schneider, N. Volkwein, N. Schreiter, and A. Poellinger, *Comparison of Extrinsic and Intrinsic Dynamic Contrasts in Fast 3D Optical Mammography,* Presentation ETu1C.4 at the European Conferences on Biomedical Optics (Munich, Germany, May 12-16, 2013).

(11) S.K. Piper, A. Krueger, S.P. Koch, J. Mehnert, C. Habermehl, J. Steinbrink, H. Obrig, C.H. Schmitz, *Ein tragbares Multi-Kanal NIRS-System: Validierungsstudie beim Fahrradfahren am Spreeufer,* invited talk at the 22nd German EEG/EP Mapping Meeting. (Schloss Rauischholzhausen, Germany, Oct 11-13, 2013)

(12) Piper SK, Elliott JT, Lawrence KSt, Poellinger A, Schmitz CH (2014) *Kinetic DOT Reconstruction of Contrast-Enhanced Optical Mammography Data for Reader-Independent Lesion Detection.* Presentation BW4B.8 at Biomedical Optics (Miami, FL USA, April 26 - 30, 2014)

Oral Presentations

(1) "Efficient reduction of superficial background signals in non-invasive near-infrared fluorescence (NIRF) imaging of brain pathologies in small animals," Molekulare Bildgebung 2010, Nov.4-6 2010, Chiemsee, Germany

(2) "Fast 3D Optical Mammography using ICG Dynamics for Reader Independent Lesion Differentiation," Presentation BW4A.1 at Biomedical Optics and Digital Holography and Three-Dimensional Imaging (Miami, FL USA, April 29 - May 2, 2012)

(3) "Whole body fluorescence imaging in humans", SPIE Photonics West 2013, BioS Conference [8578-65] (San Francisco, CA USA, Feb. 2-7, 2013)

(4) "Reader-Independent Classification of Malignant and Benign Breast Lesions Based on Delayed ICG Washout Kinetics," Presentation ETu1C.5 at the European Conferences on Biomedical Optics (Munich, Germany, May 12-16, 2013).

(5) "Ein tragbares Multi-Kanal NIRS-System: Validierungsstudie beim Fahrradfahren am Spreeufer," invited talk at the 22nd German EEG/EP Mapping Meeting. (Schloss Rauischholzhausen, Germany, Oct 11-13, 2013)

(6) "Kinetic DOT Reconstruction of Contrast-Enhanced Optical Mammography Data for Reader-Independent Lesion Detection," Presentation BW4B.8 at Biomedical Optics (Miami, FL USA, April 26 - 30, 2014)

2 Spectral Approach Resolving Depth for Planar Imaging with Spectral Excitation

2.1 Introduction

In this chapter a new approach will be developed to increase the depth sensitivity for non-invasive fluorescence imaging by making use of multi-spectral continuous-wave NIR light. The method will be tested for a planar small animal imaging system. Challenges of *in vivo* imaging of brain pathology will be presented and addressed by the new approach. Parts of this chapter were published in Biomedical Optics Express [Piper et al., 2010].

2.1.1 Medical Need: Small Animal Stroke Research

Non-invasive near-infrared fluorescence (NIRF) imaging is a powerful tool to study pathophysiology in a wide variety of animal models of disease [Wunder et al., 2005, Pierce et al., 2008,Wunder and Klohs, 2008] including brain diseases [Ntziachristos et al., 2002,Hintersteiner et al., 2005,Hsu et al., 2006,Klohs et al., 2008,Hyde et al., 2009, Klohs et al., 2009b, Klohs et al., 2009a, McCann et al., 2009] and it benefits from the development of numerous highly specific reporter agents [Ntziachristos, 2006]. However, various methodological challenges have to be considered when applying non-invasive NIRF imaging to animal models of brain disease [Hillman, 2007].

Particularly in brain imaging, the non-invasive visualization of compound binding or uptake within diseased brain tissue is confounded by strong superficial signals [Klohs et al., 2008, Klohs et al., 2009b, Klohs et al., 2009a]. These signals originate from large vessels on the dorsal surface of the brain [Laufer et al., 2009] (compare Figure 2.2) and the highly vascularized scalp, skull bone, and dura mater, and are regarded as "background" signal in brain imaging. They have to be considered, especially because most compounds used for NIRF imaging have a long blood half-life and/or a high rate of extravasation [Wunder et al., 2005,Pierce et al., 2008, Wunder and Klohs, 2008]. Therefore, the superficial background signals can impede the detection of fluorescence in deeper tissue layers [Graves et al.,

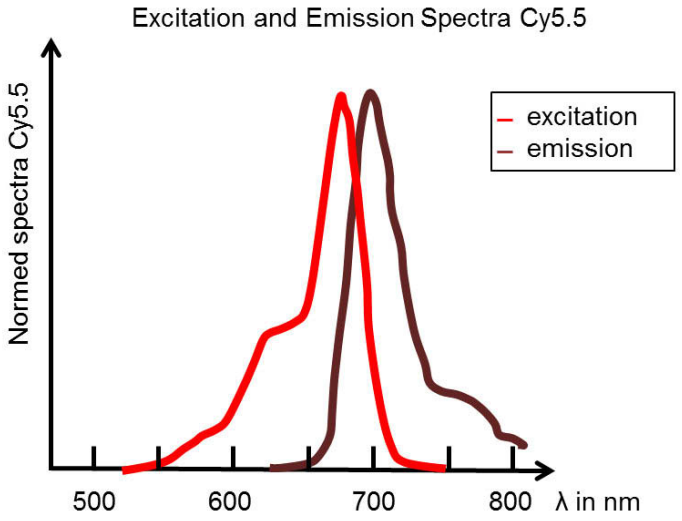

Figure 2.1: *Excitation and shifted emission spectra of the NIR fluorophore Cy5.5. Spectra taken from [Arizona, 2014].*

2005, Gao et al., 2005] (see for example Figure 2.3D or Figure 2.12). In the following sections of Chapter 2, a new method to improve the contrast of non-invasive fluorescence images of the murine brain will be described and validated reducing the contribution of unspecific fluorescence coming from superficial structures.

2.1.2 Introduction to Fluorescence Imaging

For fluorescence imaging the object is illuminated with excitation light, which will excite subsurface and superficial fluorophores. The immediate emission of light of an in most cases shifted wavelength is called fluorescence [Andersson-Engels et al., 1997, Ntziachristos et al., 2003, Lakowicz, 2009]. A high-sensitivity camera, equipped with appropriate wavelength filters, can then collect the emission light, which is proportional in strength to the excitation light. The proportionality factor is given by the wavelength dependent quantum yield or emission efficiency $\Phi_F(\lambda)$ of a given fluorophore defined as the quotient of emitted to absorbed photons.

$$\Phi_F(\lambda) = \frac{\#\text{ photons emitted}}{\#\text{ photons absorbed}}$$

Figure 2.1 shows the excitation and shifted emission spectra of the fluorophore Cy5.5, a blue-green chromophore that absorbs and emits in the near-infrared wavelength range [Arizona, 2014]. Cy5.5 is excitable between about 580 nm and 700

nm with an excitation maximum around 670 nm. Its maximum emission is around 710 nm [Ballou et al., 2005]. Depending on the number of fluorophores conjugated to a macromolecule and furthermore the macromolecule itself as well as the solvent, the absolute values of absorption and emission can vary due to quenching (re-absorption of fluorescence photons) and other photo-chemical reactions [Berlier et al., 2003, Koyama et al., 2007, Ogawa et al., 2009]. Narrow optical bandpass filters are required to adequately separate excitation and emission light.

Depending on the excitation source applied, NIR imaging in general and fluorescence imaging in particular can be broadly categorized in continuous-wave (cw) systems utilizing steady state excitation sources, frequency-domain (FD) systems using frequency modulated (MHz) sources, and time-domain (TD) systems using laser pulses of several femto to pico seconds width together with a time-gated detection [Hebden et al., 1997, Ntziachristos et al., 2003, Wolf et al., 2007, Leblond et al., 2010](see also Chapter 3). In reflectance imaging, the object is illuminated from the same side from which the detector system measures the emitted fluorescence light, as is shown in Figure 1.2A. This method is termed fluorescence-reflectance imaging (FRI) or more general epi-illumination imaging [Ntziachristos, 2006]. Usually, all components are incorporated in a light-tight housing.

Advantages and Limitations of cw Fluorescence Reflectance Imaging

The most important advantage of near-infrared fluorescence (NIRF) over (intrinsic) absorption contrast in optical imaging is that the red-shifted fluorescence emission arising from fluorophores inside the tissue is clearly distinguishable from low tissue background and the incident excitation light. Although the trend goes to whole-body tomographic imaging systems that allow 3D image reconstruction and moreover quantification of fluorescence particles, the vast majority of applications of *in vivo* small animal imaging are based on cw epi-illumination imaging [Leblond et al., 2010]. Advantages are its simplicity of operation, a relatively inexpensive hardware, a high throughput capability as well as a high sensitivity for molecular events that are relatively close to the surface [Ntziachristos et al., 2003]. Fluorescence imaging on a macroscopic scale largely depends on spatially resolving bulk signals from specific fluorescent entities reporting on cellular and molecular activity [Ntziachristos, 2006].

Applying non-invasive NIRF imaging to animal models of brain disease or other deeper laying targets in general is challenging as FRI is inherently highly sensitive to fluorescent sources in superficial layers [Piper et al., 2010]. Therefore, the desired visualization of compound binding or uptake within deeper tissue can mingle with superficial unspecific fluorescence from the unbound fluorophore circulating in the vasculature [Klohs et al., 2006, Klohs et al., 2009b, Piper et al., 2010].

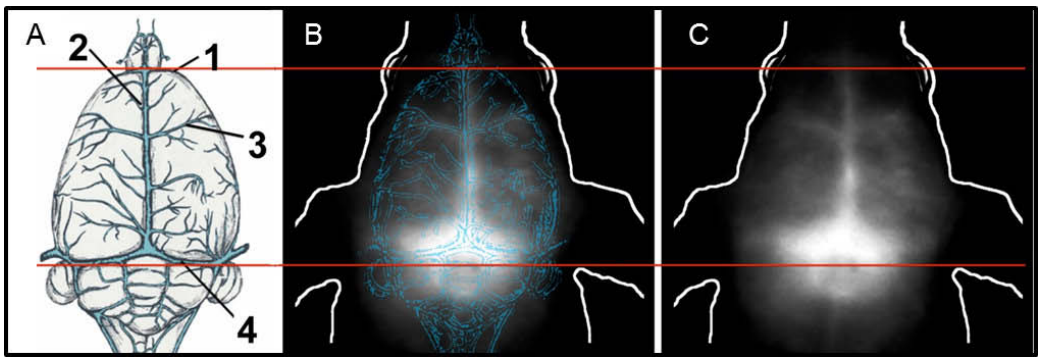

Figure 2.2: *Vascular anatomy of the murine brain. A: Schema of superficial cerebral vascular anatomy of the murine brain. 1: inferior cerebral vein, 2: superior sagittal sinus, 3: superior cerebral vein; 4: transverse sinus (taken with permission from [Laufer et al., 2009]. C: non-invasive NIRF image of a healthy mouse injected with NIR fluorescent albumin. B: overlay of A and C.*

2.2 Methods

2.2.1 Theory: Non-invasive Surface-Stripping

When measuring in reflectance geometry, the penetration depth of light into tissue is a function of scattering and absorption. In the NIR wavelength range discussed here, hemoglobin is the most relevant absorber. The absorption coefficients of its two states, oxygenated and deoxygenated hemoglobin, are highly wavelength dependent while scattering can be considered as constant (see Figure 1.1). Below about 700 nm the absorption coefficient µa increases rapidly with decreasing wavelength [Prahl, 2001, Hillman, 2007]. Therefore, light at a shorter wavelength has a lower penetration depth in tissue. When tissue is consecutively excited at two different wavelengths (within the excitation range of the fluorophore), two fluorescence images can be obtained at the fluorescence wavelength (710 nm for the fluorophore Cy5.5). Both images have a contribution from superficial fluorescent sources and from deep tissue sources. However, the contribution of these two compartments differs depending on the penetration depth of the excitation light. The associated fluorescence image of the less penetrating excitation wavelength yields a stronger relative weight for the fluorescence from superficial layers.

In a simplistic model, we can describe a deep laying fluorescing inclusion with a concentration c^{deep}, while fluorescent sources from superficial layers shall be represented by c^{surf} (see Figure 2.3D). At two different wavelengths the fluorescence detected in an FRI system is given by

$$I_{\lambda_1}^{fluo} = \alpha_1 \Phi_F(\lambda_1) \left(S_{\lambda_1}^{surf} c^{surf} + S_{\lambda_1}^{deep} c^{deep} \right)$$

$$I_{\lambda_2}^{fluo} = \alpha_2 \Phi_F(\lambda_2) \left(S_{\lambda_2}^{surf} c^{surf} + S_{\lambda_2}^{deep} c^{deep} \right) \tag{2.1}$$

Here I_{λ}^{fluo} is the measured fluorescence intensity per image voxel in J/cm^{2}s, $\Phi_F(\lambda_i)$ is the quantum efficiency, S_{λ}^{surf} and S_{λ}^{deep} are the sensitivities for wavelength λ_i in J·l/(cm^{2}s mol) and c^{surf}, c^{deep} are the mean fluorophore concentrations in µmol/l for the superficial layer and the inclusion depth, respectively. The different coupling coefficients α_1 and α_2 can possibly be determined using a calibration phantom with a known fluorophore concentration.
With $\lambda_1 < \lambda_2$, a difference image $\Delta\tilde{I}$ of both fluorescence images (2.1) can be defined, potentially reducing the influence superficial layers.

$$\Delta\tilde{I} = I_{\lambda_2}^{fluo} - \beta \cdot I_{\lambda_1}^{fluo} \tag{2.2}$$

When beta is chosen

$$\beta = \left(\frac{\alpha_2 \cdot \Phi_F(\lambda_2) \cdot S_{\lambda_2}^{surf}}{\alpha_1 \cdot \Phi_F(\lambda_1) \cdot S_{\lambda_1}^{surf}} \right), \tag{2.3}$$

such that the contributions from superficial sources in both images are of equal strength, the difference image (2.2) can be written as

$$\Delta\tilde{I} = c^{deep} \alpha_2 \Phi_F(\lambda_2) \left(S_{\lambda_2}^{deep} - \frac{S_{\lambda_2}^{surf}}{S_{\lambda_1}^{surf}} \cdot S_{\lambda_1}^{deep} \right). \tag{2.4}$$

In Eq. (2.4) the difference image $\Delta\tilde{I}$ is no longer a function of c^{surf} but is now dependent only on the concentration of the inclusion c^{deep} and a proportionality constant $\alpha_2\Phi(\lambda_2)$.

In practice, however, neither the sensitivities S_λ nor the coupling coefficients α_i are known. Therefore, a different way is needed to determine β. Moreover, due to differences in illumination intensity and emission efficiency Φ_F of the fluorophore between different excitation wavelengths, the measured fluorescence signal can largely vary in strength. As a consequence, simple image subtraction ($\beta = 1$) does not usually lead to sufficient reduction of superficial background signals.

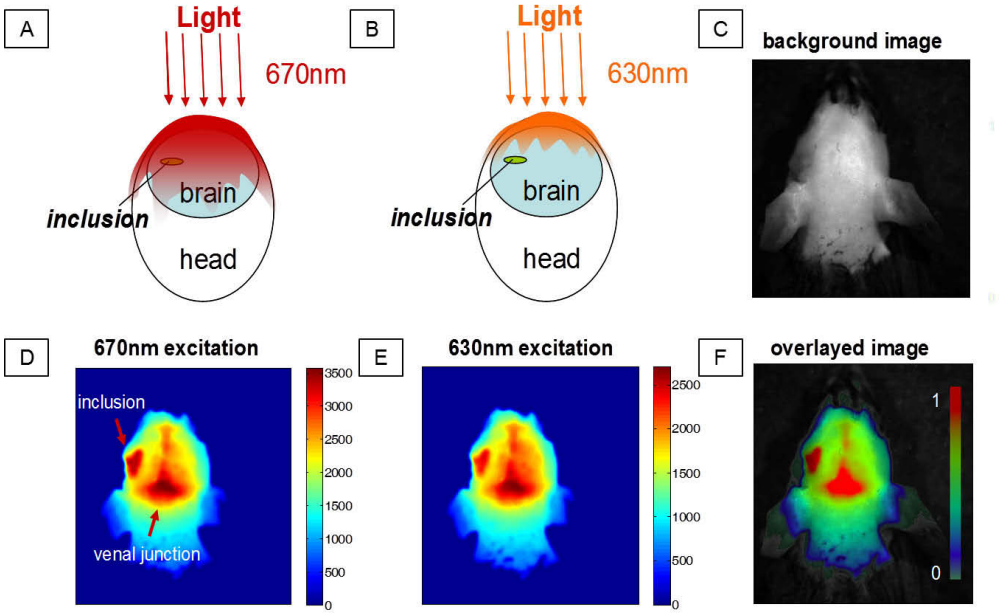

Figure 2.3: *Schematic representation of the surface-stripping idea. A: Light at 670 nm has a higher penetration depth than at 630 nm (B). D,E: Color-coded in vivo fluorescence imaging data of a mouse head with a 2 mm fluorophore capsule containing 10^{-12} mol Cy5.5 implanted into the left hemisphere and with an additional intravenous injection of 0.2 nmol Cy5.5-dextran consecutively excited with 670 nm (D) and 630 nm (E). C:Grey-scaled background (reflectance) image of the mouse head excited with 670 nm and acquired without the fluorescence filter. F: Overlay of the normalized fluorescence image shown in D projected onto the reflectance image of the mouse shown in C. FOV: 5 × 5 cm^2.*

In the following subsections, two approaches will be introduced to determine β experimentally such that $\Delta\tilde{I}$ is a *depth-weighted* fluorescence image, where signal intensities coming from superficial layers largely cancel out as they contribute to both fluorescence images excited at λ_1 and λ_2, respectively.

2.2.2 The Surface-Stripping Algorithm

Figure 2.3 gives an example of fluorescence images acquired with different excitation wavelengths. First, an exaggerated schematic representation of different penetration depths is given in subplot A and B. Furthermore, fluorescence images of a mouse with a fluorescent capsule implanted into the left hemisphere excited with 670 nm (D) and 630 nm (E), respectively, are shown. Light at 630 nm has a lower penetration depth than 670 nm. Therefore, the resulting fluorescence image

of the first is stronger influenced by the scalp than the fluorescence image excited at 670 nm. Over the left hemisphere, fluorescence from the inclusion is clearly visible for both excitation wavelengths. However, signal intensities of the capsule are higher in the 670 nm image. Both fluorescence images additionally show a large fluorescence signal coming from the venous junction of the superior sagittal sinus and the transverse sinus, which in this case, is a disturbing fluorescence signal from the scalp.

2.2.2.1 Region Not Of Interest (RNOI) Equalisation

One approach to define the scaling factor β experimentally is to equalise the mean image intensities of both fluorescence images taken over a 'region not of interest' (RNOI).

$$\frac{1}{N}\sum_{i\,\in\,\mathrm{RNOI}}^{N} I_{\lambda_2}^{fluo}(i) = \beta_{\mathrm{RNOI}} \cdot \frac{1}{N}\sum_{i\,\in\,\mathrm{RNOI}}^{N} I_{\lambda_1}^{fluo}(i), \tag{2.5}$$

Here, a region in the image is defined where fluorescence in deeper tissue is assumed to be low and only superficial sources are expected/present. For brain imaging this approach is helpful when the diseased hemisphere is known. In the manually chosen RNOI c^{deep} is approximated as zero and, consequently, $\Delta\tilde{I}$(RNOI) also equals zero.

$$\frac{1}{N}\sum_{i\,\in\,\mathrm{RNOI}}^{N} \Delta\tilde{I}(i) \approx 0 \tag{2.6}$$

In this case equation (2.2) can be inverted to determine β :

$$\beta_{\mathrm{RNOI}} = \frac{\frac{1}{N}\sum_{i\,\in\,\mathrm{RNOI}}^{N} I_{\lambda_2}^{fluo}(i)}{\frac{1}{N}\sum_{i\,\in\,\mathrm{RNOI}}^{N} I_{\lambda_1}^{fluo}(i)}, \tag{2.7}$$

which is then given by the mean signal intensity over all N image pixel i that are element of the RNOI of the fluorescent image excited with λ_2 divided by the respective mean in the fluorescent image excited with λ_1 (see Figure 2.6A,B). This approach is defined in analogy to a constant offset subtraction calculated by the counts over a region *distant* from the fluorescent target for single wavelength tomography [Graves et al., 2005].

2.2.2.2 Histogram Equalisation/Matching

If prior knowledge of the fluorophore distribution is not available, β can be calculated using a histogram equalisation (HE) in the sense of *matching* the histograms of both fluorescence images taken.

A histogram h provides the frequency n_i of the signal intensity value s_i in an image, independently of its spatial distribution. For $0 \leq s_i \leq s_{max}$ we can write:

$$h(s_i) = n_i \quad i = 1, ..., N \tag{2.8}$$

$$\sum_{i=1}^{S} n_i = N,$$

with N being the number of image pixel and S the total number of signal intensities. Figure 2.6 D shows the intensity histograms of the images in Figure 2.3 D and E.

When matching the histograms h_{λ_i} of both fluorescence images taken, we make the assumption that the underlying intensity distributions p_{λ_i} are similar but may have a scaling-offset due to differences in laser intensity and quantum efficiency of the fluorophore. Moreover, we assume that a focal, deep laying inclusion adds only to a small range of pixel intensities in the image acquired with the deeper penetrating wavelength. HE transforms the signal intensity distribution h_{λ_1} of the image acquired at excitation wavelength λ_1 to the distribution of signal levels h_{λ_2} acquired at λ_2. As a result, the difference between the two *matched* images after HE is mainly due to the focal inclusion of an unknown position in the brain.

Mathematical Background to Histogram Equalisation

The intensity values s_i of an image can be considered as random variables [Jähne, 2005]. This means that the measured intensity in an image pixel i is actually not characterized by a single value s_i but through a probability density function $p_s(s)$. The total probability of measuring any intensity value is 1. Therefore, the probability density function has the following characteristics:

$$\int_{-\infty}^{\infty} p_s(s)ds = 1, \tag{2.9}$$

$$p_s(s) = \frac{n}{\int_{-\infty}^{\infty} n \; dn} \quad 0 \leq s \leq 1$$

with n being the absolute frequency of the signal intensity value s.

In the continuous case, a certain intensity value $s + ds$ is measured with the probability $p_s(s)ds$. In the discrete case, only a finite number S of intensity values s_i with $i = 1, 2, 3, .., S$ can be measured with the probability $p_s(s_i)$.

The distribution of s can be transformed with any transfer function $r = T(s)$ that has the following characteristics:

(i) T is monotonically increasing in the interval $(0, 1)$

(ii) $0 \leq T(s) \leq 1$ for $0 \leq s \leq 1$

and the corresponding inverse function $s = T^{-1}(r)$ for $0 \leq r \leq 1$ with the analogue conditions (i) and (ii). The probability density distribution $p_r(r)$ of the transformed values r is then given by:

$$p_r(r) = \left[p_s(s) \frac{ds}{dr} \right]_{s=T^{-1}(r)} \tag{2.10}$$

If the transfer function is chosen as the cumulative distribution function of p_s:

$$r = T(s) = \int_0^s p_s(w)dw \quad 0 \leq s \leq 1. \tag{2.11}$$

then the differentiation with respect to s yields [Heuser, 1990]:

$$\frac{dr}{ds} = p_s(s) \tag{2.12}$$

Applying equation (2.12) to (2.10) gives a uniform density distribution, constant to 1:

$$p_r(r) = \left[p_s(s) \frac{1}{p_s(s)} \right]_{s=T^{-1}(r)} = 1 \quad 0 \leq r \leq 1 \tag{2.13}$$

In the case of continuous data, the application of the cumulative distribution function as transfer function yields a uniformly distributed (also termed *equalised*) histogram with all probabilities equal to 1.

To match the distribution $p_s(s)$ to a desired distribution $p_z(z)$ the following steps are taken:

(1) The original distribution is equalised to a uniform distribution.

$$r = T(s) = \int_0^s p_s(w)dw$$

(2) The cumulative distribution function of the desired distribution is calculated.

$$v = G(z) = \int_0^z p_z(w)dw$$

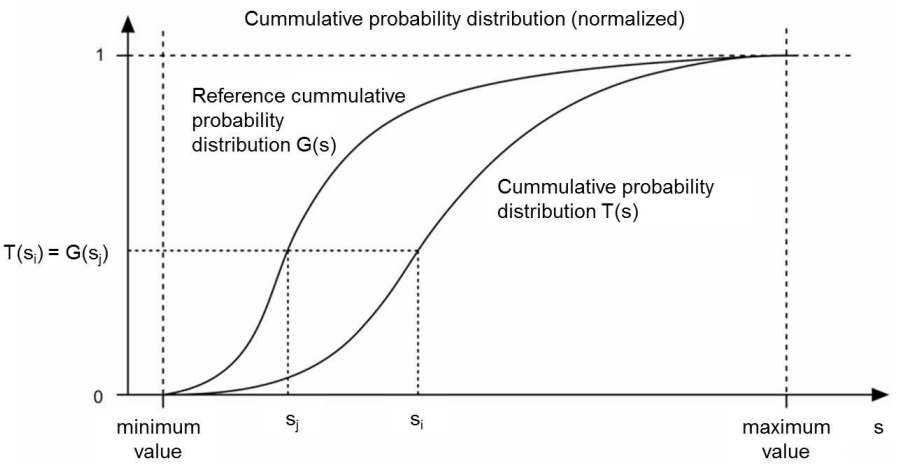

Figure 2.4: *Mathematical background to histogram equalisation and matching. To match a given probability density function $p_s(s)$ to $p_{s'}(s')$, calculate the respective cumulative probability density functions $T(s)$ and $G(s')$ according to equation* (2.11)*. Any particular value s_i in the data to be adjusted is then replaced by s_j whose cumulative histogram value $G(s_j)$ matches $T(s_i)$.*

(3) Both distributions $p_r(r)$ and $p_v(v)$ now have identical uniform density. Therefore, they can be exchanged. In the inversion process $z = G^{-1}(v)$, v is replaced by the values of r (the equalised original). As a result,

$$z = G^{-1}(r) = G^{-1}(T(s))$$

has the desired density distribution. Figure 2.4 illustrates the above described process of matching two probability density functions.

For an image, however, the distribution of intensity values is discrete and a continuous function $p_s(s)$ does not exist. Therefore, the equalisation results for a histogram (Equation (2.8)) with the corresponding cumulative distribution function is only an approximation to the ideal (continuous) case.

$$r_k = T(s_k) = \sum_{j=1}^{k} \frac{n_j}{N} = \sum_{j=1}^{k} p_s(s_j) \quad k = 1, ..., S \quad s_k = T^{-1}(r_k) \tag{2.14}$$

Computational Implementation

The process of equalising (matching) two discrete histograms takes the input image I_{λ_1} and produces an output image $\beta_{\text{HIS}} \cdot I_{\lambda_1}$ whose histogram matches the histogram specified by image I_{λ_2}. The objective is to find a β_{HIS} such that the sum of absolute errors between the intensity level histogram of the transformed picture and that of a reference picture is minimized [Gonzalez and Woods, 2002, Gonzalez et al., 2004].

In detail, β_{HIS} is calculated as the factor that best minimizes the bounded area between the parametric representation of the intensity histograms of I_{λ_2} and $\beta_{\text{HIS}} \cdot I_{\lambda_1}$ (see Figure 2.6D). Let L be the number of histogram bins, then the bounded area A between two histograms h_1 and h_2 was calculated as:

$$A = \frac{1}{2}|h_1(L) \cdot h_2(1) - h_1(1) \cdot h_2(L) + \sum_{i=1}^{L-1} h_1(i) \cdot h_2(i+1) - h_1(i+1) \cdot h_2(i)| \quad (2.15)$$

The HE algorithm is implemented as follows:

- Approximate β_{HIS} in a first step by calculating the coefficient α_1 of a first order polynomal fit P that best fits the data I_{λ_1} to I_{λ_2} in a least-squares sense (MATLAB function `polyfit`):

$$P(I_{\lambda_1}) = \alpha_1 \cdot I_{\lambda_1} = I_{\lambda_2}.$$

- Calculate a range of 100 different values of β_i with

$$0.5\alpha_1 \leq \beta_{\text{HIS}} \leq 2\alpha_1.$$

- For every β_i,
  - generate the histogram for the input image h_{λ_2} and the specified image $h_{\beta_i \dot{\lambda}_1}$ at the same resolution of $L = 30$ bins,
  - calculate the respective bounded area A according to Equation (2.15).
- Find the global minimum of $A(\beta_i)$. Take β_i of the minimum bounded area $min(A)$ as β_{HIS}.

Sometimes, the initial approximation α_1 is adverse, such that the range of β-values does not properly cover the global minimum. In this case, the range needs to be individually adjusted.

2.2.2.3 Data Acquisition and Preprocessing

The Applied Small Animal FRI System

The FRI system that was used was developed at the Department of Experimental Neurology of the Charité University Medicine Berlin. Epi-illumination fluorescence reflectance images can be taken at different excitation wavelengths without moving the object [Klohs et al., 2006, Piper et al., 2010]. Light from two TE-cooled laser diodes emitting 670 nm and 633 nm (Roithner Lasertechnik, Vienna, Austria) is coupled to an optical switch (LightTech Fiberoptics Inc, San Leandro, CA) and directed into a dark chamber, where it illuminates the object from above. A back-illuminated nitrogen-cooled CCD camera (Vers Array 512, 512 x 512 pixel, Roper Scientific Inc., Duluth, GA) with a focusing lens system (Nikkor macro lens, f = 50 mm, f/1.2, Nikon, Duesseldorf, Germany) and two 710 nm interference filters (FWHM 20 nm, Andover Corp., Salem, NH) detects the emitted fluorescence light. The acquired fluorescence intensity images are stored as *.SPE files wich were then further processed in MATLAB

Data Preprocessing

Data processing and analysis were performed using MATLAB 6.5 software (The Mathworks, Inc., Natick, MA). An automatic baseline correction prior to analysis removed the read-out noise offset. All images were normalized to acquisition time and a top hat image (MATLAB function `imtophat`, structuring element circle with a diameter of 4 pixels) was subtracted from each image to correct for superficial fluorescence from dust. If not stated differently, all resulting fluorescence images were normalized to the maximum value of the fluorescence image excited with 670 nm and smoothed by spatial filtering (two-dimensional digital filter, structuring element circle with a diameter of 10 pixels).

Before subtracting both preprocessed fluorescence images excited with $\lambda_1$and λ_2, respectively, the equalisation factor β was calculated using i)the RNOI approach and ii) the histogram equalisation as described in sections 2.2.2.1 and 2.2.2.2 above. The difference $\Delta\tilde{I} = I_{\lambda_2}^{fluo}$ - $\beta\cdot$ $I_{\lambda_1}^{fluo}$ was then calculated and negative pixel values of the adapted subtraction image were set to zero.

2.2.3 Phantom Measurements

Two sets of phantom experiment have been conducted on tissue simulating phantoms: one to experimentally determine the optimal wavelengths for the surface-stripping algorithm when using the fluorophore Cy5.5, and another, with optimal wavelength choice, to demonstrate the general feasibility of the algorithm in an experimentally controlled setup.

2.2.3.1 Wavelengths Dependence

In cooperation with the Institute of Experimental Physics, Free University Berlin, we were able to test the wavelength dependence of the proposed algorithm experimentally.

A pulsed dye laser (Sulforhodamine 101 (LC 6600), Lambdachrome®, Lambda Physik AG, D-37079 Goettingen, Germany) with 10 Hz repetition rate, pumped by an 308 nm XeCl-Excimer radiation system, was used to excite a tissue phantom from 616 nm to 667 nm in 5 nm steps. The absorption spectra and laser characteristics of the dye can be found in [Brackmann, 2000]. Laser pulses had a full width at half maximum of 10 ns and an approximated power of 1 mJ.

A tissue phantom was prepared embedding a 4 mm long translucent polyethylene capsule (outer diameter of 0.93 mm, inner diameter of 0.58 mm, net volume 1 µl, SIMS Portex Ltd, Kent, UK) containing 10^{-11}mol of the fluorophore Cy5.5-PEG (molecular weight 23 kDa) beneath about 4 mm of pork meat (gammon). An additional top layer of fluorophore concentration (Cy5.5-PEG) was added by shortly placing and then peeling off a piece of napkin soaked with 1 ml Cy5.5-solution (approx. 10^{-7}mol Cy5.5). Figure 2.7 sketches the measurement setup.

To account for wavelength dependent intensity differences of the laser, all fluorescence images were divided by the respective excitation image acquired without 710 nm fluorescence filter.

2.2.3.2 Feasibility of the Algorithm

A 2 mm long translucent polyethylene capsule (outer diameter of 0.61 mm, inner diameter of 0.26 mm, net volume 0.1 ml, SIMS Portex Ltd, Kent, UK) containing 10^{-12} mol of the fluorophore Cy5.5 (Cy5.5-dextran, Nanocs, New York, NY) was embedded beneath one or two layers of pork meat (cutlet, 4 mm each) with and without an additional top layer of fluorophore concentration (Cy5.5-dextran, Nanocs, New York, NY) which was added as described in Subsection 2.2.3.1 above (see Figure 2.9).

2.2.4 Computer Simulations

The algorithm presented here does not rely on the knowledge of sensitivity factors $S_{\lambda_i}^{fluo}$. However, to estimate the penetration depth for different excitation wavelengths, Monte Carlo simulations were performed using a simulation software developed by L.Wang and S.Jacques [Wang and Jacques, 1992, Wang et al., 1995, Wang et al., 1997].

2.2.4.1 General Introduction to Monte Carlo Methods

Similar to the connection Albert Einstein found between the macroscopic physical properties of diffusion and the stochastic microscopic motion of particles [Einstein, 1905], the macroscopic optical properties of scattering and absorption in turbid media are linked to the stochastic nature of photon propagation through tissue.

Monte Carlo (MC) simulations are based on the macroscopic properties that are assumed to extend uniformly over small units of tissue volume. The scattering coefficient (μ_s) and the absorption coefficient (μ_a) are defined as the probability of photon scattering and absorption per unit pathlength, respectively. Usually, MC simulations do not treat the photon as a wave phenomenon because phase and polarization are quickly randomized after multiple scattering events, and their role in energy transport can be neglected.

Photon propagation in MC simulations is expressed through probability distributions that describe for instance the step size of photon movement between consecutive sites of photon-tissue interaction, or the angles of deflection in a photon's trajectory when a scattering event occurs. They estimate how photon migration is distributed in a certain media (tissue) after launching a large number of independent random trials instead of solving the analytical model to the underlying system explicitly [Rubinstein and Kroese, 2011].

MC methods can be applied to arbitrarily complex geometries and tissue parameter distributions [Hebden et al., 1997]. Though costly in computational time, they have become the gold-standard in cases where accurate methods are required and where solving the general analytical model, i.e. the radiative transfer equation (RTE), is non-trivial [Hielscher et al., 1998]. Moreover, MC simulations are the method of choice where the diffusion approximation to the RTE fails, for example in regions near the light source or cases where voids or low-scattering regions are present [Jacques and Pogue, 2008].

Sampling Random Variables in a Monte Carlo Simulation

The stochastic nature of photon scattering and absorption is simulated by the random sampling of variables from well-defined probability distributions (Monte

Carlo - "throwing the dice"). Several realisation possibilities exist to calculate a photon's trajectory from the tissue's optical properties and random numbers [Arridge et al., 1995, Kalos and Whitlock, 2008, Lux and Koblinger, 1991].

In the following, the implementation of the applied MCML program by [Wang et al., 1995] is summarized for sampling random variables in MC st .
For any random variable χ there is a probability density function that defines the distribution of χ over the interval (a, b), such that:

$$\int_a^b p(\chi)d\chi = 1 \tag{2.16}$$

Given a pseudo-random number generator provided by a computer, a random variable ξ can be generated which is uniformly distributed over the interval $(0, 1)$. The cumulative distribution function(Equation (2.11)) of ξ is then characterized by:

$$\begin{aligned} F_\xi(\xi) = \int_{-\infty}^{\xi} p_\xi(\xi')d\xi' &= 0 \quad \text{if} \quad \xi \leq 0 \\ &= \xi \quad \text{if} \quad 0 < \xi \leq 1 \\ &= 1 \quad \text{if} \quad \xi > 1. \end{aligned} \tag{2.17}$$

To randomly sample the generally non-uniformly distributed function $p_\chi(\chi)$ with the uniformly-distributed random variable ξ, a transformation function

$$\tau = T(\chi) \tag{2.18}$$

is chosen such that the corresponding probability density function $p_\tau(\tau)$ is uniform, too:

$$F_\tau(\tau) = \int_{-\infty}^{\tau} p_\tau(\tau')d\tau' \tag{2.19}$$

$$\begin{aligned} \text{with} \quad p_\tau(\tau) &= 0 \quad \text{if} \quad \tau \leq 0 \\ &= 1 \quad \text{if} \quad 0 < \tau \leq 1 \\ &= 0 \quad \text{if} \quad \tau > 1. \end{aligned} \tag{2.20}$$

The distributions $p_\tau(\tau)$ and $p_\xi(\xi)$ can then be exchanged and

$$F_\tau(\tau_1) = F_\xi(\xi_1) = \tau_1 = \xi_1 \quad \text{for} \quad \tau_1, \xi_1 \in (0, 1). \tag{2.21}$$

As is described in subsection 2.2.2.2, the cumulative probability distribution func-

tion $F_\chi(\chi)$ (Equation (2.11)) represents such a transformation $\tau = T(\chi)$ that yields a uniform probability distribution:

$$T(\chi_1) = F_\chi(\chi_1) = \int_a^{\chi_1} p(\chi) d\chi \quad \text{for} \quad \chi_1 \in (a, b) \tag{2.22}$$

Considering Equation (2.21) it follows that

$$F_\chi(\chi_1) = F_\xi(\xi_1) \quad \text{for} \quad \chi_1 \in (a, b) \quad \text{and} \quad \xi_1 \in (0, 1). \tag{2.23}$$

Employing Equation (2.22) for the left-hand side and Equation (2.17) for the right-hand side, Equation (2.23) converts into:

$$\int_a^{\chi_1} p_\chi(\chi) d\chi = \xi_1 \quad \text{for} \quad \xi_1 \in (0, 1), \tag{2.24}$$

which is then solved for χ_1 to receive the function $\chi = T^{-1}(\xi)$.

2.2.4.2 Sampling Photon Propagation with MCML

The MCML software used here [Wang and Jacques, 1992, Wang et al., 1995, Wang et al., 1997] propagates photons in three dimensions and records photon deposition (absorption), A(x, y, z) in J/cm^3, due to absorption in each grid element of a spatial array.

The probability density function of the step size of photon movement (s) between consecutive sites of photon-tissue interaction (scattering or absorption) is given by [Wang et al., 1995]:

$$p(s) = (\mu_s + \mu_a) e^{-(\mu_s + \mu_a)s}. \tag{2.25}$$

Using this distribution in Equation (2.24) gives an expression for a sampled value, s_1, based on the random number ξ:

$$\begin{aligned} \xi &= \int_0^{s_1} p(s) ds \\ &= \int_0^{s_1} (\mu_s + \mu_a) e^{-(\mu_s + \mu_a)s} ds \\ &= 1 - e^{-(\mu_s + \mu_a)s_1} \end{aligned} \tag{2.26}$$

Solving for s_1 yields:

$$s_1 = \frac{-ln(1 - \xi)}{(\mu_s + \mu_a)}, \tag{2.27}$$

or substituting ξ by $(1-\xi)$ due to the symmetry of ξ around 0.5:

$$s_1 = \frac{-ln(\xi)}{(\mu_s + \mu_a)}. \tag{2.28}$$

The direction of movement $\vec{e_r}$ in polar coordinates can be simulated by statistically sampling an deflection angle, $\theta \in [0, \pi)$, and an azimuthal angle, $\Psi \in [0, 2\pi)$. The probability distribution for the cosine of the deflection angle in biological tisse, $\cos(\theta)$, is proportional to the Henyey-Greenstein phase function that was originally proposed for galactic scattering [Henyey and Greenstein, 1941, Jacques et al., 1987]. The probability distribution $p(\cos(\theta))$ as implemented in the used MCML program is given by:

$$p(\cos(\theta)) = \frac{1-g^2}{2\ (1+g^2-2g\cos(\theta))^{3/2}}\ , \tag{2.29}$$

where g is the anisotropy factor that equals the expected value $\langle\cos(\theta)\rangle$. For isotropic scattering g is equal to 0, while and a value near 1 indicates very forward directed scattering.

Applying Equation (2.29) to Equation (2.24), the choice for $\cos(\theta)$ can be expressed as a function of the random number ξ:

$$\begin{aligned} \cos(\theta) &= \frac{1}{2g}\left(1+g^2-\left[\frac{1-g^2}{1-g+2g\xi}\right]^2\right) \quad \text{if} \quad g>0 \\ &= 2\xi - 1 \quad \text{if} \quad g=0. \end{aligned} \tag{2.30}$$

The azimuthal angle,Ψ, is uniformly distributed over $(0, 2\pi)$ and can therefore be sampled from ξ as:

$$\Psi = 2\pi\xi. \tag{2.31}$$

The new position of a photon that has been at position $\vec{r_0}$ in the medium is given by:

$$\vec{r_1} = \vec{r_0} + s_1\vec{e_r}. \tag{2.32}$$

Usually, the simulated photon (or photon package) has an initial direction perpendicular to the medium's surface corresponding to an infinitely narrow photon beam perpendicularly incident on the tissue. To consider absorption, it is assigned an initial weight $W = 1$, which is decreased after each step by the fraction ΔW that is deposited in the local grid element. The amount of absorbed and therefore deposited photon weight can be calculated as:

$$\Delta W = W\frac{\mu_a}{\mu_a + \mu_s} \tag{2.33}$$

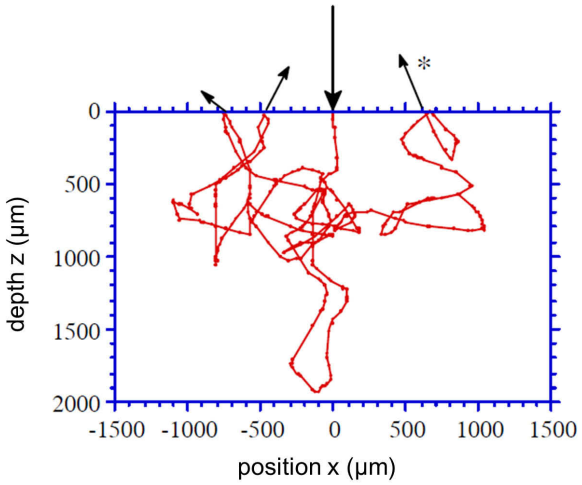

Figure 2.5: *Example of photon propagation through tissue as calculated from Monte Carlo simulations. The photon positions of a perpendicularly incident photon propagating through a homogeneous medium are marked as dots. Approaching the surface, only a part of the photon weight continues after being internally reflected. The other part is refracted and escapes. The asterisk (*) indicates the termination of the simulation in this example. The figure is adapted from [Wang and Jacques, 1992].*

During the MCML simulation, the total accumulated photon weight $A(x, y, z)$ absorbed in each local grid element is updated and stored:

$$A(x, y, z) = A(x, y, z) + \Delta W. \tag{2.34}$$

If the photon hits a boundary of the tissue, for example the air/tissue interface, then it may either escape or be internally reflected. This can be determined by comparing a random number ξ with the internal reflectance R at the incident angle α_i:

$$\begin{aligned} &\text{If} \quad \xi \leq R(\alpha_i), \text{ then the photon is internally reflected;} \\ &\text{if} \quad \xi > R(\alpha_i), \text{ then the photon escapes the tissue.} \end{aligned} \tag{2.35}$$

R can be calculated from the Fresnel formulas [Born and Wolf, 1986, Hecht and Zajac, 1998] and is given by the mean intensity reflection in the parallel and the perpendicular polarisation direction:

$$R(\alpha_i) = \frac{1}{2}\left[\frac{\sin^2(\alpha_i - \alpha_t)}{\sin^2(\alpha_i + \alpha_t)} + \frac{\tan^2(\alpha_i - \alpha_t)}{\tan^2(\alpha_i + \alpha_t)}\right], \tag{2.36}$$

	$\lambda\ (nm)$	$\mu a\ (mm^{-1})$	$\mu s\ (mm^{-1})$
Excitation	670	0.014	20
	633	0.027	22
Fluorescence emission	710	0.0095	18

Table 2.1: *Optical properties used in the MCML simulations [Wang and Jacques, 1992, Wang et al., 1995, Wang et al., 1997]. Scattering coefficients are adapted from in vivo measurements published by [Bourayou et al., 2008].*

where the angle of transmission α_t can be calculated from the refractive indices of the media that the photon is coming from, n_i, and transmitted to, n_t, by Snell's law:

$$n_i \sin(\alpha_i) = n_t \sin(\alpha_t). \tag{2.37}$$

An example of a photon trajectory in a homogeneous medium taken from [Wang and Jacques, 1992] is illustrated in Figure 2.5. The photon positions are demarked as dots and each step in between is randomly sampled. As the photon propagates through the tissue, its weight is decreased from an initial value of 1 and equals $1-(\mu_s/(\mu_a+\mu_s))^n$ after n steps inside the medium. When striking the surface, a fraction of the photon weight is refracted and the remaining weight continues to propagate after being internally reflected. The simulation is terminated when the photon weight drops below a certain threshold level. The asterisk (*) indicates the termination in this example, which occurred as the last significant fraction of photon weight escaped at the surface. Typically 10^4 to 10^6 photon trajectories have to be calculated to get a statistical photon distribution in the medium.

2.2.4.3 Simulation of Multispectral Excitation in Fluorescence Reflectance Imaging

First, the `mcml` program [Wang and Jacques, 1992, Wang et al., 1997] was used to consecutively simulate three point sources at 633 nm, 670 nm and 710 nm impinging on a slab, homogeneous half space (single layer). For every wavelength, 10^7 photons were simulated using a voxel width of 0.006 cm, and the anisotropy factor g was assumed to be 0.9. The optical properties chosen are summarized in Table 2.1. The scattering coefficients µs were approximated from *in vivo* measurements published in [Bourayou et al., 2008]. The used absorption properties µa correspond to a total hemoglobin concentration of 60 µmol/l, with an oxygen saturation of 70 %, dissolved in water based on the molar extinction coefficients published by Scott Prahl [Prahl, 2001].

Second, the corresponding convolution program `conv` [Wang and Jacques, 1992,

Wang et al., 1997] converted the point source solutions to yield responses to a finite photon beam with a radius of 0.03 cm for the 710 nm data and a flat beam geometry with a radius of 1.5 cm for the 633 nm and 670 nm results. Multiplying the results of a flat beam geometry at 633 nm and 670 nm, respectively, with that of the finite photon beam at 710 nm mimics the spread excitation of a light source in an FRI system and detection of fluorescence light with a camera system.

In this last step, the reciprocity theorem [Cristy, 1983] was used to reduce the number of simulations, taking into account that the sensitivity distribution is independent of which region is designated as source and which is designated as target. The obtained photon density curves reflect the desired depth dependent sensitivity (see Figure 2.8).

2.2.5 *In vivo* Application I: Mouse Model of Stroke (Capsule Implantation)

In vivo measurements were done with a mouse model described in detail in [Klohs et al., 2006]. In short, translucent polyethylene tubes (outer diameter of 0.61 mm, inner diameter of 0.26 mm, SIMS Portex Ltd, Kent, UK) were filled with a Cy5.5-PEG solution (MW = 23 kDa, Nanocs, New York, NY). The tubes were cut into lengths of 2 mm and then thermally sealed, containing a net volume of 0.106 µl and 10^{-12}mol Cy5.5. An experimental neurologist anaesthetised an adult male C57Bl6 mouse weighing 25 g (Bundesinstitut fuer Risikoforschung, Berlin, Germany) with a 5% solution of chloral hydrate (200 mg/kg) injected intraperitoneally. The hair was removed at the dorsal part of the head, the left temporalis muscle was detached, a hole was drilled into the skull and a capsule deposited at a depth of about 4 mm in the cortex of the left hemisphere approximately 2 mm caudal from bregma. The hole was closed using skin glue (Dermabond GmbH, Norderstedt, Germany) and muscle and skin were fixed into their original place. To investigate background fluorescence from fluorophores circulating in the vasculature, the mouse's tail vein was cannulated to allow a series of bolus injections to incrementally increase background fluorescence by subsequent intravenous injections of (0.2, 0.2, and 0.4) nmol Cy5.5-PEG. After each bolus injection, the fluorophore concentration in the blood increased to approximately (0.1, 0.2 and 0.4) µmol/l, assuming a total blood volume of 2 ml in the mouse. The dye conjugate was allowed to equilibrate for 1 min before NIRF imaging (Figure 2.10).

2.2.6 *In vivo* Application II: Mouse with Stroke

Finally, the 'non-invasive scalping' approach was tested *in vivo* in a mouse with induced cerebral ischemia (stroke). Middle cerebral artery occlusion was performed by the experimental neurology department of the Charité in a male C57Bl6/N

mouse as published in [Meisel et al., 2004,Klohs et al., 2008]. In detail, a monofilament was introduced into the common carotid artery under isoflurane anesthesia, advanced to the origin of the middle cerebral artery, and left there for 30 min, until reperfusion. Cerebral ischemia leads to an impairments of the blood-brain barrier (BBB) integrity because tight and adherend junctions of the cerebral endothelium malfunction under ischemia [Petty and Lo, 2002]. This enables an extravasation of plasma constituents, cells and molecular markers into the brain parenchyma, which do not pass the BBB under physiological conditions. An effective NIRF marker to image BBB impairment is fluorescently labeled albumin [Klohs et al., 2009b]. In our study, 0.1 mg Cy5.5 labeled albumin (20 µl of a 5% albumin solution with a Cy5.5 content of 387 nmol/ml, dissolved in 200 µl NaCl, German Cancer Research Center Heidelberg) were injected intravenously 96 h after re-perfusion. Cy5.5-albumin was allowed to circulate in the vasculature for 2 h after injection before NIRF imaging was performed. The mouse was then sacrificed under deep anesthesia and the brain was removed from the skull for *ex vivo* NIRF imaging (Figure 2.12). All procedures were in accordance with German animal welfare laws.

2.3 Results

2.3.1 RNOI and Histogram Equalisation

For molecular imaging studies the fluorescing inclusion has to be separated from the signal coming from the scalp. Adapted subtraction images resulting from the two proposed approaches of the non-invasive 'surface-stripping' algorithm are exemplarily shown in Figure 2.6. Both, the mean equalisation in a 'region not of interest' (subplot A) as well as the histogram equalised subtraction (subplot C) show very similar depth-weighted results for a mouse with an implanted fluorescent capsule. The calculated scaling factors β_{RNOI} and β_{HIS} are 1.28 and 1.26, respectively. The widespread fluorescence signal from the scalp, especially from the venal junction (compare Figure 2.3D,E) is highly reduced after the 'non-invasive scalping'. The implanted capsule can be seen with higher local contrast. In subplot C line profiles along a horizontal cut through the approximate capsule plane are presented. They illustrate a higher overall signal intensity for the fluorescence image excited with the deeper penetrating and more efficiently exciting 670 nm wavelength compared to 633 nm (see Figure 2.1). Furthermore, it can be seen that the capsule's signal strength relative to the mean signal level is higher for 670 nm. The line profile of the β_{RNOI} weighted 633 nm image (black dashed line) shows that the signal level on the contralateral hemisphere (pixel in x-direction $\geq$ 125), where mainly superficial fluorescence is expected, are now of equal strength as in the 670 nm image.

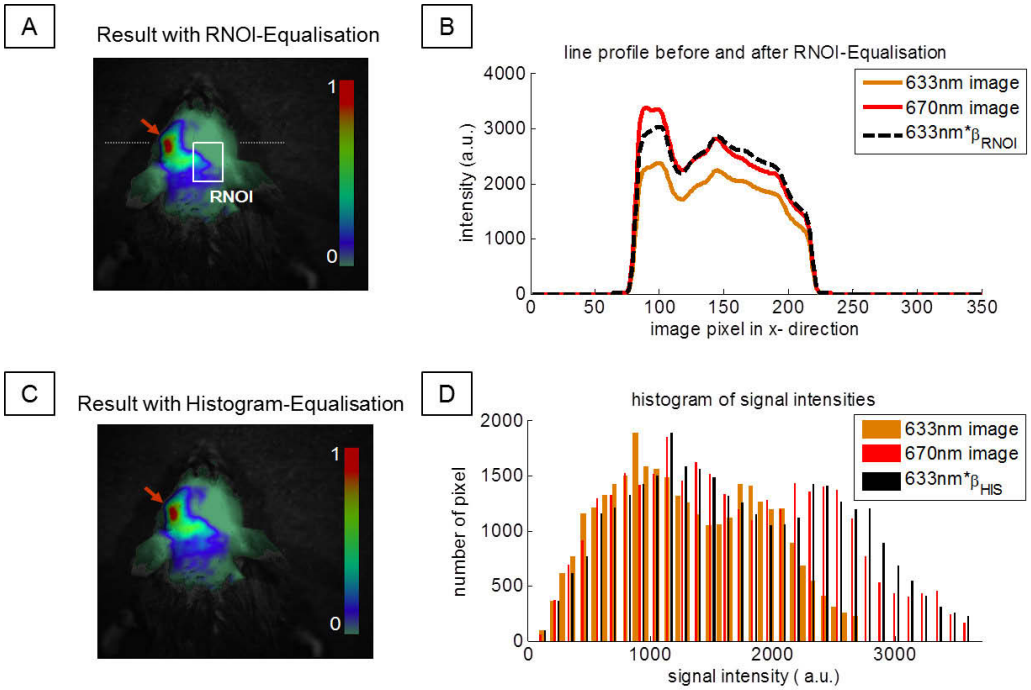

Figure 2.6: *RNOI and histogram approach. Resulting adapted subtraction images after the surface-stripping algorithm using (A) mean equalisation in a 'region not of interest' (RNOI) and (C) histogram equalisation for the in vivo fluorescence imaging data shown in Figure 2.3. Red arrows indicate the signal of the implanted fluorescent capsule. Fluorescence images are shown in a normalized colour-coded manner and projected onto the excitation image of the mouse head acquired without 710 nm fluorescence filter. B: Intensity profiles along a horizontal cut through the fluorescence images at the approximate capsule plane indicated by the white thin line in image A. D: Signal intensity histograms of the fluorescence images with 670 nm and 633 nm excitation wavelength (red and orange, respectively) and the rescaled histogram of the latter (black). In this case, multiplying the 633 nm image with the factor $\beta_{HIS} = 1.26$ best equalizes the histograms of both fluorescence images taken.*

2.3.2 Results: Wavelength Dependence

Figure 2.2.3.1 shows fluorescence images and surface-stripped results for a tissue phantom excitated with various wavelengths increasing from 616 nm to 667 nm. Without the superficial fluorescent layer, the fluorescence image shows a strong and focal signal at the sight of the embedded inclusion only (subplot B). Adding a fluorescent top layer increases background fluorescence and causes additional blur (subplot C). The fluorescent inclusion is still apparent for every excitation wavelength tested; however, its fluorescence signal is largest for 667 nm excitation wavelength, which is least absorbed in tissue and moreover the peak excitation wavelength of the fluorophore Cy5.5 (compare Figure 2.1). RNOI and HE approach of the surface-stripping algorithm lead to very similar results for the tissue phantom (subplot D,E). Both approaches show best image contrast for the inclusion when choosing 635 nm and 667 nm excitation light. Adapted subtraction of fluorescence images excited above 640 nm from the 667 nm image leads to a cancellation of almost all fluorescence signal from the inclusion as well as the background. In these cases, the wavelength dependent differences in penetration depth are too small to leave sufficient subtraction contrast. For excitation light lower than 625 nm, an RNOI or histogram equalised image subtraction also leads to a simultaneous cancellation of background and target fluorescence. Here, the adapted subtraction results in negative pixel values in the area of the inclusion, which are set to zero in the surface-stripping procedure. For all further phantom and *in vivo* measurements, the small animal imaging system described in Subsection 2.2.2.3 was used with 670 nm and 633 nm excitation wavelengths.

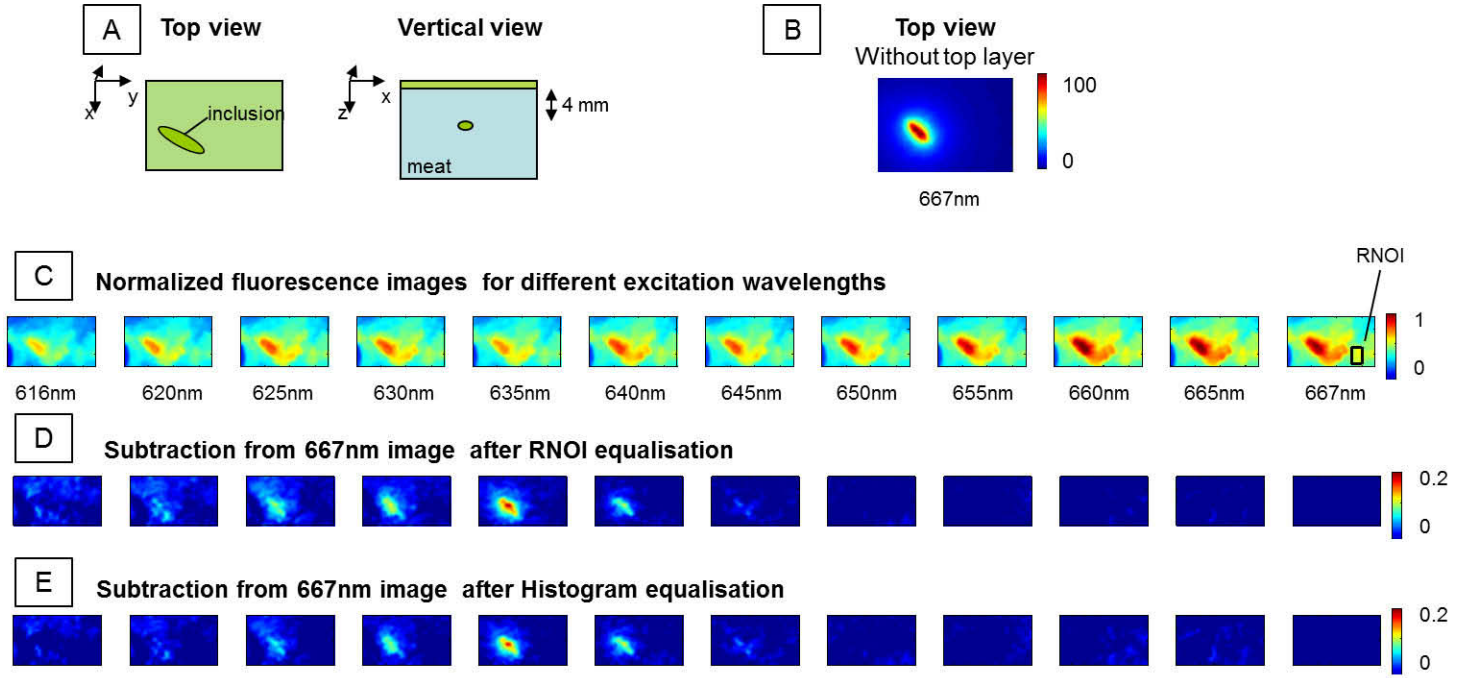

Figure 2.7: *Wavelengths dependence of the algorithm. A: Sketch of the tissue phantom in top and vertical view. B,C: Top view fluorescence images of a fluorescent capsule (10^{-11} mol Cy5.5) embedded in meat in 4 mm depth with (C) and without (B) a thin fluorophore film (Cy5.5-PEG) added on top to increase background fluorescence. C: Acquired fluorescent images excited with 616 nm to 667 nm, respectively, each divided by the respective background image acquired without the fluorescence filter and normalized to the maximum intensity of the 667 nm image. D, E: Resulting images after the surface-stripping algorithm either obtained with the RNOI equalisation approach (D) or the histogram equalisation (E), respectively. All fluorescence images are in arbitrary units (a.u.). Neighboring images are equally scaled as indicated by the corresponding color bar on the right.*

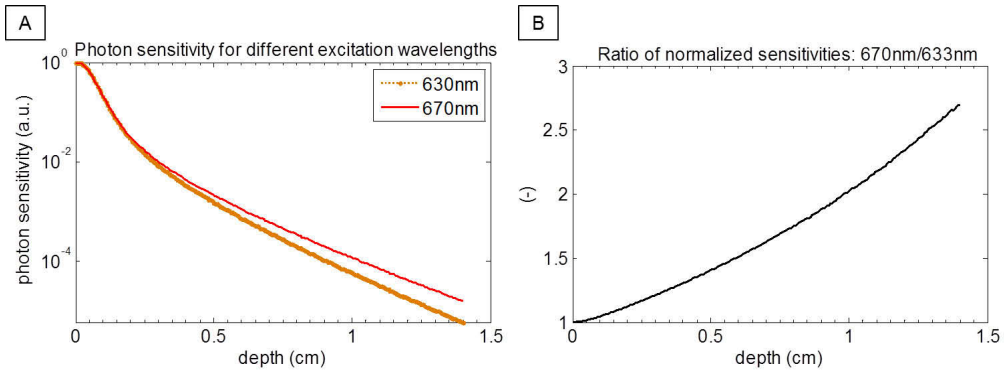

Figure 2.8: *Monte Carlo simulation results. A: Normalized sensitivity in a logarithmic scale as a function of depth for a point inclusion fluorescing at 710 nm, spread excitation beams at 633 nm and 670 nm and a point-wise detection. This mimics the spread excitation of a fluorescent source in an epi-fluorescence imaging system and the detection with a camera system. B: Ratio of the normalized sensitivities shown in A. Adapted from [Piper et al., 2010].*

2.3.3 Simulation Results

The Monte Carlo results in Figure 2.8 demonstrate the decrease in photon sensitivity with increasing depth for a point inclusion fluorescing at 710 nm and a point-wise detection when excited with spread excitation beams at 633 nm and 670 nm. Furthermore, they illustrate the very high sensitivity of epi-illumination imaging for dye concentrations in superficial layers. The ratio of normalized sensitivities shows that the difference in inclusion signal intensity between both excitation wavelengths grows exponentially with depth (Figure 2.8B). At an inclusion depth of 0.5 cm the fluorescence image excited with 670 nm is about a factor 2 more sensitive to the inclusion than the corresponding image excited with 633 nm, considering the same number of fluorescence photons being released by both excitation wavelengths.

2.3.4 Results: Phantom Measurements

Figure 2.9 shows normalized NIRF images and the 'surface-stripped' results of a capsule containing 10^{-12}mol of the NIR fluorochrome Cy5.5 embedded in pork meat. In all experimental setups, target localization is improved and a reduction of the effect of superficial layers can be observed after the surface-stripping algorithm is applied. RNOI and HE approach lead to similar scaling factors β (compare Table 2.2) and therefore to similar resulting images. In minor depth (1st row), the proposed algorithm only reduces the originally widespread fluorescence signal of the capsule leading to a more focal appearance compared to the 670 nm image. At a depth of 8 mm (2nd row), the capsule cannot be univocally localized on the 670 nm NIRF image without prior knowledge. This is eased in the resulting images. The same is true when a NIRF dye solution is applied topically to increase the fluorescence at the very surface of the phantom (bottom row). Here, the 8 mm deep inclusion is only observable after the surface-stripping algorithm. The residual fluorescence signal is not as symmetrically distributed as in the first two cases but still clearly localized.

2.3.5 Results *In vivo* I: Mouse Model of Stroke (Capsule)

In vivo results of a mouse with a surgically implanted fluorescent capsule and incrementally increasing background fluorescence are shown in Figure 2.10. Again, RNOI and HE approach lead to similar scaling factors β (compare Table 2.2) and therefore to similar surface-stripped images.

Without additional fluorophore circulating in the vasculature, the fluorescent inclusion is distinctly visible in both fluorescence images taken as well as in the resulting subtraction images. Multiple injections of a Cy5.5 labelled conjugate lead to an increasing additional signal from the confluens sinuum (confluence of superior sagittal and transverse venous sinuses) in the fluorescence images excited with 670 nm and 633 nm, respectively. Especially for the less penetrating 633 nm excitation light, the latter is dominating over the entire contralateral hemisphere. This ubiquitous physiological 'noise' is highly reduced after the 'non-invasive scalping'. However, a residual signal of increasing strength occurs in both the RNOI and the HE approach when the amount of injected conjugate is beyond 0.2 nmol. As long as the fluorophore concentration in the blood is below 0.4 µmol/l (8 nmol injected Cy5.5-PEG) the rather diffuse fluorescence signal of the raw images is focused and localized to the area overlying the implanted capsule. When the dye concentration in the blood exceeds 0.4 µmol/l, fluorescence of the capsule is outweighed by the signal originating from the venal junction (4th row, Figure 2.10).

In Figure 2.11, size and location of the RNOI are arbitrarily varied to illustrate

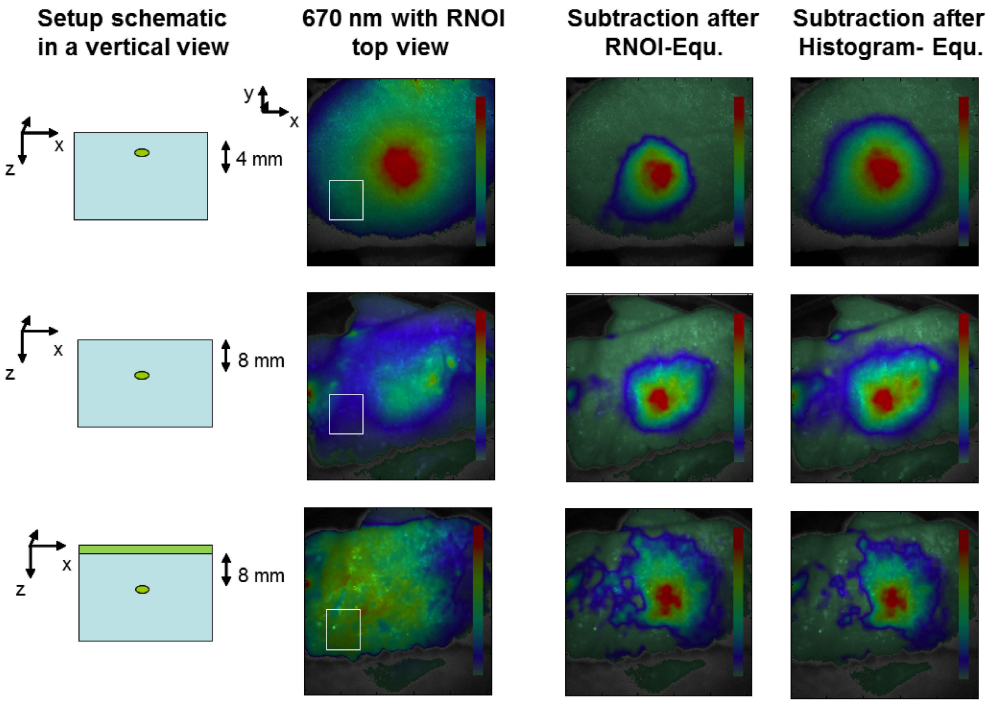

Figure 2.9: *Results tissue phantom. Top view fluorescence imaging data of a tissue phantom with a fluoroscent dye in a capsule embedded in 4 mm (1st row) and 8 mm (2nd and 3rd row) depth. In the last row a thin fluorophore film (Cy5.5-dextran) is added on top of the phantom to simulate background fluorescence of the scalp. The first column sketches the phantom in a vertical view. The second column shows the normalized NIRF image with 670 nm excitation wavelength projected onto a grey-scale background image of the phantom. Third and fourth columns: normalized overlays of the obtained surface-stripping results after RNOI and histogram equalisation, respectively. White squares delineate the used RNOI. FOV: 5 × 5 cm^2. Colorbars indicate normalized amplitudes between [0 1] in arbitrary units.*

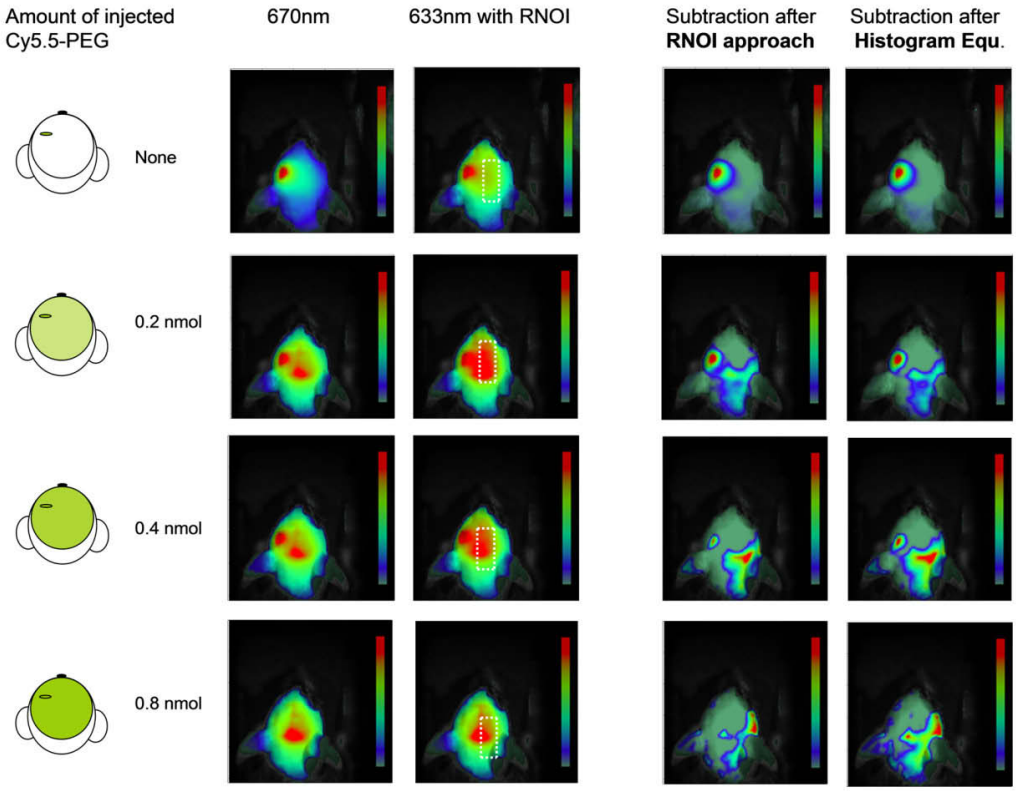

Figure 2.10: *Results in vivo imaging I: implanted capsule and increasing background fluorescence. In vivo fluorescence imaging data of a mouse head with implanted fluorescent capsule in the left hemisphere and with multiple additional venal injections of 0.2 nmol Cy5.5-PEG. The first column sketches the measurement situation. The second and third column show normalized fluorescence images taken with 670 nm and 633 nm excitation wavelengths, respectively, projected onto a grey-scale background image of the mouse head. White dotted squares depict the RNOI used for the RNOI approach of the surface-stripping algorithm. The last two columns show subtraction results after RNOI-mean equalisation and histogram equalisation, respectively. Colorbars indicate normalized amplitude between [0 1] in arbitrary units.*

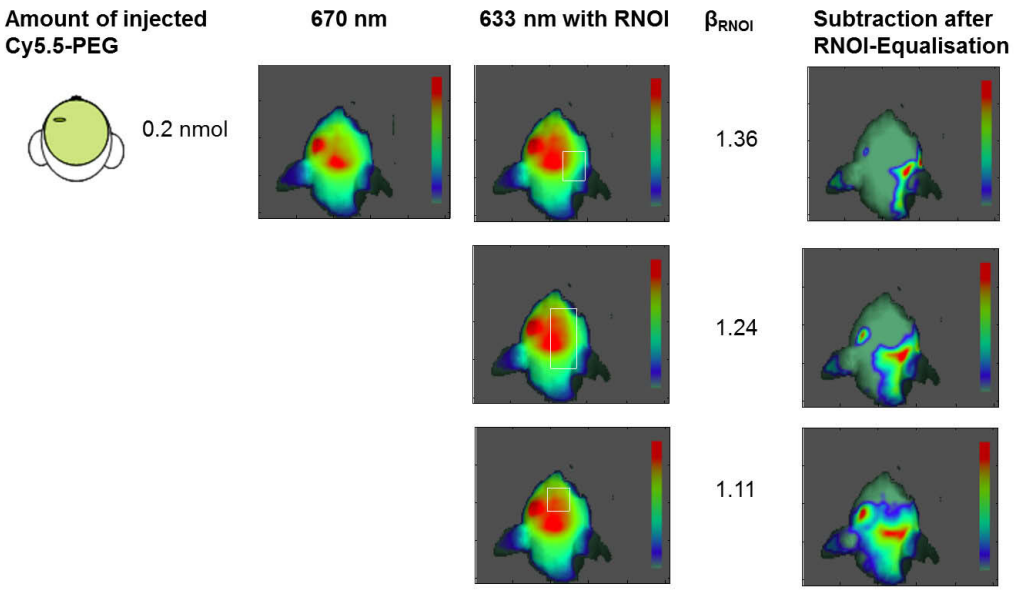

Figure 2.11: *Subtraction results depending on the choice of the region not of interest (RNOI). In vivo fluorescence imaging data of a mouse with implanted fluorescent capsule in the left hemisphere and with one additional venal injections of 0.2 nmol Cy5.5-PEG before and after the surface-stripping algorithm. The first column sketches the measurement situation. The second and third column show fluorescence images taken with 670 nm and 633 nm excitation wavelengths, respectively, and white squares depict different RNOI choices. The last column shows the resulting subtraction image after RNOI-mean equalisation. Colorbars indicate normalized amplitude between [0 1] in arbitrary units.*

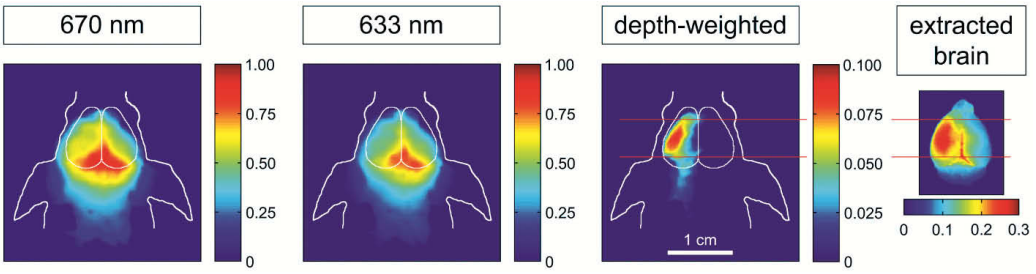

Figure 2.12: *In vivo results stroke. Non-invasive NIRF images of a living mouse after experimentally induced cerebral ischemia in the left hemisphere 2 h after i.v.-injection of NIRF-labeled albumin. Image taken from Ref. [Piper et al., 2010].*

how the resulting subtraction image can differ depending on the chosen RNOI. In this example, the reduction of superficial background signal increases with increasing scaling factor β_{RNOI}. Nevertheless, the target signal from the implanted capsule is also reduced more prominently, thereby diminishing the contrast improvements of the algorithm.

2.3.6 Results *In vivo* II: Mouse with Stroke

Figure 2.12 demonstrates how the presented algorithm can facilitate the detection of a fluorescent compound accumulating in diseased brain tissue in a living mouse suffering from stroke. After experimentally inducing cerebral ischemia, fluorescently labeled albumin, a marker for blood-brain barrier disruption, was injected intravenously. No detected fluorescence signal could be primarily attributed to the ischemic hemisphere at 670 or 633 nm excitation wavelengths. Both images are dominated by the centered fluorescence signal from the confluens sinuum. After use of the 'non-invasive scalping' approach, here shown after histogram equalisation, a focal NIRF signal emerges in the depth-weighted image, which corresponds well with the location of the fluorescence over the ischemic area on the *ex vivo* image taken after extracting the brain.

The scaling factors β for all experiments are given in Table 2.2. In most cases histogram equalisation led to very similar scaling values as the RNOI approach. Therefore, contrast improvement and imaging results are very similar for both approaches of the surface-stripping algorithm. However, depending on size and location of the chosen RNOI (Figure 2.11) the resulting subtraction images can differ greatly. This could be considered a drawback of the RNOI-approach compared to the automatically running histogram equalisation which does not require any additional manual input.

		$\beta_{\mathbf{RNOI}}$	β_{HIS}
Phantom study:	Inclusion depth 1 mm	1.866	1.210
	Inclusion depth 3 mm	1.686	1.458
	Inclusion depth 3 mm + layer of Cy5.5-dextran	1.733	1.759
in vivo I: capsule	No injection	0.571	0.579
	Injection 1	1.207	1.179
	Injection 2	1.303	1.192
	Injection 3	1.849	1.798
in vivo II: stroke		0.259	0.281

Table 2.2: *Scaling factors β obtained for RNOI and histogram equalisation approach of the surface-stripping algorithm.*

2.4 Discussion

The previous sections described and validated a new method to improve detectability and image contrast for non-invasive FRI reducing the contribution of unspecific fluorescence coming from superficial structures. While we focused on showing the usefulness of the presented surface-stripping approach in the particular case of cerebral ischemia in the murine brain, this technique is not restricted to cerebral target sites. The demonstrated subtraction algorithm could also be helpful in other experimental settings where the signal of interest clearly lays in deeper tissues, for example the kidney.

The principal idea of this spectral approach is to obtain two fluorescence images with different depth sensitivities by using two different excitation wavelengths. This capitalizes on the fact that higher variability in tissue optical properties is observed for excitation photons compared to emission photons [Chaudhari et al., 2009].

In practice, 633 nm and 670 nm have experimentally shown to be most suitable when the fluorochrome Cy5.5 is used (Figure 2.7). While the wavelength dependence was tested on a tissue phantom made of pork meat, *in vivo* measurements have a considerably higher hemoglobin content (especially when measuring through the intact scalp). Therefore, absorption dependent differences in penetration depth for different wavelengths are expected to be larger for *in vivo* measurements because light is more absorbed in well perfused tissue.

For excitation light lower than 625 nm the measured fluorescence emission intensity is considerably smaller compared to 670 nm excitation light. This is expected considering the wavelength dependent excitability of the fluorophore Cy5.5 (Figure

2.1). Moreover, when a relatively high number of Cy5.5 molecules is conjugated to a protein, a secondary absorbance peak at 600 nm occurs, which, however, is not converted to fluorescence [Berlier et al., 2003]. Even though differences in quantum efficiency for different excitation wavelengths are ruled out by the equalisation step of the surface-stripping algorithm, Cy5.5 fluorescence strength seems to be generally insufficient when excited below 625 nm.

Theoretically, however, an excitation below 615 nm seems desirable because absorption in tissue increases tremendously towards the orange and yellow wavelength range. If a NIR fluorophore would be available that is still excitable below 625 nm, the measurable emitted fluorescence would mainly originate from fluorochromes within the first millimetre of tissue. In this case, the target signal in deeper layers would probably be less reduced. Nevertheless, from a technical point of view it has to be mentioned that fairly inexpensive laser diodes are available with wavelengths around 630 nm and above. They can be easily handled and implemented into existing NIRF systems by simple fibre optics (section 2.2.2.3). Among the visible wavelengths, however, the generation of red emission seems more challenging and complicated [Harkonen et al., 2007]. Costly and elaborate laser optic installations would be required to realize a laser source with sufficient output power in the radiation range from 580 nm to 630 nm [Gerster et al., 2003]. Even though technically feasible, they are probably beyond the realm of possibility in most biomedical small animal research laboratories.

The experiments show that both, the suggested RNOI approach as well as the histogram equalisation, are well viable to determine the scaling factor β. The histogram equalisation as an automated data processing step seems favourable because it does not require a priori information about the location of the deep laying target. Furthermore, it is independent of modulations in the setup such as intensity changes of the excitation light or repositioning of the object within the camera's field of view.

The proposed RNOI equalisation, on the other hand, does require some fiddling as to where exactly place and what size to choose for the RNOI. The effect of superficial signal reduction varies depending on size and location of the arbitrarily chosen RNOI (see Figure 2.11). This, however, could also be beneficial because it leaves some freedom of choice to the investigator as to what extend superficial but also target signal components shall be reduced or not.

2.4.1 Limitations of the Surface-Stripping Algorithm

The optical NIR window as well as the specific absorption spectra of the fluorophore limit the spectral range of possible excitation wavelengths (compare Figure 2.1 and Figure 1.1). Therefore, depth sensitivities do not differ on a large scale between suitable excitation wavelengths. This inevitably leads to a reduction of

the target signal, too, because tissue penetration of the lower NIR wavelength is not confined to superficial layers. Moreover, the used FRI geometry does not allow to quantify how deep 'superficial' really is. To what extent the subtraction method also eliminates the signal of interest depends on the target's depth as the ratio of depth sensitivities increases with increasing depth (Figure 2.8). A fluorescent source of interest in a superficial layer, for instance in a tumor model where tumor cells may grow from the brain into the scalp, would be removed or at least strongly attenuated by the proposed surface-stripping approach.

Another crucial point to the method is its liability to artificial edge effects if the different fluorescence images are not adequately co-registered. Movements of the object between the different spectral measurements can lead to artefacts in the subtraction image. A fast image acquisition would limit movement artefacts. The current imaging system was not optimized for rapid switching between excitation and fluorescence image acquisition but this could be realized in future applications with a filter wheel. While simultaneous multi-wavelength imaging systems are inured to motion artefacts [Burgess et al., 2008, Yuan et al., 2009], they are not feasible for our application. Here, both excitation wavelengths excite the same fluorophore. The measured emission signal therefore cannot be spectrally re-assigned to the corresponding excitation wavelength which, however, is essential for the surface-stripping algorithm.

2.5 Conclusion

The presented surface-stripping algorithm enables visualization of fluorescent sources located deep in tissue layers where detection was previously hampered by strong fluorescence from superficial structures. In most experimental settings investigated, the application of this approach led to a considerable increase of contrast and an improved localization of the fluorescent source of interest by reducing superficial signal components. Yet, absolute quantification of the target's depth is not possible in reflectance imaging. The benefit might be little if background sources completely outweigh the signal of a deeper laying target or when the fluorescent source of interest merges into superficial layers. However, the technique can reveal fluorescent sources which would have escaped conventional NIRF reflectance imaging.

3 Time-Resolved Approach Resolving Depth for Planar Imaging with Time-Domain Measurements

3.1 Introduction

In this chapter explicit depth recovery in planar NIR fluorescence imaging is presented which makes use of time-resolved measurements. With the help of Monte Carlo simulations a straightforward method is validated to quantify the depth of a fluorescence inclusion in *in vivo* small animal imaging. Parts of this chapter have been submitted to the Journal of Physics in Medicine and Biology (Piper et al., Reference number PMB-100146).

3.1.1 Motivation: Sounding the Depth of Fluorescent Targets

Non-invasive near-infrared fluorescence (NIRF) imaging is increasingly being used to study physiology and pathophysiology in animal disease models [Ntziachristos, 2006,Leblond et al., 2010,Ntziachristos, 2010,Massoud and Gambhir, 2003] and in the preclinical evaluation of targets and specific ligands [Zhang et al., 2011,Hillman, 2007,Lu et al., 2013]. Although the trend is toward whole-body tomographic imaging systems that allow 3D image reconstruction and quantification of fluorescence particles, most *in vivo* small animal imaging is based on *planar* (2D) reflectance imaging [Leblond et al., 2010].

The lack of depth resolution is often considered a fundamental drawback in planar imaging. Moreover, the measured spatial fluorescent distribution on an object's surface could be the same, whether it originates from a small fluorescent source in a deep layer or a boarder fluorescent source with lower concentration in a superficial layer [Ntziachristos et al., 2003].

When measuring fluorescence intensity by a *single* cw light source and detector, it is impossible to decouple depth and concentration of the fluorophore, because both affect the measured intensity on the surface in a similar way [Hall et al., 2004,Keren et al., 2008]. A time-gated detection of fluorescence, on the other hand, contains enough information for a depth-resolved determination of absorption and

fluorescence changes within a *single* measurement [Steinbrink et al., 2001, Liebert et al., 2006].

It has been demonstrated that the time of flight $\langle t \rangle_{fl}$ of fluorescence photons coming from a fluorescent inclusion linearly correlates with the inclusion's depth for semi-infinite, non-fluorescent turbid media [Hall et al., 2004, Keren et al., 2008]. Therefore, it seems self-evident to make use of this linear dependency to determine the depth z by measuring the fluorescence photons' mean time of flight.

In *in vivo* small animal imaging, however, the object's geometry cannot be approximated as semi-infinite. Even more important, tissue auto-fluorescence or background fluorescence from unbound fluorophores circulating in the vasculature cannot be neglected. In the following sections of Chapter 3 the impact of a finite, heterogeneous geometry and moreover the influence of different levels of background fluorescence from the medium itself are investigated.

In homogeneous media, different slopes between $\langle t \rangle_{fl}$ and the depth of a fluorescent inclusion are expected depending on the optical properties of the object imaged. The slope of this linear relationship can principally be calculated from photon transport simulations or, potentially much more easily, determined by two independent measurements at different depths leading to a linear calibration curve for the individual setup. For the latter solution, one measurement could be a fluorescent object placed on top of the animal, in case of small animal imaging for example, and the second measurement with a fluorescent object placed below the animal.

The results suggest that determining the depth of an embedded fluorescent object by a straightforward linear calibration can be well feasible within the dimensions of a small animal.

3.1.2 Introduction to Time-Resolved Planar (Fluorescence) Imaging

Time-resolved or time-domain optical imaging measures the (fluorescence) emission as a function of time delay following a several femto to pico seconds long (excitation) laser pulse (see Figure 3.1A) [Patterson et al., 1989, Das et al., 1997, Cubeddu et al., 2002, Marcu, 2012]. Depending on the path length a photon has travelled through tissue, the time of flight t, that a photon needs until it emerges from the tissue surface, varies. The distribution of arrival times reflects the temporal point spread function (TPSF), which is the attenuated and broadened temporal distribution of photons after propagating through turbid media [Patterson et al., 1989].

When a pico second pulse of light is transmitted through several centimeters of soft tissue, the TPSF will extend over several nanoseconds [Hebden et al., 1997]. Time correlated single photon counting (TCSPC) systems, which are photon counting detectors measuring the flight times of individual photons relative

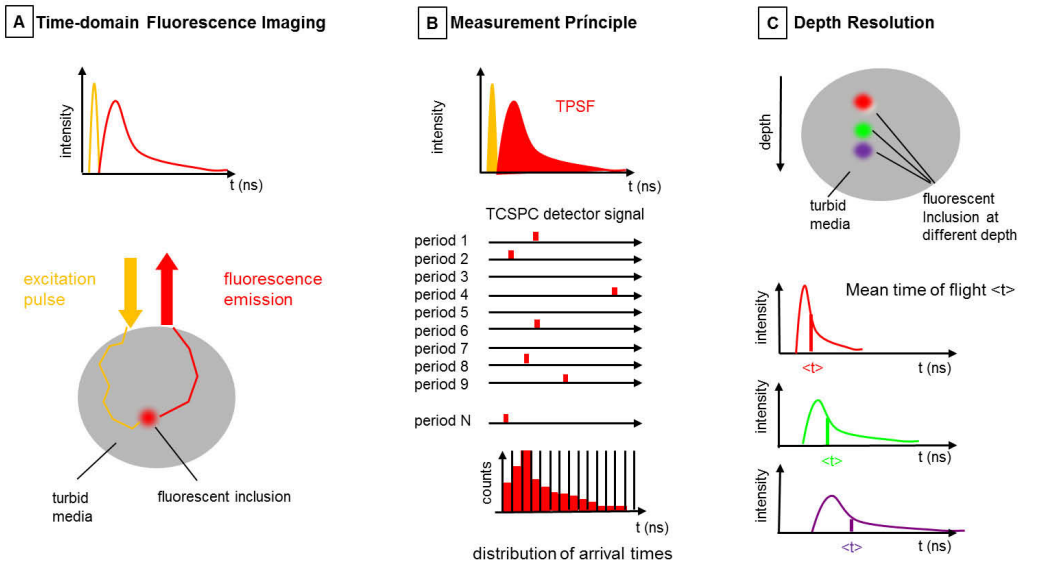

Figure 3.1: *Schematic of principles behind time-resolved fluorescence imaging. A: When a pico second pulse of light propagates through several centimeters of turbid media, the attenuated and broadened temporal distribution of (fluorescence) photons emerging from the surface will extend over several nanoseconds. B: The temporal point spread function (TPSF) of the fluorescence emission is acquired by counting detectors measuring the flight times of individual photons relative to a reference pulse. This is called conventional time correlated single photon counting (TCSPC). C: Depending on the depth of the fluorescence inclusion in a non-fluorescent medium, the time of flight distribution, measured at the surface, varies. Principally, the mean time of flight $\langle t \rangle$ correlates with the inclusion's depth [Hall et al., 2004, Keren et al., 2008].*

to a reference pulse, are the most commonly used technique to determine the TPSF [Lakowicz, 2009]. Excited by a high repetition rate laser light source, a histogram of photon arrival times is build-up which represents the TPSF as change of fluorescence intensity versus time (Figure 3.1B) [Marcu, 2012].

If the TPSF is measured accurately, high-resolution information can be extracted from its shape [Hebden and Delpy, 1994, Gibson et al., 2005]. By calculating different moments [Steinbrink et al., 2001, Liebert et al., 2003, Liebert et al., 2012] or the Laplace transform of the TSPF [Schweiger and Arridge, 1999], one can distinguish between tissue absorption and scattering properties inside the medium [Grosenick et al., 2003], or depth and concentration of a fluorophore (Figure 3.1C) [Hall et al., 2004, Keren et al., 2008], respectively.

The early arriving photons have travelled the shortest path through tissue and are assumed to have undergone only relatively few scattering [Wu et al., 1997,

Turner et al., 2005]. Photons with a late arrival time are delayed by a larger number of scattering events. Later photons, therefore, have been more influenced by NIR absorbers in tissue [Grosenick et al., 2003, O'Sullivan et al., 2012]. The decay of the TPSF can be used to extract the intrinsic fluorophore lifetime by means of multiple exponential fits without the need for reconstructions [Bastiaens and Squire, 1999, Bloch et al., 2005, Kumar et al., 2005]. This feature has given rise to fluorescence lifetime based imaging contrast (FLIM) which is sensitive to factors affecting molecular interactions or the local tissue environment such as pH, viscosity, oxygen concentration and tissue autofluorescence ([Kumar et al., 2005, Kumar et al., 2006, Becker, 2012].

3.2 Methods

3.2.1 The Monte Carlo eXtreme Software for Time-resolved Photon Migration

Planar time-resolved fluorescence reflectance measurements were simulated with the Monte Carlo eXtreme (MCX) software published by Fang and Boas [Fang and Boas, 2009]. In contrast to the MCML software applied in Chapter 2 for multi-spectral imaging with continuous-wave light on homogeneous medium, MCX allows to model *time-resolved* photon migration in *arbitrary* 3D turbid media. Moreover, the software accelerates the simulation time by computing many photon packages in parallel (see Figure 3.2) on the graphics processing units (GPUs), which represent an excellent shared memory parallel computing platform featuring extremely low memory latencies and hierarchical thread structures.

The MCX code is implemented with CUDA programming language [Nvidia, 2007], but has the option to be solely operated through MATLAB under the software package `MCXLAB`. Detailed installation instructions can be found under [MCX and MCXLAB, 2012] and http : //mcx.sf.net/cgi − bin/index.cgi?Doc/Installation.

MCX Work Flow of Simulating Photon Migration

Figure 3.2 illustrates the parallel work flow for simulating photon migration with the MCX software. Within each thread, photon propagation itself is similarly implemented as in the MCML software described in Section 2.2.4.3. With MCX, however, the fluence distribution $F(\vec{r}, t_i)$ under a unitary light source can be calculated for any user-specified time gate t_i and voxel $\vec{r}$ of the simulated volume.

For each repetition, the random number generator (RNG) of the GPU is reseeded using a RNG that runs on the central processing unit (CPU). The work flow can be summarized as follows:

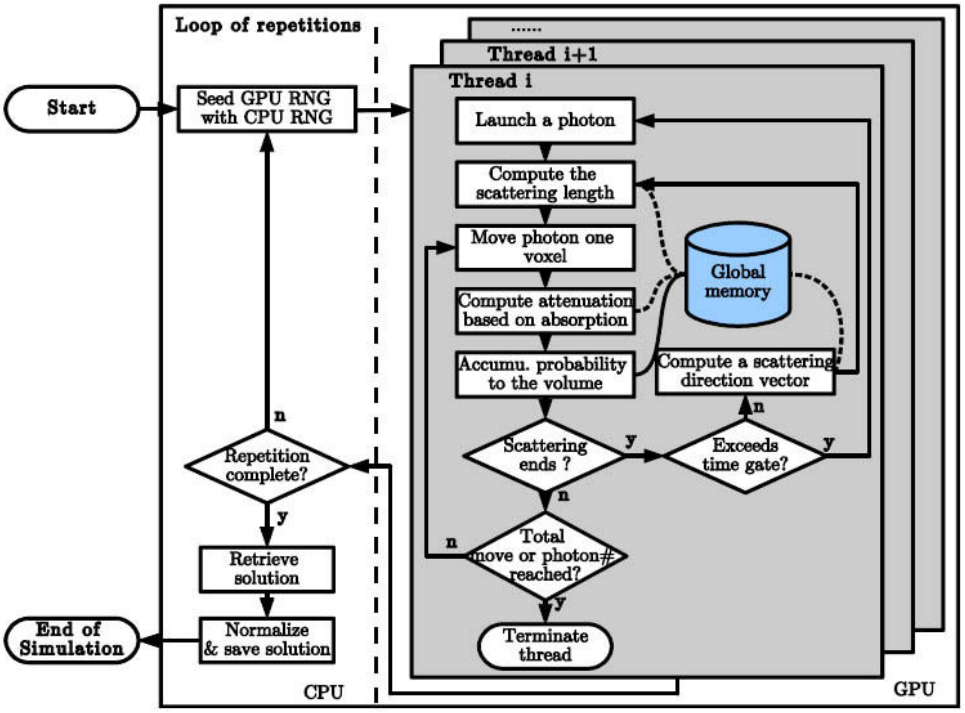

Figure 3.2: *Block diagram of the parallel work flow for simulating photon migration with the Monte Carle eXtreme software MCX. The curved dashed lines indicate read-only global memory access and curved solid lines read/write access. Figure is taken from [Fang and Boas, 2009].*

(1) At first, a photon (package) with an initial weight $W = 1$ is launched at the position of the source $\vec{r}_s$ along an incident direction $\vec{r}_0$.

(2) Then, the distance L to the next scattering event is computed using the absorption and scattering coefficients $\mu_a(\vec{r}_j)$ and $\mu_s(\vec{r}_j)$ of the current voxel $\vec{r}_j$ and a random number ξ according to equation (2.28).

(3) The photon (package) is moved *one voxel* along the scattering trajectory.

   a) If μ_s changes, the remainder of the scattering length L is renormalized [Wang et al., 1995]:

$$L_{new} = L\frac{\mu_s(\vec{r}_j)}{\mu_s(\vec{r}_{j+1})}. \tag{3.1}$$

   b) If the boundary of the medium is reached, the probability of an internal reflection $R(\alpha_i)$ is calculated from Fresnel's equation according to

Equation (2.36) and (2.35). If a reflection occurs, migration through the medium continues in the direction mirrored at the reflection interface and W is decreased by the fraction:

$$\Delta W_R = W \cdot R(\alpha_i). \tag{3.2}$$

c) If the photon leaves the medium in a detector location $\vec{r}_d$ at an refractive angle (Equation (2.37)) less than the predefined aperture of the detection fibre, then the photon is registered in the k^{th} time interval:

$$t_k < t_i < t_k + \Delta t \tag{3.3}$$

of the user-defined time gates. Furthermore, information is recorded in a history file identifying the detector and pathlength l_{ij} of the photon i and each passed voxel j prior to being detected [Boas et al., 2002]. The total time-of-flight is given by:

$$t_i = \sum_j \frac{l_{ij}}{c_j}, \tag{3.4}$$

where c_j is the speed of light in voxel j.

(4) The attenuation ΔW along this voxel step is computed and W is further decreased by the fraction:

$$\Delta W = W \frac{\mu_a(\vec{r}_{j+1})}{\mu_a(\vec{r}_{j+1}) + \mu_s(\vec{r}_{j+1})}. \tag{3.5}$$

(5) The current package weight W is accumulated to the current voxel's raw probability $P(\vec{r}_{j+1}, t_i)$, at the fixed time interval which is binned according to the user's specified time gates.

(6) Steps 3-5 are repeated until the photon has migrated the total scattering length L.

(7) The propagation stops and the trajectory ends, if the remaining scattering length is less than one voxel.

(8) A new scattering direction with the deflection angle θ and the azimuthal angle Ψ is calculated as a function of the random number $\xi \in (0, 1)$ according to Equations (2.30) and (2.31).

(9) The steps 2-8 are repeated until the photon exits the medium or reaches the maximum time gate t_{max}.

(10) The steps 1-9 are repeated until the predefined total number of package steps or the desired total number of photons is reached.

To get the final photon fluence $F(\vec{r},t)$, the dimensionless raw probability $P(\vec{r},t)$ accumulated in the medium is then normalized based on the energy conservation relationship in [Boas et al., 2002] by:

$$F(\vec{r},t) = P(\vec{r},t)\frac{E_a/E_t}{\sum_i \sum_j P(\vec{r}_j,t_i)\mu_a(\vec{r}_j)\Delta V \Delta t} \tag{3.6}$$

where E_a/E_t is the fraction of total energy being absorbed calculated from the tracked package weight for each photon, ΔV is the voxel volume and Δt is the time gate length.

Accumulating the photon probability into the corresponding time gates according to their respective time-of-flight yields a distribution (histogram) of arrival times similar to what can be measured by time-resolved single photon counting detectors:

$$N_k = \sum_{i*} \exp\left(-\sum_j \mu_{a,j} l_{i,j}\right) \tag{3.7}$$

where the summation over $i*$ includes only those photon packages that are detected in the kth time interval (Equation (3.3)).

Implementation Pitfalls

- The minimum graphic memory M required is given by:

$$M = V_x \cdot V_y \cdot V_z \cdot N_t \cdot 4 \text{ bytes} \tag{3.8}$$

  with V_x,V_y and V_z being the number of voxel along each direction of the entire volume to be simulated, and N_t being the total number of time gates.

- For non-dedicated graphic cards the graphics driver may exceed a kernel's run-time. As a result, the simulation aborts after a few seconds. In this case, it helps to simulate a smaller number of photons and to increase the number of repetitions instead. The graphic card can be further relieved by operating through the Linux text console instead of the graphical user interface.

- Another crucial point in the MCX work flow is step 5 where $P(\vec{r},t_i)$ is simultaneously updated from all active threads. The GPU may miss about 1 % of the accumulation events when many threads concurrently read and

write the same global memory location. The probability for this so called *race condition* is exponentially reduced with the distance from the source [Boas et al., 2002] and relates to [Nvidia, 2007]:

$$\frac{T(T-1)}{2} \int_V P_s(\vec{r},t) \cdot P_s(\vec{r},t) dr \tag{3.9}$$

with T being the number of active threads in a multi-processor, $P_s(\vec{r},t)$ is the solution for the media with scattering properties only ($\mu_a = 0$), and V is the volume of a voxel.

3.2.2 Derivation of the Sensitivity Distribution

A planar light source was approximated by using a grid of 104 × 55 directed point sources with a distance of one voxel between neighbouring sources. To simulate epi-illumination, the layer of sources was placed directly above the simulated medium. Initial direction of the photon packets was directed downwards. Overall fluence of the approximated planar source is then given by

$$F(\vec{r},t) = \sum_i F_i(\vec{r},t), \tag{3.10}$$

with F_i being the fluence for a single point source.

The reciprocity theorem [Cristy, 1983] was applied to calculate the sensitivity distribution of a fluorescent point source illuminated with a planar excitation source and detected by a single pixel of a camera system installed above. According to the theorem, the sensitivity distribution is independent of which region is designated as source and which is designated as target [Cristy, 1983]. Therefore, a point source was simulated in place of a detector. The acquired flux of the point source to a given time t is denoted as $D(\vec{r},t)$. Using convolution in the time-domain ($\times_t$), the desired sensitivity distribution $\Phi(\vec{r}, \mathrm{t})$ of the detected fluorescence photons, given a fluorescent object in voxel $\vec{r}$, is given by:

$$\begin{aligned} \Phi(\vec{r},t) &= F(\vec{r},t) \times_t D(\vec{r},t) \\ &= \sum_\tau F(\vec{r},\tau) \cdot D(\vec{r},t-\tau). \end{aligned} \tag{3.11}$$

Figure 3.3 illustrates how the reciprocity theorem was applied. Here, the fluence distribution of a planar source over a mouse head and the fluence distribution of a centered point source are displayed for different time windows from 25 to 775 ps. The last row depicts their pixel wise convolution in the time-domain, which yields the desired sensitivity distribution $\Phi(\vec{r}, \mathrm{t})$.

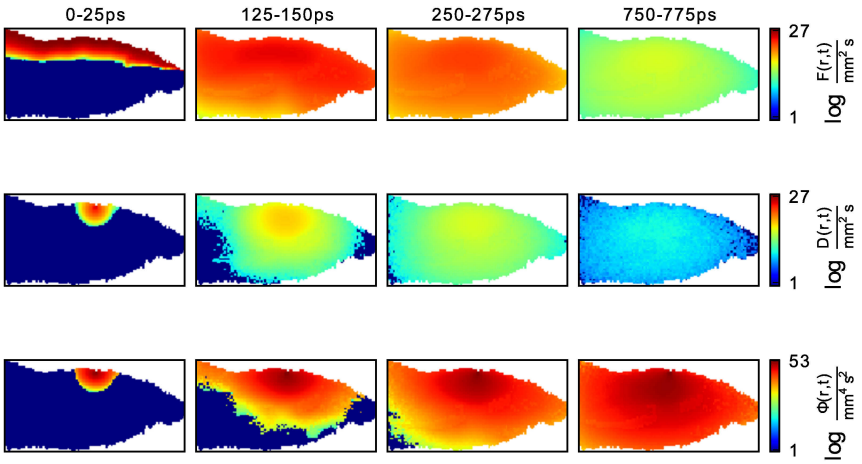

Figure 3.3: *Calculation of the sensitivity distribution using the reciprocity theorem [Cristy, 1983]. First row: Fluence distributions of a planar source over a mouse head geometry after 25, 150, 275 and 775 ps, integrated over 25 ps each, logarithmic scaling. Second row: Fluence distributions of a centered point source over a mouse head for the same time windows, logarithmic scaling. Last row: Convolution of the first two fluence distributions mimics the sensitivity distribution for a fluorescent point source illuminated with a planar excitation source and detected in a single pixel of a camera system.*

The first moment of the acquired distribution of fluorescence photons is then given by

$$\langle t \rangle_{fl} = \sum_i t_i \cdot \; p(\vec{r}, t_i) \tag{3.12}$$

with the probability mass function $p(\vec{r}, t_i)$ of this distribution being

$$p(\vec{r}, t_i) = \frac{\Phi(\vec{r}, t_i)}{\sum_j \Phi(\vec{r}, t_j)} \quad . \tag{3.13}$$

3.2.3 Simulated Scenarios

A total of 10^{11} photons and 190 time windows with 25 ps each were simulated for the entire planar source. Three different geometries with an isometric voxel size of 0.31 × 0.31 × 0.31 mm^3 were used:

(1) a semi-infinite medium (length × width × depth: 104 × 55 × 78 voxel),

(2) a cylinder with a diameter of 14.6 mm approximating the head of a small animal (length: 104 voxel, diameter: 47 voxel), and

(3) the anatomical geometry of a mouse head obtained by magnetic resonance imaging (7-T Pharmascan T2 sequence, voxel size $(0.31\ mm)^3$, Bruker, length × width × depth: 104 × 55 × 53 voxel). In analogy to [Bourayou et al., 2008] the MRI volume was segmented in *brain*, *other tissue* and *air*.

The sagittal and coronal views of all simulated geometries are shown in Figure 3.4.

The optical properties chosen (see Table 3.1) are taken from [Bourayou et al., 2008] and relate to a planar excitation source of λ_{ex} = 682 nm and a point fluorescence source of λ_{em}= 710 nm. These wavelengths correspond to the excitation and emission wavelength of the NIRF cyanine dye Cy5.5, which is commonly used in mice [Klohs et al., 2006, Klohs et al., 2008, Umezawa et al., 2009]. Its quantum yield in aqueous buffer is 0.28 [Umezawa et al., 2009], but was neglected in the simulations. Fluorescence photon absorption due to the fluorophore itself (quenching) was also neglected.

The semi-infinite medium was simulated with the homogeneous optical properties of *other tissue* (Table 3.1). In order to show the system's dependency on a sufficient signal-to-noise ratio (SNR),

(1) the semi-infinite medium was simulated twice:

a) with N=10^{11} photons, and

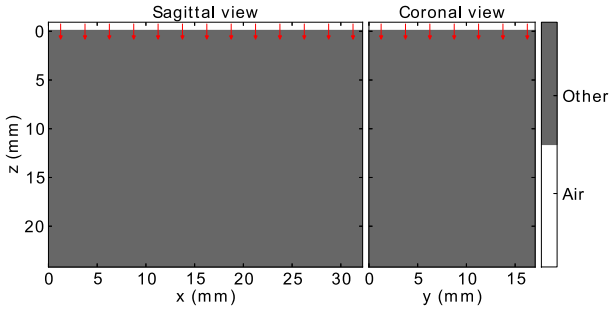

(a) semi-infinite medium

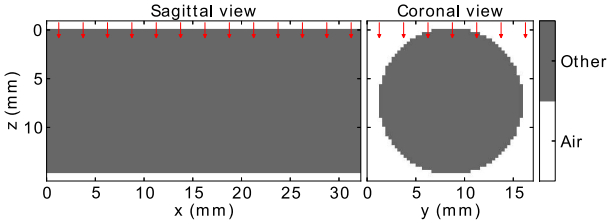

(b) cylindrical geometry

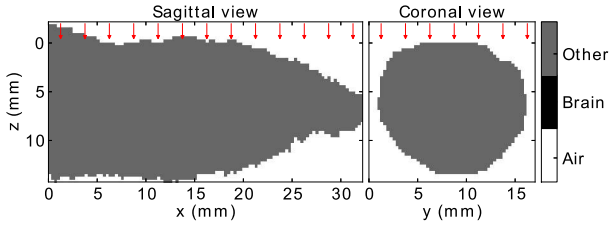

(c) homogeneous mouse head geometry

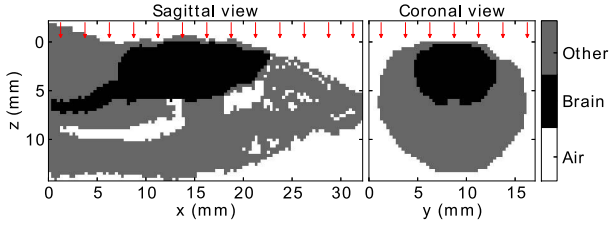

(d) heterogeneous mouse head geometry

Figure 3.4: *Schemes of the simulated, increasingly realistic geometries in a sagittal and coronal view.*

b) with considerably fewer photons (N=10^8), thereby reducing the SNR in deeper layers.

To demonstrate how the mean time of flight is altered depending on the optical properties of the medium,

(2) the cylinder with *homogeneous* optical properties was simulated four times:
   a) with the tabulated values of μ_a and μ_s for *other tissue*,
   b) with increasing μ_s to the values for brain tissue,
   c) with decreasing μ_a to the values for brain tissue, or
   d) varying both (Table 3.1).

To investigate the influence of *heterogeneous* optical properties,

(3) the mouse head was simulated in two scenarios:
   a) with homogeneous optical properties and
   b) with different optical properties for *brain*, *other tissue* and *air*.

Furthermore, different levels of background fluorescence were evaluated. To do so, the sum over all voxels excluding the fluorescent inclusion weighted by a factor of 0 (no background influence), 10^{-9}, 10^{-8}, 10^{-7} or 10^{-6} was added to the time of flight distribution of the fluorescent voxel. This corresponds to 0%, 0.03%, 0.3%, 3%, and 30% of the target's concentration, respectively. The resulting distribution was convolved with the time of flight distribution of the excitation wavelength (Figure 3.6(b)).

For all finite media simulated, a linear calibration line was plotted between two potential calibration points, one above and one beneath the object. Additionally, a grey shaded area enveloping all data points was added to illustrate the deviation from such a potential calibration.

3.3 Results

3.3.1 Simulation Results for Increasingly Realistic Geometries

The results of the Monte Carlo simulations for increasingly realistic geometries are shown in Figure 3.5 and Figure 3.6. In all homogeneous media, a linear relationship is observed between the mean time of flight of the fluorescence photons $\langle t \rangle_{fl}$ and the depth of the fluorescent object. In the case of the semi-infinite medium (Figure 3.5(a)), this linearity could be extended to more than 20 mm depth(N=10^{11}, blue). When considerably fewer photons (N=10^8, green) are simulated and the SNR in

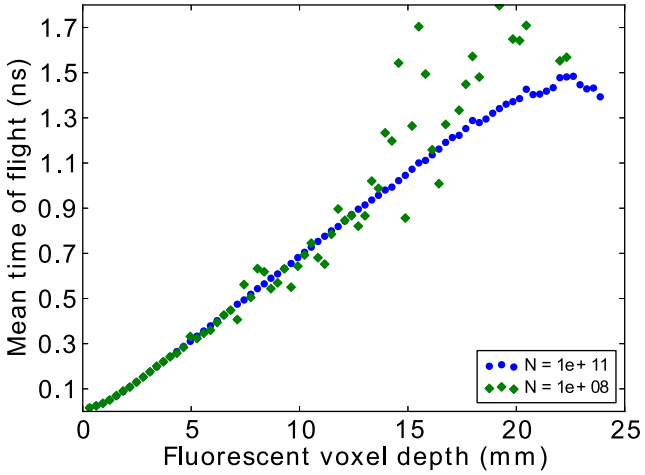

(a) semi-infinite medium

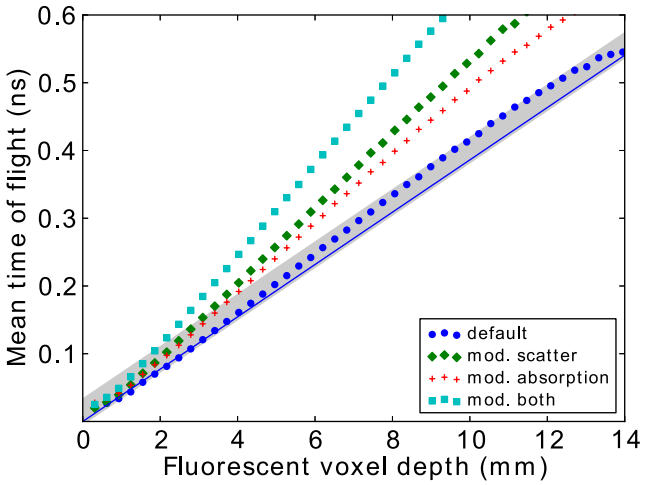

(b) cylindrical medium

Figure 3.5: *MC results without background fluorescence for the semi-infinite and the cylindrical geometry. (a): Mean time of flight for a fluorescent source in different depths with sufficient (blue) and reduced (green) signal-to-noise ratio in deeper layers. (b): Mean time of flight for a fluorescent source in different depths with the tabulated optical properties of other tissue (blue), increased scattering (green), reduced absorption (red), or the variation of both (cyan). The solid blue line displays a potential calibration line between two points, one above and one beneath the object, together with a grey shaded area enveloping all data points to illustrate the deviation from such calibration.*

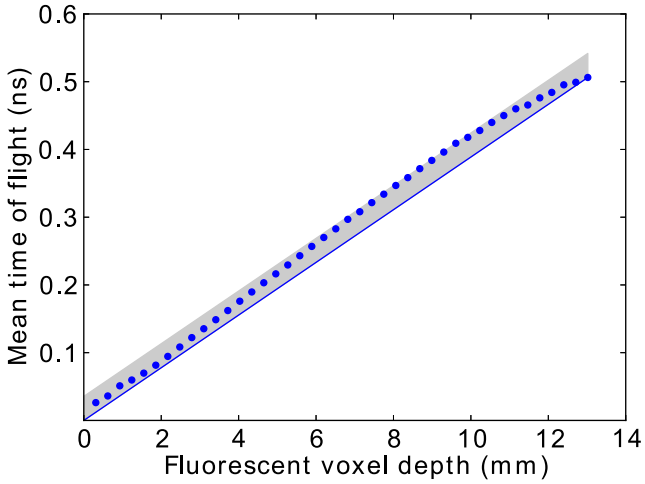

(a) homogeneous mouse head

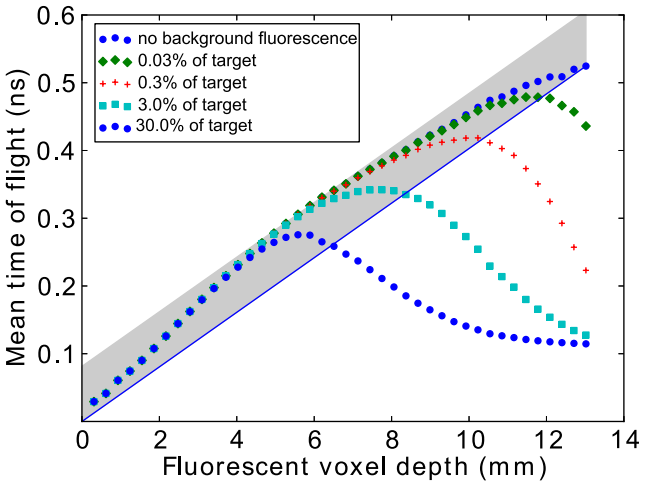

(b) heterogeneous mouse head

Figure 3.6: *MC results for the homogeneous and the heterogeneous mouse head geometry with increasing levels of background fluorescence. (a): Mean time of flight for a fluorescent source in different depths in a mouse head geometry with homogeneous optical properties. (b): Mean time of flight for a fluorescent source in different depths in a mouse head geo-metry with heterogeneous optical properties and increasing levels of homogeneous background fluorescence. The solid blue lines display a potential calibration line between two points, one above and one beneath the object, without unspecific background fluorescence or prior to fluorophore injection, respectively.*

	λ (nm)	μ_a (mm^{-1})	μ_s (mm^{-1})	g	n
Brain	682	0.023	19.9	0.9	1.4
	710	0.017	18.6	0.9	1.4
Other Tissue	682	0.0421	12.9	0.9	1.4
	710	0.029	12.0	0.9	1.4
Air	682, 710	0.0	0.0	1.0	1.0

Table 3.1: *Optical properties used in the Monte Carlo simulations. Data are taken from in vivo measurements published by [Bourayou et al., 2008].*

deeper layers decreases, noise dominates over the linear trend already at about 15 mm depth.

The results for a finite, cylindrical medium with homogeneous but varying optical properties (Figure 3.5(b)) illustrate how the linear slope between $\langle t \rangle_{fl}$ and depth increases with higher scattering or lower absorption in the tissue. Here, a decrease in μ_a from 0.029 mm^{-1} to 0.017 mm^{-1} or an increase in μ_s from 12 mm^{-1} to 18 mm^{-1} both lead to an increase in slope of about 33% (from about 0.0375 ns/mm to about 0.05 ns/mm). Varying μ_s and μ_a simultaneously increases the slope of the linear correlation to about 0.0625 ns/mm.

3.3.2 Simulation Results for Heterogeneous Media and Different Levels of Background Fluorescence

In the more realistic case of a heterogeneous mouse head (Figure 3.6(b)), the slope between $\langle t \rangle_{fl}$ and inclusion depth can no longer be considered as *constant* throughout the medium. Without unspecific background fluorescence, it changes at a depth of 6 mm from about 0.05 ns/mm to about 0.033 ns/mm for any deeper inclusion sights. This change in slope can be explained by the change in μ_s from *brain* to *other tissue* at 6 mm depth. The overall convex increase in $\langle t \rangle_{fl}$ with depth leads to a larger deviation from a linear calibration ($\approx$ 0.0385 ns/mm) which is indicated by the increased width of the grey shaded area. Calibrating by two measurement points, above and below the mouse head, would overestimate the actual depth of an inclusion by up to 2 mm. For increasing levels of homogeneous background fluorescence the correlation between mean time of flight and depth of a fluorescence source deviates from the linear trend derived without background after 12, 10, 8, and 6 mm of depth, respectively. As the initial linear slope stays constant no matter whether background fluorescence is present or not, a potential calibration prior to fluorophore injection still maintains validity for target depths up to several mm. Calibrating with unspecific background fluorescence in the

media, however, would drastically underestimate the initial slope thereby giving falsely overestimated values for the inclusion depth.

3.4 Discussion

With the development of targeted probes and agents the interest in fluorescence imaging is now in the fluorophore biodistribution in tissues [Massoud and Gambhir, 2003, Ntziachristos, 2006, Hilderbrand and Weissleder, 2010, Ntziachristos, 2010]. While cw intensity measurements are most widely used because they use rather simple and inexpensive instrumentation, they require tomographic measurements combined with complex inversion algorithms (see Chapter 4) to decouple fluorophore depth and concentration [Ntziachristos, 2006, Tan et al., 2013]. Time-domain diffuse optical measurements can recover both from a single source and detector measurement [Hall et al., 2004, Keren et al., 2008].

Here, the limitations of the linear dependence between mean time of flight $\langle t \rangle_{fl}$ and depth of a fluorescent inclusion for planar imaging have been explored. Ranging depth by measuring $\langle t \rangle_{fl}$ is only possible as long as a sufficient SNR can be measured. The higher the sensitivity of the camera system used, the longer the distance over which the linear correlation with depth holds true in homogeneous media. If the SNR is low for a deep laying source, the measured mean time of flight cannot be determined reliably. In the case of small animal imaging with object dimensions of a few cm, however, it is possible to adequately measure a second calibration point below the object. Therefore, it is feasible to linearly approximate the correlation between $\langle t \rangle_{fl}$ and inclusion depth throughout a small animal.

The simulation results for the mouse head geometry show that the potential error in depth using the proposed linear calibration critically depends on changes of the optical properties within the medium. As expected, the slope between $\langle t \rangle_{fl}$ and depth increases with increasing scattering or lower absorption properties of the medium. Changes in μ_s and μ_a between different types of tissue result in a bend of the linear trend. Nevertheless, in the simulations without background fluorescence, the depth of a fluorescent inclusion in the heterogeneous mouse head gets overestimated by a linear calibration by 2 mm at most. Therefore, depth ranging of a focal target with this approach still seems reasonably feasible in *non*-fluorescent biological tissue.

In *in vivo* fluorescence imaging, background fluorescence resulting from unbound compound circulating in the vasculature or tissue autofluorescence are often not negligible and can become a major obstacle [Hilderbrand and Weissleder, 2010, Gu et al., 2013]. Our simulation results suggest that the initial linear slope between $\langle t \rangle_{fl}$ and depth is not affected by the presence of background fluorescence. A potential calibration *prior* to fluorophore injection, or for instance with a control

animal, would therefore still hold valid up to several mm of target depth. For rodents, the question often arises in planar cw imaging as to whether a measured fluorescent distribution originates from a focal source in a deeper layer, as for example in an ischemic region in the mouse brain, or from a broader source of lower concentration in a superficial layer, as for example the highly vascularized scalp [Piper et al., 2010]. This question can still be answered with the simple depth-ranging approach. Differentiating between intra- and extracerebral signal is not hampered when using a linear calibration, even in the presence of moderate background fluorescence.

3.4.1 Limitations of the Suggested Depth Ranging Approach

The suggested calibration approach is not suitable for large object dimensions, as for instance the human head, because it is not possible to adequately measure a second calibration point below the object. In functional brain imaging in humans, additional dynamic changes in the mean time of arrival have shown to help in differentiating intra- and extracerebral space [Liebert et al., 2006, Jelzow et al., 2012].

As no *in vivo* measurements have been performed so far, the success of the inferred calibration approach has to be taken conditionally. A potential calibration with unspecific background fluorescence already present in the media would drastically underestimate the initial slope, thereby giving falsely overestimated values for the inclusion depth. Though not investigated here, also in the case of multiple, closely neighbouring targets, the method is likely to fail if the fluorescence signals overlap in the acquired planar fluorescence image. It remains to be determined whether the approach is inferior in terms of depth resolution to existing time-domain fluorescence *tomography* [Lam et al., 2005, Ale et al., 2013, Tichauer et al., 2013] and fluorescence lifetime imaging systems, which haven proven capable of deconvolving probe from background signals [Akers et al., 2007, Kumar, 2011, Rice et al., 2013].

3.5 Conclusion

The simulation results have shown that the well-known linear relationship between mean time of flight and depth of a fluorescent object in planar time-resolved fluorescence imaging also holds in heterogeneous, finite turbid media as is the case in rodents. More importantly, even in the presence of strong unspecific background fluorescence, a potential calibration with two measurement points, one above and one below the object, prior to fluorophore injection still holds valid up to several mm of target depth.

While depth estimation with the suggested calibration approach still has to be reproduced and validated in *in vivo* measurements, it benefits from its simplicity and straightforward applicability to real measurements, avoiding additional measurement channels or complex image reconstruction. Especially for the case of small animal imaging this simple approach could garner sufficient information about the depth of a fluorescent target.

4 Tomographic Approach Resolving Depth with Multi-Distance Measurements

4.1 Introduction

In this chapter the concept of optical tomography is introduced which makes use of multiple source and detector sites to yield a three-dimensional image reconstruction.

This known approach was applied within a clinical pilot study on contrast-enhanced fast dynamic 3D optical mammography in humans. Different kinetic features, three-dimensionally resolved throughout the entire breast volume, could be derived and evaluated for their potential to distinguish malignant (cancerous) from benign (non-cancerous) breast tissue. Parts of this chapter were published in RöFo - Fortschritte auf dem Gebiet der Röntgenstrahlen und der bildgebenden Verfahren [Schneider et al., 2011].

4.1.1 Medical Need: Optical Mammography

Breast cancer is the leading malignancy of women worldwide [Jemal et al., 2008]. Approximately one in eight women in western countries will be diagnosed with breast cancer in her lifetime, with increasing incidence of breast cancer worldwide [DeSantis et al., 2011]. Nodal involvement as well as the presence of distant metastases closely correlates with the size of the primary tumor [Carter et al., 1989, Van Lancker et al., 1995]. Therefore, prognosis of women with breast cancer is better the earlier the cancer is detected [Clark et al., 1987, Carter et al., 1989]. Currently, the gold standard for breast cancer screening is X-ray mammography. Its frequency of employment, however, is limited due to the use of ionizing radiation. Furthermore, it causes discomfort in patients, has shown to be less reliable for young women with dense breast tissue, and has fairly low average sensitivity and specificity of about 75 % and a 60-90 %, respectively [Pisano et al., 2005]. Moreover, there is a high false positive rate leading to unnecessary psychological strain [Leff et al., 2008]. After 10 mammograms one in two women will have had at least one false positive [Elmore et al., 2005]. For monitor-

ing women at high-risk of developing breast cancer, magnetic resonance imaging (MRI) has proven to be a powerful alternative to X-ray mammography, but high costs and variable specificity hinders its use as a general screening modality prophylactically applied to all women [DeSantis et al., 2011]. Ultrasound imaging, as the third clinically available breast imaging method, is often required as an additional diagnostic tool to differentiate suspicious masses detected by palpation or X-ray mammography. However, ultrasound imaging is very examiner-dependent and time-consuming with low specificity which makes it unsuitable as a screening tool [Tromberg et al., 2008, DeSantis et al., 2011, Flexman et al., 2011, Poellinger, 2012].

The limitations of all currently available breast imaging modalities have fuelled the search for alternative techniques. Historically, breast illumination with NIR light started more than 80 years ago [Cutler, 1929], but NIR spectroscopy has only become feasible with developments in light sources, detectors, and computing technology since the 1980's. It allows the calculation of scattering and absorption properties in tissue from light intensity changes [Delpy et al., 1988, Sassaroli and Fantini, 2004, Kocsis et al., 2006] and, moreover, the derivation of hemoglobin concentration and oxygen levels [Jobsis, 1977, Carlsen, 1982, Bartrum Jr and Crow, 1984]. In the 1990's, concepts for a three-dimensional image reconstruction evolved despite dominant scattering of photons in tissue [Graber et al., 1993, Arridge and Hebden, 1997, Arridge and Schweiger, 1997]. Different from ionizing radiation, which is only minimally scattered and therefore basically propagating on a direct, straight path though tissue, the diffuse propagation of NIR light allows only probabilistic predications about its travelled path [Gibson et al., 2005]. While it is common sense in the optical research community that diffuse optical imaging can never compete in terms of spatial resolution with anatomical imaging techniques such as X-ray imaging, ultrasound or MRI, it offers several distinct advantages in terms of sensitivity to physiological changes in tissue, safety, cost and bedside use rather than anatomical mapping [Gibson et al., 2005, Leff et al., 2008, Weissleder and Pittet, 2008]. Moreover, recent developments towards fast diffuse optical tomography (DOT) [Barbour et al., 2001, Schmitz et al., 2005], with volume scan rates of more than 1 Hz, now allow sufficient sampling of hemodynamic changes in tissue, thereby raising the hope to characterize tissue beyond static, morphological imaging contrast [Flexman et al., 2011, Schneider et al., 2011, Schreiter et al., 2013].

Tumor growth is closely connected with an increased vascularization (neoangiogenesis) for keeping up a sufficient blood supply [Weinberg, 2007]. Furthermore, vasculature in tumorous tissue tends to be disorganized, hyperpermeable, and lacking proper vasomotor function [Jain, 2001, Weinberg, 2007, Weissleder and Pittet, 2008]. These functional changes in diseased compared to healthy tissue result in

measurable changes in scattering and absorption properties due to the underlying differences in blood volume and tissue oxygenation. They open the floor for several unique contrast mechanisms assessable with NIR imaging [Tromberg et al., 2008]. Dynamic features that have been investigated include tissue-intrinsic dynamics such as the resting auto regulatory rhythms or breathing maneuvers [Flexman et al., 2011, Schmitz et al., 2013, Flexman et al., 2013, Schreiter et al., 2013] as well as those evoked by external contrast mechanism such as the application of tissue pressure [Al Abdi et al., 2010, Carp et al., 2013], the use of non-air breathing gases [Graber and Barbour, 2012] or use of blood-borne contrast agents to increase the diagnostic yield of optical mammography [Corlu et al., 2007, Alacam et al., 2008, Poellinger et al., 2011b, Poellinger et al., 2011a, Ebert and Grosenick, 2013].

We performed a clinical pilot study on fast 3D optical mammography using extrinsic dynamic contrast. Here, bolus kinetics after rapid administration of the blood-pool agent indocyanine green (ICG) were imaged [Schneider et al., 2011]. Depending on concentration, ICG can cause an approx. hundredfold increase in NIRS light absorption and has a high binding affinity to serum proteins that cannot pass through the endothelium of healthy vessels [Landsman et al., 1976, Yoneya et al., 1998, Desmettre et al., 2000]. During early enhancement, tissue concentration contrast is mainly determined by intravascular contributions [Alacam et al., 2008, Hagen et al., 2009]. Previously reported absorption measurements were able to study some aspects of ICG pharmacokinetics in the breast [Intes et al., 2003, Alacam et al., 2008], however, none of these have been performed at scan rates that adequately sample the early bolus dynamics in tissue. In the following sections a reader-independent analysis approach will be derived to automatically differentiate malignant from benign lesions based on non-invasively acquired early ICG bolus kinetics. This numerical approach focuses on dynamic, perfusion-related parameters and their distribution within the entire breast volume without demanding any a priori information on the localization of lesions.

4.1.2 Introduction to Diffuse Optical Tomography (DOT)

4.1.2.1 General Introduction

Diffuse optical tomography generates full three-dimensional (3D) images of optical properties within the transilluminated tissue. To do so, sequential measurements are taken from an array of light sources and detectors widely spaced over the tissue's surface and generally coupled to by means of fiber-optic components as described in detail by [Arridge and Hebden, 1997, Arridge and Schweiger, 1997, Hebden et al., 1997, Boas et al., 2001, Gibson et al., 2005, Arridge and Schotland, 2009]. Figure 4.1A illustrates the probability distribution of photon travel in tissue

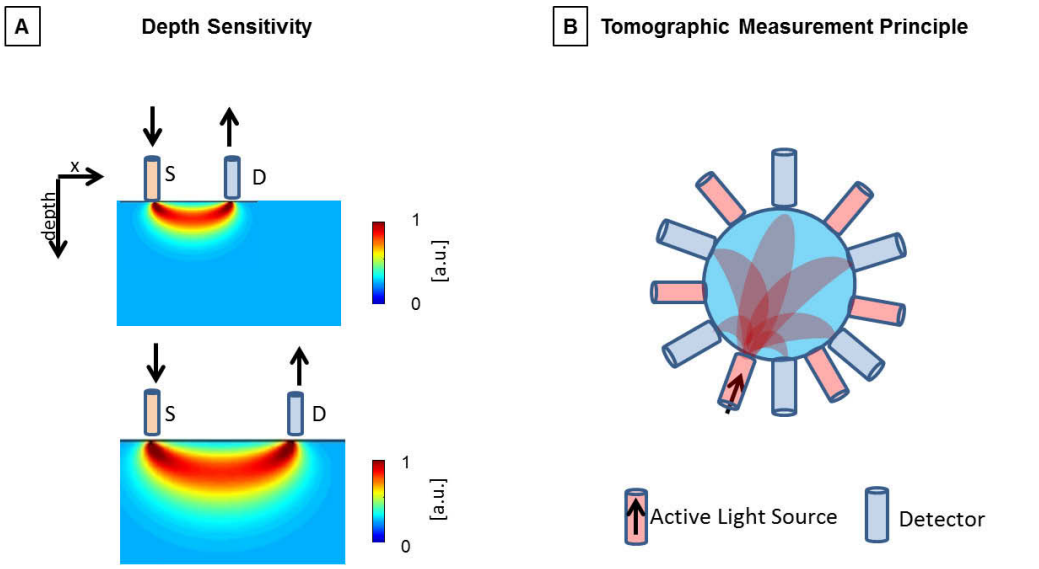

Figure 4.1: *Depth sensitivity and measurement principle in optical tomography. A: The sensitivity distribution for a single source-detector measurement depends on the distance between source and detector. The color coded vertical slices show how the probability of photon travel through deeper layers increases with increasing source-detector distance. Source (S) and detector (D) are separated by 1 cm and 2 cm, respectively. B: Tomographic measurements consist of sequential tissue illumination and multiple source-detector distances. The scheme illustrates an annular optode arrangement typically applied in breast imaging and sketches the overlapping sensitivity areas between a single source and multiple detectors.*

for photons emitted at point S and captured at the location of the detector D. Though NIR light is propagating diffusive (randomly) through the entire tissue volume after 1-2 mm from the source [Jacques and Pogue, 2008], the fraction of light reaching a certain detector has most likely probed the 'banana' shaped part of the volume between the particular source and detector. Therefore, each source - detector combination, a so-called optical channel, is sensitive only to a certain area in between.

Moreover, depending on the distance between source and detector, different depths are probed [Barbour et al., 2001,Boas et al., 2004]. The larger the distance, the more likely a detected photon has travelled deeper through tissue. Figure 4.1B schematically shows the overlapping sensitivity area for multiple source-detector combinations surrounding the tissue of interest.

4.1.2.2 Image Reconstruction

The Optical Reconstruction Process in General

Optical image reconstruction is an elaborate process matching theoretical predictions of photon propagation through tissue to the actual measurements on the surface. This involves

(i) modelling of the expected DOT measurements for a given measurement setup with assumed tissue optical properties (often termed *forward model*),

(ii) inversion of the predicted solution, and

(iii) reducing the mismatch between the model-based predictions and the actually acquired measurements,

thereby recovering the most likely distribution of parameters of interest out of the data based on the model.

Mathmatical Formulation of the Reconstruction Process

Mathematically, the calculation of one or more internal characteristics from a series of boundary measurements is an example of a so-called *inverse problem*. In [Arridge and Hebden, 1997], the *forward model* is stated as follows:

"Given a distribution of light sources $\{q\}$ on the boundary $\delta\Omega$ of an object Ω, and a distribution of tissue parameters $\{p(\vec{r})\}$ within Ω, find the resulting measurement set $\{y\}$ on $\delta\Omega$."

This can be expressed with the help of a general non-linear forward operator F:

$$y = F[p(\vec{r})]. \tag{4.1}$$

Similarly, the inverse problem is stated as:

"Given a distribution of light sources $\{q\}$ and a distribution of measurements $\{y\}$ on $\delta\Omega$ derive the tissue parameter distribution $\{p(\vec{r})\}$ within Ω."

which can be represented by

$$\{p(\vec{r})\} = F^{-1}[\{y\}]. \tag{4.2}$$

What might look simple to solve turns out to be a mathematical and computational challenge because usually the problem is highly ill-posed.

Non-linear image reconstruction

If absolute values of the optical properties are to be reconstructed from a single acquisition, as might be the case in breast imaging [Dehghani et al., 2003] or in static imaging of the brain [Hintz et al., 2001, Hebden et al., 2002], the full non-linear problem has to be solved.

To do so, a regularized objective function Ψ is defined, which represents the difference between the measured data y and the predicted data based on an assumed forward model $f(p)$, for example in a least-squared sense:

$$\Psi = \|y - f(p)\|^2 + \alpha\|\Pi\|^2, \tag{4.3}$$

where $\|\cdot\|^2$ is the L2-norm, α is the regularization parameter, and Π might be as simple as the identity matrix, $\mathbf{I}$, or include some anatomical and other prior information to constrain the number of possible solutions. A weighted least squares solution reducing the influence of noise and cross-talk both in the image and in the data can be obtained when the covariance of the image C_Q and the covariance of the data C_P are included:

$$\Psi = (y - f(p))^T C_P (y - f(p)) + \alpha(\Pi^T C_Q \Pi). \tag{4.4}$$

The non-linear minimization problems in Equation (4.3) and (4.4) are generally solved either by a Newton method such as the Levenberg-Marqardt algorithm [Moré, 1978, Marquardt, 1963], or by a gradient method such as conjugate gradients [Arridge, 1999].

The distribution of optical parameters $f(\hat{p})$ which minimizes Ψ, is then taken to be the image.

Linearization of the Forward Model

The majority of DOT reports use a perturbation approach to linearize the forward operator F for an easier study of the inverse problem. This can be done if the inverse problem is assumed to be that of reconstructing the difference between two similar states, for instance two measurements taken before and after a small (physiological) change in the optical properties. The actual optical properties p and the measured data y are assumed to be close to an initial estimate $\hat{p}$ and the simulated measurements $\hat{y} = F[\hat{p}]$, respectively. Equation (4.1) is then approximated by its Taylor series

$$y = \hat{y} + F'[\hat{p}](p - \hat{p}) + O(p^2) \tag{4.5}$$

while neglecting any terms higher than the first (linear) term. F' is the first-order Fréchet derivative of F. Both are mapping functions from the image space $\{p\}$ to the data space $\{y\}$ [Arridge and Hebden, 1997]. Numerically, F' can be

expressed in a matrix representation, termed the Jacobian matrix **J**. Putting $\Delta p = p - \hat{p}$ and $\Delta y = y - \hat{y}$ equation (4.1) can further be written in the so-called Born approximation as:

$$\Delta y = \mathbf{J}[\hat{p}]\Delta p. \tag{4.6}$$

Physically, the first Born approximation treats each point in an inhomogeneity as if it existed in isolation from the rest, ignoring the contributions of perturbations of the scattered field from other parts of an inhomogeneity [Gaudette et al., 2000].

Linearizing the change Δy in log intensity instead is called the Rytov approximation and may improve the reconstructed images by reducing the dynamic range of y [Gibson et al., 2005]. Either way, not absolute values but changes in tissue optical properties are reconstructed. Furthermore, using relative detector values $\Delta y/y_0$, usually relative to a baseline y_0 at rest or before a certain maneuver or task, has proven advantageous for dynamic measurements as well as fast image reconstruction [Pei, 1999, Pei et al., 2001, Pei et al., 2003].

The perturbation approach reduces the inverse problem to an inversion of the Jacobian matrix **J**, or some form of normalized **J**, at $\hat{p}$ [Arridge and Hebden, 1997]. The remaining challenge of the *inverse problem* is described below.

The Forward Model

Since NIR light propagation becomes diffusive (isotropic) after about 1 mm in tissue, calculation of the Jacobian is usually solved by solving the diffusion approximation to the radiative transfer equation (RTE) [Gibson et al., 2005]. For continuous-wave light sources, the time-independent form is applied [Kaltenbach and Kaschke, 1993], which is given by [Pei et al., 2001]:

$$-\delta(\vec{r} - \vec{r}_s) = \nabla[D(\vec{r})\nabla\Phi(\vec{r})] - \mu_a(\vec{r})\Phi(\vec{r}), \quad \vec{r} \in \Omega, \tag{4.7}$$

for a domain Ω with boundary $\delta\Omega$. Here, $\Phi(\vec{r})$ is the measured photon fluence at position $\vec{r}$, $\vec{r}_s$ the position of a cw light source, $\mu_a(\vec{r})$ is the position-dependent absorption coefficient and $D(\vec{r})$ the corresponding diffusion coefficient:

$$D(\vec{r}) = 1/[3(\mu_a(\vec{r}) + \mu_s'(\vec{r})]. \tag{4.8}$$

The reduced scattering coefficient, μ_s', can be calculated from the scattering coefficient μ_s and the tissue scattering anisotropy g by:

$$\mu_s' = \mu_s(1 - g) \tag{4.9}$$

This correction to μ_s results in a longer effective scattering mean free path if scattering of tissue is biased forward [Jacques and Pogue, 2008]. In biological

tissue, g is approximately 0.9. A photon can thus be considered isotropically scattered after 10 scattering events.

Practical modelling schemes to calculate **J** derived from the RTE or the diffusion approximation to the RTE, respectively, proceed either stochastically or deterministically [Arridge and Hebden, 1997]. The first employ Monte Carlo methods or random walk theory, for example. The latter are using analytical methods like the application of Green functions or finite-element schemes [Arridge and Schotland, 2009]. Regarding complex geometries and boundary effects for arbitrarily shaped objects, the finite-element method has proven most versatile [Arridge et al., 1993, Arridge, 1999] and effective with regard to computational costs [Arridge and Schweiger, 1995, Schweiger et al., 1995, Arridge et al., 2000]. Here, the volume is discretized to a finite element mesh of irregular objects with assigned optical properties taking into account that computational efficiency requires a finite element mesh which adequately represents the internal field while using the smallest possible number of elements [Gibson et al., 2005].

The derived Jacobian, also referred to as the *weight* or *sensitivity* matrix, therefore becomes an $M \times N$ matrix with entries J_{ij} that physically represent the fractional change in light intensity measured by the i^{th} source-detector pair at the surface caused by an incremental change in the optical properties at the j^{th} pixel or finite element in the medium [Pei et al., 2001].

The Inverse Problem

Most commonly, the linear equation system (4.6) is under-determined and **J** ill-posed. The first, because the affordable number of source-detector pairs, M, is commonly sparse compared to the number N of unknown optical properties $\mu_a(\lambda)$ and $D(\mu_a(\lambda), \mu_s'(\lambda))$. The second, because the absorption coefficients do not vary smoothly with the data. Therefore, the matrix **J** is not invertible, which constitutes to the term inverse *problem*. Nevertheless, there are several matrix inversion techniques for calculating a *pseudo* inverse. They vary in the way the inversion is regularized to suppress the influence of measurement noise and modelling errors [Habermehl et al., 2014] and may work iteratively to find the most likely solution to the measured data [Gaudette et al., 2000, Gibson et al., 2005]. In the following, three common methods applied in DOT image reconstruction will be briefly introduced.

- **Tikhonov Regularization** is one of the oldest and most established regularization methods [Calvetti et al., 2000]. In its simplest form, the system

of linear equations is replaced by the regularized system

$$\left(\mathbf{J}^T\mathbf{J} + \alpha\mathbf{I}\right)\Delta p = \mathbf{J}^T\Delta y \quad \text{for} \quad \alpha \geq 0, \tag{4.10}$$

where α is a regularization parameter that determines the amount of regularization and $\mathbf{I}$ is the identity matrix. For any $\alpha > 0$ Equation (4.10) has the unique solution

$$\Delta p_\alpha = \left(\mathbf{J}^T\mathbf{J} + \alpha\mathbf{I}\right)^{-1}\mathbf{J}^T\Delta y. \tag{4.11}$$

The goal is then to find the solution $\Delta\tilde{p}_\alpha$ of Equation (4.10) that satisfies the minimization problem

$$min_{\alpha\in\mathbf{R}_+}\left\{\|\mathbf{J}\Delta p - \Delta y\|^2 + \alpha\|\Delta p\|^2\right\} \tag{4.12}$$

where $\|\cdot\|$ denotes the Euclidean norm.

- **ART - the Algebraic Reconstruction Technique** solves Equation (4.6) by sequentially projecting an estimate of the solution onto the hyperplanes defined by the individual rows of the linear system. This projection then estimates the solution in the next iterative step. Mathematically, this can be written as [Gaudette et al., 2000]

$$\Delta p_{k+1} = \Delta p_k + \omega\frac{\Delta y_i - \mathbf{j}_i\Delta p_k}{\mathbf{j}_i\mathbf{j}_i^T}\mathbf{j}_i^T \quad k = 0, 1, \ldots \quad i = kmodM + 1 \tag{4.13}$$

  where Δp_k corresponds to the k^{th} estimate of the solution, $\mathbf{j}_i$ corresponds to the i^{th} row of the $M \times N$ matrix $\mathbf{J}$, and Δy_i is the i^{th} measurement. The relaxation parameter ω customizes the step size of each iteration.

  ART converges for under-determined systems to a point on the hyperplane satisfying the linear system which is nearest to the initial guess [Kak and Slaney, 1988]. Limiting the number of iterations regularizes the convergence, though the optimum choice of how many iterations to perform is difficult [Van der Sluis and Van der Vorst, 1990].

- **TSVD - Truncated Singular Value Decomposition** is a subspace technique derived from the singular value decomposition (SVD) of the $M \times N$ stacked system matrix $\mathbf{J}$ given by [Gaudette et al., 2000]:

$$\tilde{\mathbf{J}} = \mathbf{U}\Sigma\mathbf{V}^T, \quad \mathbf{U} \in R^{M\times M} \quad \mathbf{\Sigma} \in R^{M\times N} \quad \mathbf{V} \in R^{N\times N}. \tag{4.14}$$

$\mathbf{U}$ and $\mathbf{V}$ are orthonormal matrices and $\mathbf{\Sigma}$ is a diagonal matrix with rank r whose entries $\Sigma_{i,i} = \sigma_i$ are the singular values of $\mathbf{J}$ with

$$\sigma_1 > \sigma_2 > \cdots > \sigma_r \quad and \quad \sigma_{r'} = 0 \quad \text{for all} \quad r < r' < min(M, N) \tag{4.15}$$

Discretized ill-posed problems result in poorly conditioned matrices with a very wide spectrum of singular values, over several orders of magnitude. The TSVD algorithm uses only the largest t non-zero singular values and singular vectors to estimate the inverse of Equation (4.6) by

$$\Delta\tilde{p}_t = \mathbf{V}_t \Sigma_t^{-1} \mathbf{U}_t^T \Delta y, \tag{4.16}$$

where $\mathbf{V}_t$ and $\mathbf{U}_t$ are the first t columns of $\mathbf{V}$ and $\mathbf{U}$, respectively, and Σ_t is the square diagonal submatrix of the largest t singular values. The truncation parameter, t, defines the amount of regularization in the inverse and controls the trade-off between fidelity to the data and some constraint on the result.

There are many methods available how to choose the regularizations parameter, but an appropriate *a priori* choice in general does not exists. For subspace techniques such as the TSVD, the *a posteriori* L-curve technique [Hansen, 1998, Hansen, 1999] has proven useful, which defines a curve $\mathcal{L}$

$$\mathcal{L} = \{(\mathcal{F}(\|\mathbf{J}\Delta\tilde{p}_t - \Delta y\|^2), \mathcal{F}(\|\Delta\tilde{p}_t\|^2)); \quad \text{for} \quad t > 0\}, \tag{4.17}$$

by a monotonically increasing function $\mathcal{F}$ of the L2-norm of the residual versus $\mathcal{F}$ of the L2-norm of the regularized solution $\Delta\tilde{p}_t$ while varying the regularization parameter t.

The resulting graph is termed the L-curve, because it is shaped roughly like the letter L. A small choice of t leads to a huge norm of the associated solution $\|\Delta\tilde{p}_t\|^2$, which is likely to be contaminated by the propagated error originating from the measurement noise in Δy. Conversely, a stronger regularization reduces the norm of the solution but increases the norm of the associated discrepancy $\|\mathbf{J}\Delta\tilde{p}_t - \Delta y\|^2$. The regularization parameter is then chosen at the *vertex* of the L seeking to balance between the discrepancy and the propagated error in the computed solution due to errors in Δy [Calvetti et al., 2000].

Dynamic DOT Imaging

For dynamic DOT imaging, the reconstruction process is usually performed separately for each acquired time frame. Normally, the same forward model can be used for each frame. Therefore, the Jacobian needs to be inverted only once. A

fast implementation that allows for real-time image recovery has been proposed by [Pei et al., 2003] using TSVD to solve the inverse problem.

4.1.2.3 Calculation of Physiological Parameters

Assuming that oxyhemoglobin (HbO) and deoxyhemoglobin (HbR) are the only chromophores in tissue significantly contributing to NIR light absorption, then the change in absorption $\Delta\mu_{a^{\lambda_i}}$ is given by the sum of concentration changes of Δ [HbO] and Δ [HbR] multiplied by their corresponding extinction coefficients $\epsilon^{\lambda_i}_{\mathrm{HbO}}$ and $\epsilon^{\lambda_i}_{\mathrm{HbR}}$ at wavelength λ_i [Choi et al., 2004]:

$$\Delta\mu_{a^{\lambda_i}} = \epsilon^{\lambda_i}_{\mathrm{HbO}}\Delta[\mathrm{HbO}] + \epsilon^{\lambda_i}_{\mathrm{HbR}}\Delta[\mathrm{HbR}] \tag{4.18}$$

Using two wavelengths, concentration changes of both hemoglobin states can be calculated:

$$\begin{pmatrix} \Delta[\mathrm{HbO}] \\ \Delta[\mathrm{HbR}] \end{pmatrix} = \begin{pmatrix} \epsilon^{\lambda_1}_{\mathrm{HbO}} & \epsilon^{\lambda_1}_{\mathrm{HbR}} \\ \epsilon^{\lambda_2}_{\mathrm{HbO}} & \epsilon^{\lambda_2}_{\mathrm{HbR}} \end{pmatrix}^{-1} \begin{pmatrix} \Delta\mu_{a^{\lambda_1}} \\ \Delta\mu_{a^{\lambda_2}} \end{pmatrix} \tag{4.19}$$

From these, other physiologically important parameters can be obtained, for instance

- changes in total hemoglobin concentration:
  Δ[Hbt]=Δ[HbR] + Δ[HbO],or
- oxygenation saturation:
  Δ HbS = Δ [HbO] / Δ [Hbt] $\cdot$ 100% .

The contribution to the optical NIR signal measured is mainly from capillaries, venules, and arterioles, because NIR light is less likely to escape from vessels with diameter larger than 0.2 mm [Firbank et al., 1997].

The use of a blood-borne contrast agent (CA) adds to the changes in NIR light absorption by ϵ_{CA} Δ[CA] according to the additional chromophore's concentration Δ[CA] and extinction coefficient ϵ_{CA}. An additional wavelength is required to resolve concentrations changes of all three circulating chromophores. However, in the case of the contrast agent ICG, the contributions of hemoglobin changes are often neglected because $\epsilon^{\lambda_i}_{\mathrm{ICG}} >> \epsilon^{\lambda_i}_{\mathrm{HbO/HbR}}$.

4.2 Methods

4.2.1 Dynamic Contrast-Enhanced Optical Mammography Study

In cooperation with the Institute of Radiology, Charité University Medicine Berlin, a prospective patient study was conducted to evaluate fast 3D near-infrared breast imaging using extrinsic dynamic contrast for the detection and characterization of breast lesions [Schneider et al., 2011].

Patients

A total of 25 optical mammography data sets were obtained from 22 women (mean age of 53 years, range 27 - 78 years) who had a suspicious finding in one of their breasts detected by X-ray mammography or ultrasound. Subsequent needle biopsy or surgical excision demonstrated a malignant breast lesion in 14 cases (median patient age 60 years) and a benign lesion in 8 cases (median patient age 32 years). In addition, there was a control group of three breasts without any lesions (as verified by MRI and 1.5 years follow-up): two contralateral breasts of two patients of the benign group and one contralateral breast of the malignant group. Before biopsy all patients underwent ultrasound, 21 patients received X-ray mammography and 20 patients obtained dynamic contrast-enhanced magnetic resonance imaging (DCE-MRI) at 1.5T (Signa Twin-Speed, General Electric Medical Systems, Milwaukee) with Gadolinium bolus injection. The exclusion criteria were age under 18 years, breast size greater than 34B (US system), needle biopsy or surgery of the ipsilateral breast within the previous 6 months, ulcers or wounds of the ipsilateral breast, and known anaphylactic reactions to ICG.

NIR DOT Breast Imaging System

Diffuse optical imaging was performed using a DYNOT 232 tomography system (NIRx Medical Technologies LLC, NY, USA) customized for unilateral mammography studies (Figure 4.2). A detailed description of the DOT system itself is given in [Schmitz et al., 2005]. Briefly, it is a continuous-wave system that performs simultaneous dual-wavelength measurements at 760 nm and 830 nm. It features 31 optical fibers bundles (optodes) mounted in four concentric rings around a rigid, hemispheric plastic cup with a diameter of 10 cm (Figure 4.2B). Each optode contains fibers that emit light from the optical light source as well as fibers that collected light reemitted from tissue. The instrument performs sequential illumination at each fiber position while simultaneously acquiring detector readings from all sites, resulting in a total of 961 measurement channels per wavelengths that are sampled at a rate of approx. 2 Hz.

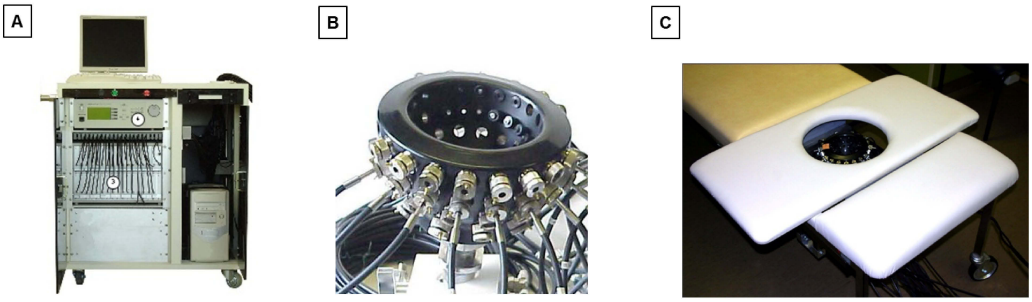

Figure 4.2: *Dynamic near infrared optical tomography system customized for unilateral mammography studies. A: DYNOT 232 tomography system (NIRx Medical Technologies LLC, NY, USA).B: Breast interface for 31 adjustable optodes arranged in four concentric rings. C: Modified patient bed.*

Different breast sizes were accommodated by varying the protrusion of the fibers into the cup. The fiber holder was mounted on a gantry positioned under a modified patient bed. The gantry slides sideways to be used on either breast and can be height-adjusted to bring the cup up against the patient's chest wall through an opening in the bed (Figure 4.2C). Women remained in prone position throughout the examination.

Imaging Protocol

Optical scanning was performed continuously for a total period of approx. 25 min and comprised the following steps:

i. 5 min baseline scan, during which the patient was requested to lie still and breathe normally,

ii. bolus administration of 25 mg ICG (PULSION Medical Systems AG, Munich, Germany) diluted in 15 ml aqua *ad injectionem* (injection time: 5 s) followed by a 15 ml saline flush,

iii. 20 min of scanning during which the patient is requested to lie still and breathe normally.

Data Preprocessing

The acquired raw data sets were preprocessed and reconstructed using the corresponding software package NAVI (NIRx Medical Technologies, LLC. (NY, USA)) [Pei et al., 2006]. First, data were smoothed with a low-pass filter of 0.15 Hz to minimize motion artifacts and high-frequency noise. Then, mean value (MV) and

standard deviation (STD) over the baseline time interval were computed for each data channel. Any channel for which the resulting coefficient of variation (CV = 100% · STD/MV) was larger than 15%, in either wavelength, was excluded from subsequent data-processing steps. Third, differences among the various channels' sensitivity settings were corrected for by dividing each time series by its baseline MV, which produced a dimensionless quantity with mean value of unity over the baseline time interval. Fourth, variations in laser output power were corrected for by computing the frame-by-frame ratio of the filtered channel data and the corresponding laser reference-channel time series. In most experiments, less than 5% of data channels were from consideration because of excessive noise.

Tomographic Reconstruction

Preprocessed data were then automatically reconstructed by the NAVI software as temporally and three-dimensionally resolved absorption changes relative to baseline.

In detail, image time series were reconstructed using relative detector differences to generate a linear perturbation equation [Barbour et al., 2001], which was subsequently solved by using a truncated singular value decomposition (TSVD) algorithm [Pei et al., 2003]. The TSVD approximates the ill-conditioned matrix $\mathbf{J}$ with the matrix $\mathbf{J}_t$ of rank t according to Equation (4.14)

$$\mathbf{J}_t = \sum_{i=1}^{t} \mathbf{u}_i \sigma_i \mathbf{v}_i \quad \sigma_i > \tau_{threshold} \tag{4.20}$$

and leads to the approximated solution:

$$\Delta p \simeq \Delta p_t = \sum_{i=1}^{t} \frac{\mathbf{u}_i \Delta y}{\sigma_i} \mathbf{v}_i \quad \text{for} \quad \sigma_i > \tau_{threshold}. \tag{4.21}$$

The threshold $\tau_{threshold}$ can be individually adjusted in the NAVI software and was chosen to account for 98% of the variance of the data.

The Jacobian matrix was generated by a finite element method algorithm that numerically solved the diffusion equation on a homogeneous hemispherical forward model with a diameter of 10 cm. The applied finite element mesh (FEM) contained 2243 nodes and 8790 tetrahedral elements with background mean values of absorption $\mu_a(\text{BMV}) = 0.06$ cm^{-1} and scattering $\mu_s(\text{BMV}) = 10$ cm^{-1}.

At each FEM node and for every time frame values of

$$\frac{\Delta\mu_a(t)}{\mu_a(t_0)} = \frac{\mu_a(t) - \mu_a(\text{BMV})}{\mu_a(t_0)} \tag{4.22}$$

were computed relative to baseline measurements $\mu_a(t_0)$. The time series of relative absorption after ICG bolus injection were calculated based on the 760 nm measurements only, since absorption properties of ICG over different ICG concentrations in plasma are rather constant at 760 nm as opposed to 830 nm [Landsman et al., 1976].

For display and data export, FEM grid data were then interpolated to 14,000 isometric volume cubes (voxels) with an edge length of 2.5 mm.

4.2.2 Evaluated Dynamic Parameters

For further evaluation and display, the reconstructed voxel time courses were analyzed using customized routines in Matlab (The Mathworks, Inc., Natick, USA).

All time courses were additionally filtered with a 0.07 Hz low-pass Butterworth filter to suppress heartbeat, higher-frequency noise, and motion artefacts. To account for a large inter-subject variability in overall signal intensity, all datasets were normalized to the maximum of the spatial mean time course of each patient. Its time point, t_{max}, was used to calculate the signal-to-noise ratio (SNR) for every voxel as the ratio of signal intensity at t_{max} and the standard deviation over the baseline period. Voxels for which SNR$<$1 were excluded from further analysis and mapping.

Regions of interest (ROIs) were manually selected in the approximated location of the lesion corresponding to palpation and MRI or X-ray mammography. For the healthy control breasts, control ROI tissue was symmetrically selected to the corresponding lesion bearing breast.

To evaluate differences in contrast dynamics for various breast lesions, three perfusion related parameters were calculated in each voxel:

- peak amplitude (PA),
- time-to-peak (TTP), and
- 'peak time grouped amplitude' (PTA).

PA was defined as the maximum amplitude in absorption changes following ICG bolus injection. To account for variations in overall signal intensities due to different breast sizes and tissue density, PA was calculated in percent with the mean amplitude within the entire breast volume of each patient being 100%. TTP is the corresponding time point of peak absorption change after ICG injection. To overcome inter-subject variability in overall blood flow, the reference time point $t_0 = 0\ s$ was set to the earliest time point of bolus arrival in the breast,which was defined as the point in time when more than 0.25% of the breast volume has exhibited a peak in intensity. Determination of these two perfusion related parameters

proved particularly robust across all voxels of the entire breast volume. Color-coded TTP and PA maps were derived and displayed in three oblique planes of the breast –coronal, sagittal and transversal– similar to the acquired DCE-MRI image planes for visual (reader-dependent) diagnosis.

The third parameter, 'peak time grouped amplitude', was then calculated as mean peak amplitude within the breast volume as a function of TTP:

$$\mathrm{PTA(TTP)} = \frac{1}{n} \sum_{n} \mathrm{PA}_n(\mathrm{TTP}) \tag{4.23}$$

PTA corresponds to the mean peak amplitude over all n voxels simultaneously exhibiting their maximum amplitude at time TTP. To evaluate the first bolus passage of ICG throughout the breast TTP values between 0 and 12 seconds in 0.5 s steps were considered.

4.2.3 Reader-Independent Lesion Classification

Based on the average PTA(TTP)-curves over all benign and malignant cases, a reader-independent metric was derived that distinguishes malignant from benign breast data without requiring any a priori information on the spatial localization of the lesion.

In detail, the standardized mean difference (SMD) between both PTA data groups was computed for each considered TTP value. SMD is defined as the difference of the means for two different groups divided by their pooled standard deviation:

$$SMD = \frac{\bar{X}_{mal} - \bar{X}_{ben}}{\sqrt{\frac{1}{n_1+n_2-2}\left((n_1-1)\cdot var(X_{mal}) + (n_2-1)\cdot var(X_{ben})\right)}} \tag{4.24}$$

with $\bar{X}_{mal}$ and $\bar{X}_{ben}$ being the group means, var the variance, and n_1, n_2 the total number of datasets in the malignant and benign group, respectively.
The most distinguishable point in time, t_{cutoff}, between both groups is given by the maximum SMD. The non-parametric Mann-Whitney-U test was applied to test whether the distributions of PTA values at TTP=t_{cutoff} come from distributions with equal median. A p-value of $p < 0.05$ was considered significant to reject the null hypothesis of equal medians.

From the PTA distributions at t_{cutoff}, a decision boundary PTA_{db} was derived to classify malignant and benign breasts data. Due to the small number of datasets in each group ($n_1 = 14$, $n_2 = 8$), we refrained from multivariate approaches, e.g. a linear discrimination analysis, which assumes the classes to be normally dis-

			Histology (Gold Standard)		
			proofed malignant	proofed benign	Total
Dynamic Optical	**Mammography**	Classified as malignant PTA > decision boundary	A *true positive*	B *false positiv*	A+B
		Classified as benign PTA < decision boundary	C *false negatives*	D *true negatives*	C+D
		Total	A+C	B+D	

Table 4.1: *Definition and derivation of sensitivity = $A/(A+C)$, specificity = $D/(B+D)$, positive predictive value = $A/(A+B)$, and negative predictive value = $D/(C+D)$ of a diagnostic method.*

tributed with different means but identical covariance matrix with full rank [Duda et al., 2012], or even nonlinear classification algorithms, e.g. Support Vector Machines [Muller et al., 2001]. Alternative features for multivariate classification approaches in a larger clinical trail will be briefly outlined in the discussion. On our PTA-feature, we performed a receiver operator characteristics (ROC) analysis [Zweig and Campbell, 1993, Cardillo, 2008].

In an ROC analysis, the classifier's output is calculated for all possible decision thresholds and plotted as the 'true positives'-rate (sensitivity) versus either the 'false positives'-rate (1 - specificity), or, for medical data more common, the 'true negatives'-rate (specificity). Either way, the area under the derived ROC-curve (AUC) is a measure of separation of two univariate distributions. Applied to the output of a two-class classifier, AUC is a bias-independent performance measure. The ROC graphs are commonly used in medical decision making and have proven useful for visualizing a classifier's performance. For random values in each class the AUC value would be around 0.5; if classes can be perfectly separated, the AUC value is 1. From an ROC-curve, the decision boundary for best sensitivity and specificity can be derived. Sensitivity, specificity as well as positive predictive value (ppv) and negative predictive value (npv) over all malignant and benign datasets were calculated for this decision boundary as defined and illustrated in Table 4.1. Data of the control group were not included in the ROC analysis.

4.2.4 Lesion Localization

The true location of a breast lesion was determined by palpation and Gadolinium-enhancement in DCE-MRI. If information of both modalities was available, priority was given to palpation. Palpation was performed directly after NIR imaging and was spatially related to the position of the imaging fibers.

To judge the accuracy of localising lesions with dynamic optical mammography, coronal maps of PA-, TTP- and PTA(t_{cutoff})-values were evaluated individually, thereby neglecting the sagittal and transversal plane, which underlie relevant fluctuations by breast compression and placement. Spots of high PA, early TTP, or above PTA_{db} in the optical mammograms were categorized as location correct if estimated and observed location of the lesion enclosed an angle of less than 90 degrees.

4.3 Results

The histological findings and lesion dimensions are summarized in Table 4.2. Of the 22 optical mammography data sets of breasts bearing a suspicious lesion, histology revealed nine invasive ductal carcinomas (IDC), one invasive lobular carcinoma (ILC), two metaplastic carcinomas, one ductal carcinoma in situ (DCIS) and one invasive lobular ductal carcinoma (ILDC) constituting to the malignant group. The benign group consisted of 6 fibroadenomas (FA), 1 fibrocystic changes (FC), 1 pseudoangiomatous stroma hyperplasia (PASH).

4.3.1 Mapping Dynamic Features

Figure 4.3 shows magnetic resonance images as well as dynamic optical mammography maps for three representative cases. Moreover, the corresponding mean time courses of relative absorption changes after ICG bolus injection over the approximated location of the lesion and healthy residual breast tissue are shown.

For the malignant example, the DCE-MRI images show a large area of hypervascularization at the 9 o'clock position in the coronal view. This corresponds well with a single, focal region of higher amplitudes in the peak amplitude map and earliest peak times in the time-to-peak map of ICG-enhanced optical mammography. The histology revealed a 33 mm intermediate grade IDC.

Figure 4.3 (on the opposite side): *Dynamic optical mammography results for a malignant case (33 mm intermediate grade invasive ductal carcinoma (IDC) in a 53-year-old woman), a benign case (22 mm fibroadenoma in a 27-year-old woman) and a healthy control (29-year-old woman). A,C,D: acquired DCE-MRI images and color-coded maps of*

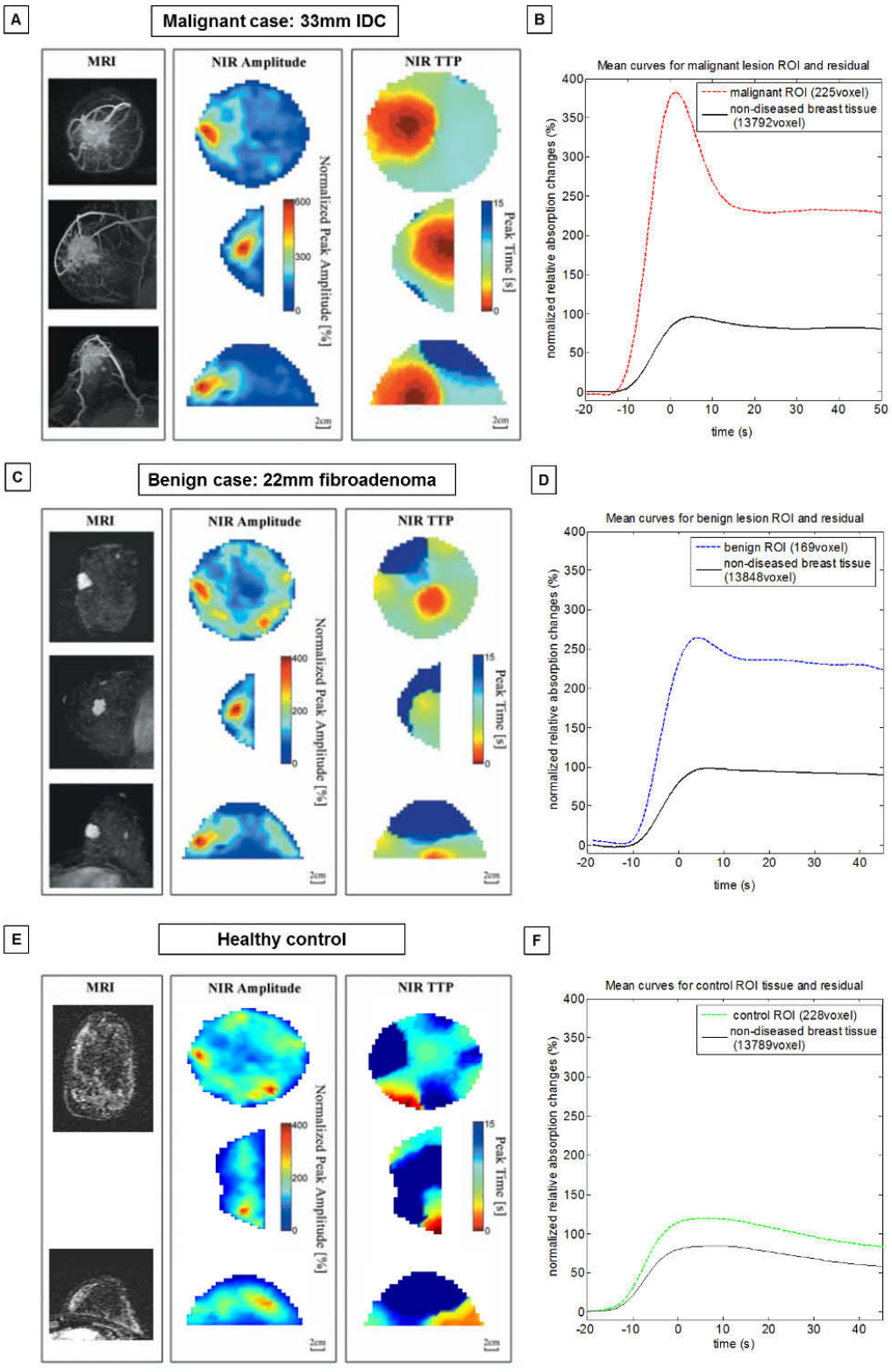
A
Malignant case: 33mm IDC
MRI
NIR Amplitude
NIR TTP
Normalized Peak Amplitude [%]
Peak Time [s]
B
Mean curves for malignant lesion ROI and residual
malignant ROI (225voxel)
non-diseased breast tissue (13792voxel)
normalized relative absorption changes (%)
time (s)
C
Benign case: 22mm fibroadenoma
D
Mean curves for benign lesion ROI and residual
benign ROI (169voxel)
non-diseased breast tissue (13848voxel)
E
Healthy control
F
Mean curves for control ROI tissue and residual
control ROI (228voxel)
non-diseased breast tissue (13789voxel)

Figure 4.3

peak amplitude and time to peak (TTP) displayed in three oblique planes of the breast - from top to bottom: coronal, sagittal and transversal view. B,D,F: Normalized relative absorption changes over time in different regions of the breast after ICG bolus injection. Regions of interest (ROIs) were manually selected in the approximated location of the lesion corresponding to palpation and MRI. For the healthy breast, control ROI tissue was symmetrically selected to the corresponding lesion bearing breast.

In the second example, DCE-MRI shows a suspicious lesion located at 9 o'clock (coronal view). The corresponding area in the optical mammography maps features focally high PA and moderate TTP values. The histology revealed a 22 mm fibroadenoma, a non-cancerous lesion. An additional hot spot of high peak amplitude is visible in the PA map at about 5 o'clock (coronal view), potentially coming from a large superficial vein. The TTP map shows a spot of earliest peak times in the lower right quadrant of the coronal plane and close to the chest wall in the transversal view with corresponding low peak amplitudes.

These two examples illustrate perfusion differences between malignant and benign and/or healthy tissue. The malignant lesion shows a predominant initial peak during first bolus passage of ICG compared to the (surrounding) healthy tissue.

The healthy control in Figure 4.3 has an unsuspicious DCE-MRI result as judged by an experienced radiologist. ICG-enhanced optical mammography, however, shows two hot spots of high peak amplitude in the PA map at about 9 and 5 o'clock position (coronal view), respectively, with corresponding very long peak times. The TTP map shows a spot of earliest peak times at about 7 o'clock in the coronal plane with corresponding moderate peak amplitudes. The control ROI time course does not differ substantially from the average over the entire breast.

4.3.2 Results: Lesion Localization

When evaluating the PA maps, isolated spots of high PA values were found in the correct location for 11 of the 14 malignant lesions (78.6%) and for 5 of the 8 benign lesions (62.5%). Evaluation of the TTP maps revealed focal areas of short TTP values for all of the malignant lesions and 7 of the benign lesions(87.5%) in the correct location. However, additional local maxima possibly perceivable by a reader as 'lesion' were found in 64% of all malignant cases when evaluating PA maps only and in 33.3% in the pure TTP map evaluation. Both methods additionally showed lesion-like spots in 37.5% of the benign cases.

4.3.3 Results: Reader-Independent Lesion Classification

Derivation of PTA curves as a function of TTP is illustrated in Figure 4.4. In the benign case (right), peak amplitudes increase with increasing TTP within the first 10 seconds, while in the malignant case (left) peak amplitudes are highest for the shortest peak times and start decreasing for a TTP of more than 2 seconds.

This difference in temporal behaviour between the two single cases has shown to be consistent over all subjects. Figure 4.5 shows the mean PTA curves over all benign and malignant cases together with the standard error of mean. Breasts with a benign lesion show a gradual PTA increase with increasing TTP whereas for

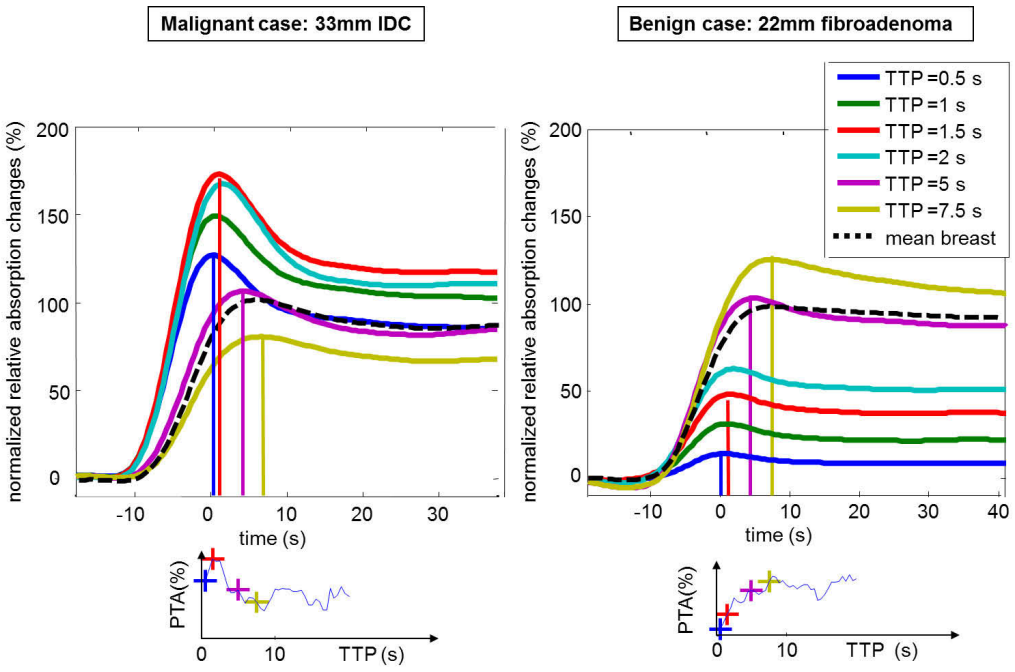

Figure 4.4: *Derivation of peak time grouped amplitude (PTA) curves as a function of time to peak (TTP). Top: Normalized mean time courses over all volume segments with equal TTP for the malignant and benign example case, respectively. Reference time point (t=0) was set to the appearance of first bolus peaks in the breast. All data are normalized to the maximum of the respective mean time course (dashed black line). Bottom: derived PTA(TTP) curves for both examples given by the mean peak amplitude as a function of TTP.*

malignant cases, PTA is highest for the shortest peak times and starts decreasing for TTP $>$ 2 s. After 5 seconds a rather constant plateau can be discerned for the malignant group while for the benign group a further increase in amplitude can be observed up to 12.5 seconds.

The best discriminatory power between malignant and benign data is expected when the standardized mean difference is at maximum. In our study, maximum SMD was observed for t_{cutoff}=1.5 s (SMD = 1.76). Mean PTA values of both groups differ significantly at this point (p = 0.0015).

The results of the ROC analysis are presented in Figure 4.5. The decision boundary PTA_{db} = 84.4% yields the highest sensitivity (85.7%) and specificity (87.5%) for the data used, with an AUC (± S.E.) of 0.92 (± 0.06). All classification results

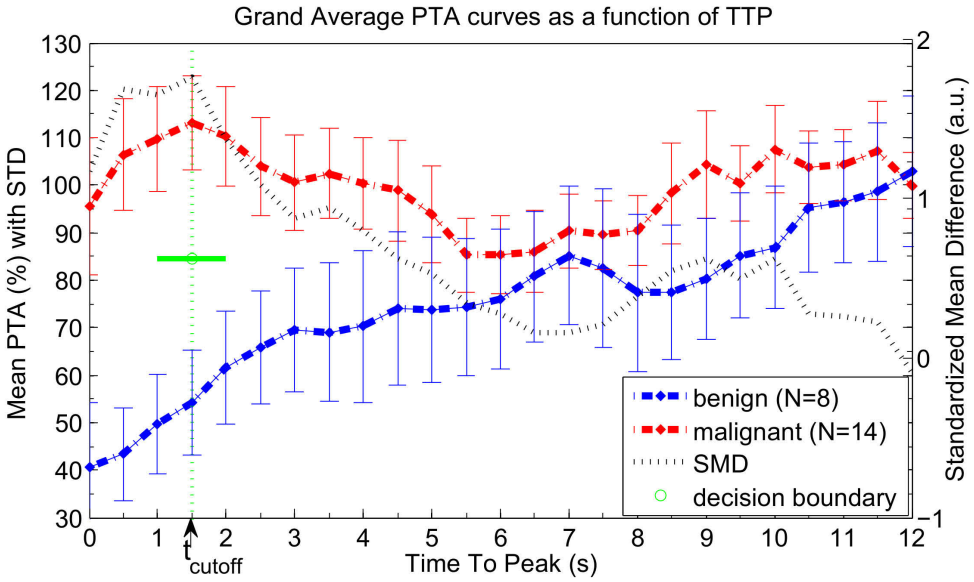

Figure 4.5: *Derivation of a reader-independent classification metric based on a peak time grouped amplitude (PTA) analysis for 22 patients. A: Mean PTA curves as a function of TTP with standard error of mean for of all benign (blue) and all malignant (red) data sets. The standardized mean difference (SMD) for each time point is indicated by the black dotted line; the arrow marks the time point of maximum SMD at* t_{cutoff} *= 1.5 s. The determined decision boundary* PTA_{db}*= 84.4% is indicated as a green bar.*

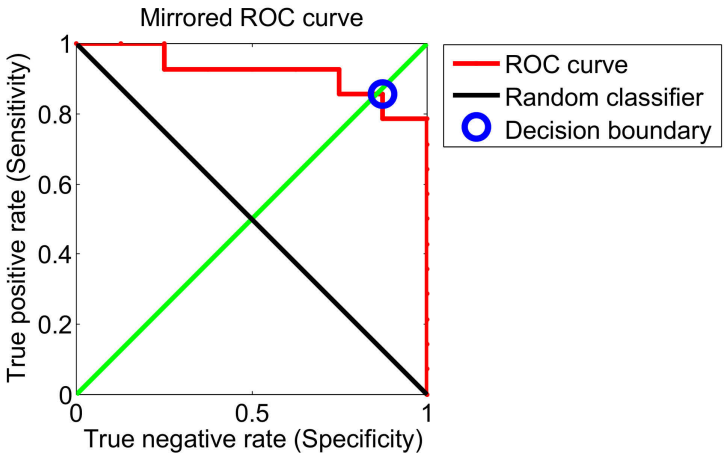

Figure 4.6: *ROC analysis results for PTA values at t_{cutoff}. The blue circle marks the point of highest sensitivity and specificity within the analyzed data set.*

Histopathology	**Number of lesions**	**Mean lesion size** (range)	**Classified correctly**
malignant (n = 14)	14		12/14
invasive ductal carcinoma	9	29 mm (8 - 51 mm)	8/9
invasive lobular carcinoma	1	25 mm	1/1
invasive lobular ductal carcinoma	1	17 mm	0/1
metaplastic carcinoma	2	28 mm (19 - 37 mm)	2/2
ductal carcinoma in situ	1	80 mm	1/1
benign (n = 8)	8		7/8
fibroadenoma	6	24 mm (10 - 52 mm)	5/6
mastopathy	1	11 mm	1/1
PASH	1	44 mm	1/1
healthy (n = 3)	0		3/3

Table 4.2: *Histopathological findings and classification results.*

for the derived boundary decision are summarized in Table 4.2. The two malignant cases that showed lower PTA(t_{cutoff}) values than 84.4% were a moderately graded IDC with a diameter of 15 mm in a 55-year-old patient (PTA(t_{cutoff}) = 30.4%) and a mixed invasive lobular and ductal carcinoma (diameter: 16 mm) in a 61-year-old patient (PTA(t_{cutoff})=74.7%). In the benign group there was only one case of a 10 mm FA in a 50-year-old woman with an amplitude of 99.6% leading to a false positive result. Positive predicted value and negative predicted value add up to 92.3% and 77.8%, respectively. The three healthy control breasts that were not included in the ROC analysis were also correctly classified as 'not malignant' (mean PTA(t_{cutoff}) = 32.7%, min 22.5%, max 60.4%) using the derived PTA_{db} decision boundary.

Regarding lesion localization within a PTA(t_{cutoff}) map, 12 of 14 malignant lesions (85.7%) were detected and mapped at correct location. In 4 malignant breasts (28.6%) additional spots were observed and 1 benign lesion was falsely detected as malignant at correct location without showing any allocatable additional spots. The remaining 7 benign lesions (87.5%) were accurately not detected.

4.4 Discussion

Using contrast-enhanced dynamic optical mammography, significant differences in the enhancement kinetics of benign and malignant breast lesions were found. High frame rate tomographic reconstruction of relative absorption changes after ICG bolus injection depicted early maximum values with higher peak amplitudes compared to the spatial average over the entire breast only in breasts bearing a malignant lesion. The localization of malignant lesions based on combined high PA and early TTP values was in good agreement with MRI and palpation in 12 of 14 cases. When parameter maps were individually evaluated by a reader similar to X-ray mammograms, relatively high rates of additional (false positive) spots where observed ranging from 28.6% of all malignant cases in the PTA analysis to 64% when mapping PA only. The combination of the perfusion-related parameters TTP and PA, however, allowed the derivation of a reader-independent amplitude cut-off that distinguished malignant from non-malignant data with high accuracy (sensitivity = 85.7%, specificity = 87.5%, ppv = 92.3%, npv = 77.8%).

Due to the use of non-ionizing near-infrared light optical tomography has a clear advantage over X-ray mammography not only in terms of safety, costs and bedside use, but also in terms of sensitivity to functional changes in tissue [Gibson et al., 2005, Leff et al., 2008, Weissleder and Pittet, 2008]. The drawback of using low-energy radiation comes with a relatively low spatial resolution due to the diffusive nature of light propagation in tissue [Gibson et al., 2005]. Optical tomography

cannot overcome this issue, but can push its limits down to about 1-3 cm depending on the inter-optode distance applied and tissue depth [Boas and Dale, 2005, White and Culver, 2010, Eggebrecht et al., 2012, Habermehl et al., 2012]. The use of co-located source-detector fibers in our study allowed a dense optode arrangement and good spatial coverage of the entire breast with inter-optode distances from 2.5 cm to 10 cm. The effective spatial resolution can therefore be approximated to about 2.5 cm according to the shortest inter-optode distance applied in the grid [White and Culver, 2010]. The voxel width of 2.5 mm in the reconstructed NIR images (Figure 4.3) is artificially derived and mainly for illustration purpose.

Improvements in localization and characterization of tissue properties can either be achieved by additional source-detector pairs, thereby decreasing the underdetermination of the inverse problem [White and Culver, 2010], or by incorporating soft or hard priors derived from concurrent imaging modalities in the forward modelling [Pogue and Paulsen, 1998, Brooksby et al., 2003, Boas and Dale, 2005, Boverman et al., 2005] as well as spatial constraints in the inverse problem [Intes et al., 2004, Yalavarthy et al., 2007]. In our study, corregistration with MRI was not possible, but DOT and MRI measurements were both performed with the patient lying in prone position. This allowed for visual comparison along similar imaging planes of both modalities. Besides the fact that at the present state-of-the-art concurrent (or corregistered) imaging is elaborate to implement, the above mentioned methods on incorporating patient based individual priors also require high computational effort. Both are counterproductive when seeking optical mammography as a screening modality.

In this context, not spatial resolution is most important in optical breast imaging, but the non-invasive derivation of functional information that cannot be easily accessed with standard X-ray imaging, ultrasound or MRI [Tromberg et al., 2008, Poellinger, 2012, Flexman et al., 2013]. While high frame-rate optical breast imaging after ICG bolus injection has not been investigated before, our findings are in good agreement with Alacam et al. who investigated ICG pharmacokinetics at a sampling rate of approx. 0.1 Hz and observed delayed enhancement in a fibroadenoma in comparison to malignancies [Alacam et al., 2008].

The rapid, early signal increase in breasts with malignant lesions is likely due to higher vessel density found in malignancies [Papadimitriou and Woods, 1975, Weidner et al., 1991, Tsutsui et al., 2003] as compared to non-malignant tissue. It is well known from dynamic MRI that malignancies tend to show faster flooding [Boetes et al., 1994, Dietzel et al., 2011] and earlier wash-out rates [Schnall et al., 2006]. In contrast to gadolinium-based contrast agents that exhibit fast and unspecific extravasation through capillaries, ICG binds to macromolecules [Landsman et al., 1976, Yoneya et al., 1998, Desmettre et al., 2000], and acts like a macromolecular contrast agent. During early enhancement, tissue concentration contrast is de-

termined by intravascular contributions [Alacam et al., 2008, Hagen et al., 2009], while extravasation of bound ICG is a much slower process unlikely to significantly add to the measured absorption change during the first bolus passage.

In a future clinical trail the simultaneous acquisition of the arterial input function (AIF) of the bolus injection would be of great interest. Modelling the microvasculature as a linear, time-invariant system relative values of blood flow, blood volume, capillary transit time and vascular leakage can be derived [Elliott et al., 2012, St Lawrence et al., 2013]. This has been tried with an average AIF model and a unified dye-dilution DOT reconstruction technique [Elliott et al., 2012, Piper et al., 2014a]. One of the challenges with the optical datasets acquired in our study is the lack of anatomical priors to significantly improve the posedness of the inverse problem. To overcome this limitation, we employed a simplified two-region spatial model –whereby the tumor is considered a sphere of variable size– and optimized the centroid position of the tumor, as well as the kinetic parameters of tumor and background [Piper et al., 2014a]. The kinetic analysis suggested the presence of a lesion with greater relative blood flow, increased permeability and larger capillary heterogeneity (i.e., greater capillary transit time) – all of which are indicative of increased angiogenesis associated with cancer [Østergaard et al., 2013].

Because tumorous tissue often features increased capillary permeability, late ICG enhancement due to extravasation also becomes a promising contrast characteristic [Piper et al., 2013a]. When doing without the optical image reconstruction and simply taking the mean signal amplitude over all measurement channels for different time windows malignant and benign breast data showed a significant difference in the late washout phase 300 - 325 sec after bolus onset. In this time window a leave-one-out cross-validation with a linear discriminant analysis showed an average test loss of 6.8% corresponding to a sensitivity and specificity of 87.5% and 90.9% respectively [Piper et al., 2013a].

Besides imaging enhanced absorption by ICG, its fluorescence has also proven attractive for breast cancer detection since tissue auto-fluorescence is low in the NIR spectral range and (late) fluorescence signals mainly originate from cancerous tissue [Corlu et al., 2007, Hagen et al., 2009, Poellinger et al., 2011a]. Combined high frame-rate absorption and fluorescence measurements after ICG bolus injection would therefore be of great interest for future research.

In our image reconstruction breast tissue was assumed to have homogeneous optical background properties. This is only a simplified approximation of the breast which is actually heterogeneous and highly structured. It mainly consists of glandular and adipose regions whose size and optical properties change at different points in the menstrual cycle and as a woman ages and glandular tissue atrophies [Cerussi et al., 2001, Shah et al., 2001]. There was a substantial median

age difference between the malignant and benign group, not considered in the analysis. Differences in breast perfusion could possibly be caused by age-related differences in glandular density (involution) and tissue perfusion. In a larger clinical trial attention should be paid to age-matched cohorts.

The average sensitivity and specificity reported for X-ray mammography are about 75% and 60-90%, respectively [Pisano et al., 2005]. The results achieved with our non-invasive approach showed an even higher sensitivity and good specificity compared to those for X-ray mammography. Nevertheless, a cross-validation is required to generalize the results to unseen subjects. A larger clinical trial needs to be conducted to determine a reliable overall sensitivity and specificity for the presented ICG-enhanced optical mammography classification.

It is well known from other imaging modalities, such as MRI, that substantial overlap can exist in contrast enhancement properties for fibroadenoma (benign lesions) and invasive breast cancers [Kuhl et al., 2008]. Furthermore, benign lesions, or simply dense glandular tissue may also be associated with a higher content of hemoglobin [Floery et al., 2005, Rinneberg et al., 2005, Leff et al., 2008, Schreiter et al., 2013]. Due to these possible overlaps of malignant and benign tissue properties, it has not been possible to differentiate breast lesions based on intrinsic parameters alone, so far [Leff et al., 2008].

Within our sparse number of datasets, a complete separation of malignant and benign data due to the derived early ICG-enhancement feature has not been possible either. We had one false positive and two false negatives, which imply that there is a physiological overlap in early ICG-perfusion between malignant and benign breast lesions. For larger clinical trials multivariate analysis tools should be considered [Duda et al., 2012] able to handle multiple features, such as different time points of ICG-enhancement or kinetic parameters such as blood flow, blood volume and capillary transit time. Moreover, careful corregistration with MRI data would permit the spatial labelling of each reconstructed voxel. This would allow to train a classifier on the individual voxels, thereby preserving the depth resolution for lesion localization in unseen (test) data.

Nevertheless, the presented classification approach focuses on differences in early perfusion dynamics throughout the breast without requiring any a priori information about the existence and localization of lesions which drastically eases the measurement and computational efforts.

4.5 Conclusion

In conclusion, the results show that early perfusion analysis of ICG-enhanced fast 3D optical mammography can help to non-invasively detect malignant breast

lesions in the depth of tissue and moreover distinguish between malignant and benign breast tissue. It is important to note that differentiation can be achieved without subjective evaluation by a trained reader. This readies the approach as a promising tool to improve the prognosis of women with breast cancer by contributing to an improved early and accurate identification of breast cancer adjunct to the established X-ray mammography screening.

5 Conclusions and Outlook

Despite optical imaging's unique advantages and capabilities, its application in non-invasive *in vivo* imaging has been hampered by low depth sensitivity due to the diffusive nature of light propagation in tissue.

In this thesis, three different approaches have been presented and tested to overcome this drawback. While planar resolution can be obtained using sensitive CCD-cameras, depth resolution of a fluorescent object or focal region of high absorbance can either be obtained with (i) multi-spectral imaging, (ii) by time-gated detection which relates photon flight time to object depth, or (iii) with elaborate tomographic measurements and image reconstruction.

With the development of numerous highly specific reporter agents, non-invasive near-infrared fluorescence imaging has become a key technique to study pathophysiology in animal disease models. While the trend is toward whole-body small animal optical tomography systems, their required complexity in imaging hardware and image reconstruction often discourages staff in biomedical research laboratories. The novel surface-stripping algorithm (i) presented herein [Piper et al., 2010], however, enhances image contrast and detectability of fluorochromes located several mm deep in tissue, even in a relatively undemanding *planar* imaging setup.

The usability of this multi-spectral approach was demonstrated in the context of small animal stroke research, a highly relevant field aiming to improve prevention, treatment and diagnosis of stroke. Nevertheless, this technique is not restricted to cerebral target sites in small animal imaging, but could also be helpful in humans, where dynamic fluorescence imaging has been used for the diagnosis of rheumatoid hands [Werner et al., 2012], diabetic feet [Perry et al., 2012] or sentinel lymph nodes [Rasmussen et al., 2009]. Recently our group presented the first whole-body fluorescence imaging system suitable for adult subjects and demonstrated sensitivity to circumscribed alterations in skin perfusion [Piper et al., 2013b].

In a next step, spectral excitation may increase diagnostic sensitivity and specificity of this novel and promising tool and establish 'surface-stripped' imaging of the whole body or larger body parts for systemic pathologies, including lymphatic disorders, skin cancer, peripheral vascular disease, polyneuropathy or arthritis.

For planar fluorescence imaging in small animals, the proposed time-domain

calibration (ii) has shown promising simulation results. The results suggest that even in the presence of strong non-specific background fluorescence garnering sufficient depth information of a fluorescent target is feasible. In a next step, *in vivo* reproduction of the effect is required as well as the comparison to existing time-domain fluorescence tomography systems [Ale et al., 2013, Tichauer et al., 2013]. Hereby not only the accuracy of depth ranging but also the computational costs and hardware efforts have to be considered. We expect benefits from the simplicity and straightforward applicability of the calibration approach.

Over the last decade, diffuse optical tomography (DOT) has emerged as a novel, non-invasive biomedical imaging modality (iii), that may be able to address some of the shortcomings of other imaging techniques. Particularly, dynamic DOT has been considered as an alternative or an adjunct to X-ray mammography for identifying and monitoring breast tumors [Tromberg et al., 2008, Leff et al., 2008, Flexman et al., 2013].

The results presented here show that early perfusion analysis of ICG-enhanced fast 3D optical mammography can help to non-invasively detect malignant breast lesions in the depth of tissue and moreover distinguish *automatically* between malignant and benign breast tissue. It is important to note that a computer-aided diagnosis without subjective evaluation by a trained reader matches well with the goal of providing a non-invasive screening tool prophylactically applied to all women. Future developments aim for a dual-breast imaging system allowing for the contra-lateral breast to serve as a reference that is under the same external stimulus as the tumor-bearing breast. Discrimination features between malignant and benign breast tissue are expected to have a higher discriminatory power when derived from relative intra-subjects differences as compared to inter-subject comparisons [Al Abdi et al., 2010, Flexman et al., 2013, Schreiter et al., 2013]. To accomplish these imaging goals, it is essential to have a system that can acquire a large amount of data at fast imaging speeds. Moreover, a more compact design would enable a critical milestone of usage outside the laboratory environment, for example as a screening tool in the gynecologist's office. Recently, we presented a wearable, multi-channel NIRS imaging system that operates with direct LED illumination on the skin and electro-optical sensors for direct detection instead of bulky optical fiber bundles [Piper et al., 2014c]. Based on this, we envision the development of a compact screening device which in its application and cost is more like a modern ultrasound machine as compared to radiological equipment.

List of Figures

1.1 Absorption and scattering of light in tissue. 3
1.2 Challenges of *in vivo* NIR imaging using the example of small animal stroke imaging 4

2.1 Excitation and shifted emission spectra of the NIR fluorophore Cy5.5. 12
2.2 Vascular anatomy of the murine brain 14
2.3 Schematic representation of the surface-stripping idea. 16
2.4 Mathematical background to histogram equalisation and matching. 20
2.5 Example of photon propagation through tissue as calculated from Monte Carlo simulations. 28
2.6 RNOI and histogram approach. 32
2.7 Results: Wavelengths dependence of the algorithm 34
2.8 Monte Carlo simulation results. 35
2.9 Results tissue phantom. 37
2.10 Results *in vivo* imaging I: Implanted capsule and increasing background fluorescence. 38
2.11 Subtraction results depending on the choice of the region not of interest (RNOI). 39
2.12 Results *in vivo* imaging II: mouse with stroke. 40

3.1 Schematic of principles behind time-resolved fluorescence imaging. 47
3.2 Block diagram of the parallel work flow for simulating for photon migration as implemented by the MCX software. 49
3.3 Calculation of the sensitivity distribution using the reciprocity theorem [Cristy, 1983]. 53
3.4 Schemes of the simulated, increasingly realistic geometries in a sagittal and coronal view. 55
3.5 MC results without background fluorescence for the semi-infinite and the cylindrical geometry. 57
3.6 MC results for the homogeneous and the heterogeneous mouse head geometry with increasing levels of background fluorescence. 58

4.1 Depth sensitivity and measurement principle in optical tomography. 66

4.2 Dynamic near infrared optical tomography system customized for unilateral mammography studies. 75
4.3 Dynamic optical mammography results for a malignant, a benign and a healthy control case. 81
4.4 Derivation of peak time grouped amplitude (PTA) curves as a function of time to peak (TTP). 84
4.5 Derivation of a reader-independent classification metric based on a peak time grouped amplitude (PTA) analysis for 22 patients. . . . 85
4.6 ROC analysis results. 86

Abbreviations

AIF	arterial input function
ART	algebraic reconstruction technique
AUC	area under the curve
CT	computed tomography
CW	continous-wave
DCE	dynamic contrast-enhanced
DCIS	ductal carcinoma in situ
FA	fibroadenoma
FC	firbocystic changes
FD	frequency domain
FEM	finite element mesh
FLIM	fluorescence lifetime based imaging contrast
FOV	field of view
FRI	fluorescence reflectance imaging
GPU	graphics processing unit
HE	histogram equalisation
HbO	oxygenated hemoglobin
HbR	deoxygenated hemoglobin
ICG	indocyanine green
i.v.	intra venous
IDC	invasive ductal carcinoma
ILC	invasive lobular carcinoma
ILDC	invasive lobular ductal carcinoma
MCX	Monte Carlo eXtreme software
MRI	magnetic resonance imaging
MV	mean value
NIR	near-infrared
NIRF	near-infrared fluorescence
npv	negative predictive value
PA	peak amplitude
PASH	pseudoangiomatous stroma hyperplasia
PET	positron emission tomography
ppv	positive predictive value
PTA	peak time grouped amplitude
RNG	random number generator
RNOI	region not of interest
ROC	receiver operator characteristic
ROI	region of interest
RTE	radiative transfer equation
SD	standard deviation
SMD	standardized mean difference
SNR	signal-to-noise ratio
SPECT	single-photon emission computed tomography
TCSPC	time correlated single photon counting
TD	time-domain
TE	thermo-electrically
TSPF	temporal point spread function
TSVD	truncated singular value decomposition
TTP	time to peak

Bibliography

[Akers et al., 2007] Akers, W., Lesage, F., Holten, D., Achilefu, S., et al. (2007). In vivo resolution of multiexponential decays of multiple near-infrared molecular probes by fluorescence lifetime-gated whole-body time-resolved diffuse optical imaging. *Molecular imaging*, 6(4):237–246.

[Al Abdi et al., 2010] Al Abdi, R. M., Schmitz, C., Ansari, R., Andronica, R., Pei, Y., Xu, Y., Graber, H., Noor, B., Ahluwalia, M., and Barbour, R. L. (2010). A dual-mode simultaneous bilateral optical imaging system for breast cancer detection. *Presentation at the Conference on Biomedical Optics (Miami, FL, USA, April 11-14, 2010)*.

[Alacam et al., 2008] Alacam, B., Yazici, B., Intes, X., Nioka, S., and Chance, B. (2008). Pharmacokinetic-rate images of indocyanine green for breast tumors using near-infrared optical methods. *Phys Med Biol*, 53(4):837–59.

[Ale et al., 2013] Ale, A., Ermolayev, V., Deliolanis, N. C., and Ntziachristos, V. (2013). Fluorescence background subtraction technique for hybrid fluorescence molecular tomography/x-ray computed tomography imaging of a mouse model of early stage lung cancer. *Journal of biomedical optics*, 18(5):056006–056006.

[Andersson-Engels et al., 1997] Andersson-Engels, S., Klinteberg, C., Svanberg, K., and Svanberg, S. (1997). In vivo fluorescence imaging for tissue diagnostics. *Phys Med Biol*, 42(5):815–24.

[Arizona, 2014] Arizona, U. o. (2014). University of arizona, dept.of mol. cell. biology: http://spectra.arizona.edu.

[Arridge and Schotland, 2009] Arridge, S. and Schotland, J. (2009). Optical tomography: forward and inverse problems. *arXiv preprint arXiv:0907.2586*.

[Arridge, 1999] Arridge, S. R. (1999). Optical tomography in medical imaging. *Inverse problems*, 15(2):R41.

[Arridge et al., 2000] Arridge, S. R., Dehghani, H., Schweiger, M., and Okada, E. (2000). The finite element model for the propagation of light in scattering media: a direct method for domains with nonscattering regions. *Med Phys*, 27(1):252–64.

[Arridge and Hebden, 1997] Arridge, S. R. and Hebden, J. C. (1997). Optical imaging in medicine: Ii. modelling and reconstruction. *Phys Med Biol*, 42(5):841–53.

[Arridge et al., 1995] Arridge, S. R., Hiraoka, M., and Schweiger, M. (1995). Statistical basis for the determination of optical pathlength in tissue. *Physics in medicine and biology*, 40(9):1539.

[Arridge and Schweiger, 1995] Arridge, S. R. and Schweiger, M. (1995). Photon-measurement density functions. part 2: Finite-element-method calculations. *Appl Opt*, 34(34):8026–37.

[Arridge and Schweiger, 1997] Arridge, S. R. and Schweiger, M. (1997). Image reconstruction in optical tomography. *Philos Trans R Soc Lond B Biol Sci*, 352(1354):717–26.

[Arridge et al., 1993] Arridge, S. R., Schweiger, M., Hiraoka, M., and Delpy, D. T. (1993). A finite element approach for modeling photon transport in tissue. *Med Phys*, 20(2 Pt 1):299–309.

[Ballou et al., 2005] Ballou, B., Ernst, L. A., and Waggoner, A. S. (2005). Fluorescence imaging of tumors in vivo. *Curr Med Chem*, 12(7):795–805.

[Barbour et al., 2001] Barbour, R. L., Graber, H. L., Pei, Y., Zhong, S., and Schmitz, C. H. (2001). Optical tomographic imaging of dynamic features of dense-scattering media. *J Opt Soc Am A Opt Image Sci Vis*, 18(12):3018–36.

[Bartrum Jr and Crow, 1984] Bartrum Jr, R. and Crow, H. (1984). Transillumination lightscanning to diagnose breast cancer: a feasibility study. *American Journal of Roentgenology*, 142(2):409–414.

[Bastiaens and Squire, 1999] Bastiaens, P. I. and Squire, A. (1999). Fluorescence lifetime imaging microscopy: spatial resolution of biochemical processes in the cell. *Trends Cell Biol*, 9(2):48–52.

[Becker, 2012] Becker, W. (2012). Fluorescence lifetime imaging–techniques and applications. *J Microsc*, 247(2):119–36.

[Berlier et al., 2003] Berlier, J. E., Rothe, A., Buller, G., Bradford, J., Gray, D. R., Filanoski, B. J., Telford, W. G., Yue, S., Liu, J., Cheung, C. Y., Chang, W., Hirsch, J. D., Beechem, J. M., Haugland, R. P., and Haugland, R. P. (2003). Quantitative comparison of long-wavelength alexa fluor dyes to cy dyes: fluorescence of the dyes and their bioconjugates. *J Histochem Cytochem*, 51(12):1699–712.

[Bloch et al., 2005] Bloch, S., Lesage, F., McIntosh, L., Gandjbakhche, A., Liang, K., and Achilefu, S. (2005). Whole-body fluorescence lifetime imaging of a tumor-targeted near-infrared molecular probe in mice. *J Biomed Opt*, 10(5):054003.

[Boas et al., 2002] Boas, D., Culver, J., Stott, J., and Dunn, A. (2002). Three dimensional monte carlo code for photon migration through complex heterogeneous media including the adult human head. *Optics express*, 10(3):159–170.

[Boas et al., 2001] Boas, D. A., Brooks, D. H., Miller, E. L., DiMarzio, C. A., Kilmer, M., Gaudette, R. J., and Zhang, Q. (2001). Imaging the body with diffuse optical tomography. *Signal Processing Magazine, IEEE*, 18(6):57–75.

[Boas et al., 2004] Boas, D. A., Chen, K., Grebert, D., and Franceschini, M. A. (2004). Improving the diffuse optical imaging spatial resolution of the cerebral hemodynamic response to brain activation in humans. *Opt Lett*, 29(13):1506–8.

[Boas and Dale, 2005] Boas, D. A. and Dale, A. M. (2005). Simulation study of magnetic resonance imaging-guided cortically constrained diffuse optical tomography of human brain function. *Applied optics*, 44(10):1957–1968.

[Boetes et al., 1994] Boetes, C., Barentsz, J. O., Mus, R. D., Van Der Sluis, R., van Erning, L., Hendriks, J., Holland, R., and Ruys, S. (1994). Mr characterization of suspicious breast lesions with a gadolinium-enhanced turboflash subtraction technique. *Radiology*, 193(3):777–781.

[Born and Wolf, 1986] Born, M. and Wolf, E. (1986). Principles of optics: Electromagnetic theory of propagation, interference and diffraction of light. *Sixth corrected edition, Pergamon Press, 1986*, 1.

[Bourayou et al., 2008] Bourayou, R., Boeth, H., Benav, H., Betz, T., Lindauer, U., Nierhaus, T., Klohs, J., Wunder, A., Dirnagl, U., and Steinbrink, J. (2008). Fluorescence tomography technique optimized for noninvasive imaging of the mouse brain. *J Biomed Opt*, 13(4):041311.

[Boverman et al., 2005] Boverman, G., Miller, E. L., Li, A., Zhang, Q., Chaves, T., Brooks, D. H., and Boas, D. A. (2005). Quantitative spectroscopic diffuse optical tomography of the breast guided by imperfect a priori structural information. *Physics in medicine and biology*, 50(17):3941.

[Brackmann, 2000] Brackmann, U. (2000). Laser dyes. *Göttingen (Germany): Lambda Physik AG. D-37079*.

[Brooksby et al., 2003] Brooksby, B. A., Dehghani, H., Pogue, B. W., and Paulsen, K. D. (2003). Near-infrared (nir) tomography breast image reconstruction with a priori structural information from mri: algorithm development for reconstructing heterogeneities. *Selected Topics in Quantum Electronics, IEEE Journal of*, 9(2):199–209.

[Burgess et al., 2008] Burgess, S. A., Bouchard, M. B., Yuan, B., and Hillman, E. M. (2008). Simultaneous multiwavelength laminar optical tomography. *Opt Lett*, 33(22):2710–2.

[Calvetti et al., 2000] Calvetti, D., Morigi, S., Reichel, L., and Sgallari, F. (2000). Tikhonov regularization and the l-curve for large discrete ill-posed problems. *Journal of computational and applied mathematics*, 123(1):423–446.

[Cardillo, 2008] Cardillo, G. (2008). Roc curve: compute a receiver operating characteristics curve. *http://www.mathworks.com/matlabcentral/fileexchange/19950*.

[Carlsen, 1982] Carlsen, E. (1982). Transillumination light scanning. *Diagn. Imaging*, 4(60):28–33.

[Carp et al., 2013] Carp, S. A., Sajjadi, A. Y., Wanyo, C. M., Fang, Q., Specht, M. C., Schapira, L., Moy, B., Bardia, A., Boas, D. A., and Isakoff, S. J. (2013). Hemodynamic signature of breast cancer under fractional mammographic compression using a dynamic diffuse optical tomography system. *Biomedical Optics Express*, 4(12):2911–2924.

[Carter et al., 1989] Carter, C. L., Allen, C., and Henson, D. E. (1989). Relation of tumor size, lymph node status, and survival in 24,740 breast cancer cases. *Cancer*, 63(1):181–7.

[Castro Lima et al., 2011] Castro Lima, V., Rodrigues, E. B., Nunes, R. P., Sallum, J. F., Farah, M. E., and Meyer, C. H. (2011). Simultaneous confocal scanning laser ophthalmoscopy combined with high-resolution spectral-domain optical coherence tomography: a review. *J Ophthalmol*, 2011:743670.

[Cerussi et al., 2001] Cerussi, A. E., Berger, A. J., Bevilacqua, F., Shah, N., Jakubowski, D., Butler, J., Holcombe, R. F., and Tromberg, B. J. (2001). Sources of absorption and scattering contrast for near-infrared optical mammography. *Academic radiology*, 8(3):211–218.

[Chaudhari et al., 2009] Chaudhari, A. J., Ahn, S., Levenson, R., Badawi, R. D., Cherry, S. R., and Leahy, R. M. (2009). Excitation spectroscopy in multispectral optical fluorescence tomography: methodology, feasibility and computer simulation studies. *Phys Med Biol*, 54(15):4687–704.

[Choi et al., 2004] Choi, J., Wolf, M., Toronov, V., Wolf, U., Polzonetti, C., Hueber, D., Safonova, L. P., Gupta, R., Michalos, A., and Mantulin, W. (2004). Noninvasive determination of the optical properties of adult brain: near-infrared spectroscopy approach. *Journal of biomedical optics*, 9(1):221–229.

[Clark et al., 1987] Clark, G. M., Sledge, G. W., J., Osborne, C. K., and McGuire, W. L. (1987). Survival from first recurrence: relative importance of prognostic factors in 1,015 breast cancer patients. *J Clin Oncol*, 5(1):55–61.

[Corlu et al., 2007] Corlu, A., Choe, R., Durduran, T., Rosen, M. A., Schweiger, M., Arridge, S. R., Schnall, M. D., and Yodh, A. G. (2007). Three-dimensional in vivo fluorescence diffuse optical tomography of breast cancer in humans. *Opt Express*, 15(11):6696–716.

[Cristy, 1983] Cristy, M. (1983). Applying the reciprocal dose principle to heterogeneous phantoms: practical experience from monte carlo studies. *Phys Med Biol*, 28(11):1289–303.

[Cubeddu et al., 2002] Cubeddu, R., Comelli, D., D'Andrea, C., Taroni, P., and Valentini, G. (2002). Time-resolved fluorescence imaging in biology and medicine. *Journal of Physics D: Applied Physics*, 35(9):R61.

[Cutler, 1929] Cutler, M. (1929). Transillumination as an aid in the diagnosis of breast lesions. *Surgery, gynecology and obstetrics*, 48:721–729.

[Das et al., 1997] Das, B., Liu, F., and Alfano, R. (1997). Time-resolved fluorescence and photon migration studies in biomedical and model random media. *Reports on progress in Physics*, 60(2):227.

[Dehghani et al., 2003] Dehghani, H., Pogue, B. W., Poplack, S. P., and Paulsen, K. D. (2003). Multiwavelength three-dimensional near-infrared tomography of the breast: initial simulation, phantom, and clinical results. *Applied Optics*, 42(1):135–145.

[Delpy et al., 1988] Delpy, D. . T., Cope, M., Van der Zee, P., Arridge, S., Wray, S., and Wyatt, J. (1988). Estimation of optical pathlength through tissue from direct time of flight measurement. *Physics in medicine and biology*, 33(12):1433.

[DeSantis et al., 2011] DeSantis, C., Siegel, R., Bandi, P., and Jemal, A. (2011). Breast cancer statistics, 2011. *CA Cancer J Clin*, 61(6):409–18.

[Desmettre et al., 2000] Desmettre, T., Devoisselle, J., and Mordon, S. (2000). Fluorescence properties and metabolic features of indocyanine green (icg) as related to angiography. *Survey of ophthalmology*, 45(1):15–27.

[Dietzel et al., 2011] Dietzel, M., Baltzer, P., Vag, T., Zoubi, R., Gröschel, T., Burmeister, H., Gajda, M., Runnebaum, I., and Kaiser, W. (2011). Potential of mr mammography to predict tumor grading of invasive breast cancer. *RoFo: Fortschritte auf dem Gebiete der Röntgenstrahlen und der Nuklearmedizin*, 183(9):826–833.

[Duda et al., 2012] Duda, R. O., Hart, P. E., and Stork, D. G. (2012). *Pattern classification*. John Wiley & Sons, 2 edition.

[Ebert and Grosenick, 2013] Ebert, B. and Grosenick, D. (2013). Optical imaging of breast tumors and of gastrointestinal cancer by laser-induced fluorescence. *Recent Results Cancer Res*, 187:331–50.

[Egawa et al., 2013] Egawa, G., Natsuaki, Y., Miyachi, Y., and Kabashima, K. (2013). Three-dimensional imaging of epidermal keratinocytes and dermal vasculatures using two-photon microscopy. *J Dermatol Sci*, 70(2):143–5.

[Eggebrecht et al., 2012] Eggebrecht, A. T., White, B. R., Ferradal, S. L., Chen, C., Zhan, Y., Snyder, A. Z., Dehghani, H., and Culver, J. P. (2012). A quantitative spatial comparison of high-density diffuse optical tomography and fmri cortical mapping. *Neuroimage*, 61(4):1120–8.

[Einstein, 1905] Einstein, A. (1905). Über die von der molekularkinetischen theorie der wärme geforderte bewegung von in ruhenden flüssigkeiten suspendierten teilchen. *Annalen der physik*, 322(8):549–560.

[Elliott et al., 2012] Elliott, J. T., Diop, M., Lee, T.-Y., and Lawrence, K. S. (2012). Model-independent dynamic constraint to improve the optical reconstruction of regional kinetic parameters. *OPTICS LETTERS*, 37(13):2571–2573.

[Elmore et al., 2005] Elmore, J. G., Armstrong, K., Lehman, C. D., and Fletcher, S. W. (2005). Screening for breast cancer. *JAMA*, 293(10):1245–56.

[Fang and Boas, 2009] Fang, Q. and Boas, D. A. (2009). Monte carlo simulation of photon migration in 3d turbid media accelerated by graphics processing units. *Opt Express*, 17(22):20178–90.

[Firbank et al., 1997] Firbank, M., Okada, E., and Delpy, D. (1997). Investigation of the effect of discrete absorbers upon the measurement of blood volume with near-infrared spectroscopy. *Physics in medicine and biology*, 42-3:465.

[Flexman et al., 2011] Flexman, M. L., Khalil, M. A., Al Abdi, R., Kim, H. K., Fong, C. J., Desperito, E., Hershman, D. L., Barbour, R. L., and Hielscher, A. H. (2011). Digital optical tomography system for dynamic breast imaging. *J Biomed Opt*, 16(7):076014.

[Flexman et al., 2013] Flexman, M. L., Kim, H. K., Gunther, J. E., Lim, E. A., Alvarez, M. C., Desperito, E., Kalinsky, K., Hershman, D. L., and Hielscher, A. H. (2013). Optical biomarkers for breast cancer derived from dynamic diffuse optical tomography. *J Biomed Opt*, 18(9):096012.

[Floery et al., 2005] Floery, D., Helbich, T. H., Riedl, C. C., Jaromi, S., Weber, M., Leodolter, S., and Fuchsjaeger, M. H. (2005). Characterization of benign and malignant breast lesions with computed tomography laser mammography (ctlm): initial experience. *Investigative radiology*, 40(6):328–335.

[Gao et al., 2005] Gao, M., Lewis, G., Turner, G. M., Soubret, A., and Ntziachristos, V. (2005). Effects of background fluorescence in fluorescence molecular tomography. *Applied optics*, 44(26):5468–5474.

[Gaudette et al., 2000] Gaudette, R. J., Brooks, D. H., DiMarzio, C. A., Kilmer, M. E., Miller, E. L., Gaudette, T., and Boas, D. A. (2000). A comparison study of linear reconstruction techniques for diffuse optical tomographic imaging of absorption coefficient. *Physics in medicine and biology*, 45(4):1051.

[Gerster et al., 2003] Gerster, E., Ecker, I., Lorch, S., Hahn, C., Menzel, S., and Unger, P. (2003). Orange-emitting frequency-doubled gaassb/gaas semiconductor disk laser. *J. Appl. Phys.*, 94:7397–7401.

[Gibson et al., 2005] Gibson, A. P., Hebden, J. C., and Arridge, S. R. (2005). Recent advances in diffuse optical imaging. *Phys Med Biol*, 50(4):R1–43.

[Gonzalez and Woods, 2002] Gonzalez, R. C. and Woods, R. E. (2002). Digital image processing, 2nd. *SL: Prentice Hall*, 2.

[Gonzalez et al., 2004] Gonzalez, R. C., Woods, R. E., and Eddins, S. L. (2004). *Digital image processing using MATLAB*. Pearson Education India.

[Graber and Barbour, 2012] Graber, H. L. and Barbour, R. L. (2012). Carbogen inspiration enhances hemodynamic contrast in the cancerous breast. *Conference on Biomedical Optics (Miami, FL USA, April 29 - May 2, 2012)*.

[Graber et al., 1993] Graber, H. L., Chang, J.-H., Lubowsky, J., Aronson, R., and Barbour, R. L. (1993). Near-infrared absorption imaging of dense scattering media by steady-state diffusion tomography. *OE/LASE'93: Optics, Electro-Optics, & Laser Applications in Science& Engineering*, pages 372–386.

[Graves et al., 2005] Graves, E. E., Yessayan, D., Turner, G., Weissleder, R., and Ntziachristos, V. (2005). Validation of in vivo fluorochrome concentrations measured using fluorescence molecular tomography. *J Biomed Opt*, 10(4):44019.

[Grosenick et al., 2003] Grosenick, D., Moesta, K. T., Wabnitz, H., Mucke, J., Stroszczynski, C., Macdonald, R., Schlag, P. M., and Rinneberg, H. (2003). Time-domain optical mammography: initial clinical results on detection and characterization of breast tumors. *Applied optics*, 42(16):3170–3186.

[Gu et al., 2013] Gu, L., Hall, D. J., Qin, Z., Anglin, E., Joo, J., Mooney, D. J., Howell, S. B., and Sailor, M. J. (2013). In vivo time-gated fluorescence imaging with biodegradable luminescent porous silicon nanoparticles. *Nature communications*, 4 Jg.

[Habermehl et al., 2012] Habermehl, C., Holtze, S., Steinbrink, J., Koch, S. P., Obrig, H., Mehnert, J., and Schmitz, C. H. (2012). Somatosensory activation of two fingers can be discriminated with ultrahigh-density diffuse optical tomography. *Neuroimage*, 59(4):3201–3211.

[Habermehl et al., 2014] Habermehl, C., Steinbrink, J., Müller, K.-R., and Haufe, S. (2014). Optimizing the regularization for image reconstruction of cerebral diffuse optical tomography. *submitted to Journal of Neural Engineering*.

[Hagen et al., 2009] Hagen, A., Grosenick, D., Macdonald, R., Rinneberg, H., Burock, S., Warnick, P., Poellinger, A., and Schlag, P. M. (2009). Late-fluorescence mammography assesses tumor capillary permeability and differentiates malignant from benign lesions. *Optics express*, 17(19):17016–17033.

[Hall et al., 2004] Hall, D., Ma, G., Lesage, F., and Wang, Y. (2004). Simple time-domain optical method for estimating the depth and concentration of a fluorescent inclusion in a turbid medium. *Opt Lett*, 29(19):2258–60.

[Hansen, 1998] Hansen, P. C. (1998). *Rank-deficient and discrete ill-posed problems: numerical aspects of linear inversion*, volume 4. Siam.

[Hansen, 1999] Hansen, P. C. (1999). *The L-curve and its use in the numerical treatment of inverse problems*. IMM, Department of Mathematical Modelling, Technical Universityof Denmark.

[Harkonen et al., 2007] Harkonen, A., Rautiainen, J., Guina, M., Konttinen, J., Tuomisto, P., Orsila, L., Pessa, M., and Okhotnikov, O. G. (2007). High power frequency doubled gainnas semiconductor disk laser emitting at 615 nm. *Opt Express*, 15(6):3224–9.

[Hebden et al., 1997] Hebden, J. C., Arridge, S. R., and Delpy, D. T. (1997). Optical imaging in medicine: I. experimental techniques. *Phys Med Biol*, 42(5):825–40.

[Hebden and Delpy, 1994] Hebden, J. C. and Delpy, D. T. (1994). Enhanced time-resolved imaging with a diffusion model of photon transport. *Opt Lett*, 19(5):311–3.

[Hebden et al., 2002] Hebden, J. C., Gibson, A., Yusof, R. M., Everdell, N., Hillman, E. M., Delpy, D. T., Arridge, S. R., Austin, T., Meek, J. H., and Wyatt, J. S. (2002). Three-dimensional optical tomography of the premature infant brain. *Physics in medicine and biology*, 47(23):4155.

[Hecht and Zajac, 1998] Hecht, E. and Zajac, A. (1998). Optics, ed. *MA: Addison-Wesley Publishing Company*.

[Henyey and Greenstein, 1941] Henyey, L. G. and Greenstein, J. L. (1941). Diffuse radiation in the galaxy. *The Astrophysical Journal*, 93:70–83.

[Heuser, 1990] Heuser, H. (1990). Lehrbuch der analysis, teil 1, bg teubner, 5. *Auflage, Stuttgart*.

[Hielscher et al., 1998] Hielscher, A. H., Alcouffe, R. E., and Barbour, R. L. (1998). Comparison of finite-difference transport and diffusion calculations for photon migration in homogeneous and heterogeneous tissues. *Phys Med Biol*, 43(5):1285–302.

[Hilderbrand and Weissleder, 2010] Hilderbrand, S. A. and Weissleder, R. (2010). Near-infrared fluorescence: application to in vivo molecular imaging. *Current opinion in chemical biology*, 14(1):71–79.

[Hillman, 2007] Hillman, E. M. (2007). Optical brain imaging in vivo: techniques and applications from animal to man. *J Biomed Opt*, 12(5):051402.

[Hillman et al., 2011] Hillman, E. M., Amoozegar, C. B., Wang, T., McCaslin, A. F., Bouchard, M. B., Mansfield, J., and Levenson, R. M. (2011). In vivo optical imaging and dynamic contrast methods for biomedical research. *Philos Transact A Math Phys Eng Sci*, 369(1955):4620–43.

[Hintersteiner et al., 2005] Hintersteiner, M., Enz, A., Frey, P., Jaton, A. L., Kinzy, W., Kneuer, R., Neumann, U., Rudin, M., Staufenbiel, M., Stoeckli, M., Wiederhold, K. H., and Gremlich, H. U. (2005). In vivo detection of amyloid-beta deposits by near-infrared imaging using an oxazine-derivative probe. *Nat Biotechnol*, 23(5):577–83.

[Hintz et al., 2001] Hintz, S. R., Benaron, D. A., Siegel, A. M., Zourabian, A., Stevenson, D. K., and Boas, D. A. (2001). Bedside functional imaging of the premature infant brain during passive motor activation. *Journal of perinatal medicine*, 29(4):335–343.

[Hsu et al., 2006] Hsu, A. R., Hou, L. C., Veeravagu, A., Greve, J. M., Vogel, H., Tse, V., and Chen, X. (2006). In vivo near-infrared fluorescence imaging of integrin alphavbeta3 in an orthotopic glioblastoma model. *Mol Imaging Biol*, 8(6):315–23.

[Hyde et al., 2009] Hyde, D., de Kleine, R., MacLaurin, S. A., Miller, E., Brooks, D. H., Krucker, T., and Ntziachristos, V. (2009). Hybrid fmt-ct imaging of amyloid-beta plaques in a murine alzheimer's disease model. *Neuroimage*, 44(4):1304–11.

[Intes et al., 2004] Intes, X., Maloux, C., Guven, M., Yazici, B., and Chance, B. (2004). Diffuse optical tomography with physiological and spatial a priori constraints. *Physics in medicine and biology*, 49(12):N155.

[Intes et al., 2003] Intes, X., Ripoll, J., Chen, Y., Nioka, S., Yodh, A., and Chance, B. (2003). In vivo continuous-wave optical breast imaging enhanced with indocyanine green. *Medical physics*, 30:1039.

[Jacques et al., 1987] Jacques, S., Alter, C., and Prahl, S. (1987). Angular dependence of hene laser light scattering by human dermis. *Lasers Life Sci*, 1(4):309–333.

[Jacques and Pogue, 2008] Jacques, S. L. and Pogue, B. W. (2008). Tutorial on diffuse light transport. *J Biomed Opt*, 13(4):041302.

[Jähne, 2005] Jähne, B. (2005). *Digitale Bildverarbeitung*, volume 6. Springer.

[Jain, 2001] Jain, R. K. (2001). Normalizing tumor vasculature with anti-angiogenic therapy: a new paradigm for combination therapy. *Nature medicine*, 7(9):987–989.

[Jelzow et al., 2012] Jelzow, A., Wabnitz, H., Obrig, H., Macdonald, R., and Steinbrink, J. (2012). Separation of indocyanine green boluses in the human brain and scalp based on time-resolved in-vivo fluorescence measurements. *J Biomed Opt*, 17(5):057003.

[Jemal et al., 2008] Jemal, A., Siegel, R., Ward, E., Hao, Y., Xu, J., Murray, T., and Thun, M. J. (2008). Cancer statistics, 2008. *CA Cancer J Clin*, 58(2):71–96.

[Jobsis, 1977] Jobsis, F. F. (1977). Noninvasive, infrared monitoring of cerebral and myocardial oxygen sufficiency and circulatory parameters. *Science*, 198(4323):1264–7.

[Kak and Slaney, 1988] Kak, A. C. and Slaney, M. (1988). Principles of computerized tomographic imaging. *IEEE, New York*.

[Kalos and Whitlock, 2008] Kalos, M. H. and Whitlock, P. A. (2008). *Monte carlo methods*. John Wiley & Sons.

[Kaltenbach and Kaschke, 1993] Kaltenbach, J.-M. and Kaschke, M. (1993). Frequency- and time-domain modelling of light transport in random media. *Medical optical tomography: functional imaging and monitoring*, pages 65–86.

[Keren et al., 2008] Keren, S., Gheysens, O., Levin, C. S., and Gambhir, S. S. (2008). A comparison between a time domain and continuous wave small animal optical imaging system. *IEEE Trans Med Imaging*, 27(1):58–63.

[Klohs et al., 2009a] Klohs, J., Baeva, N., Steinbrink, J., Bourayou, R., Boettcher, C., Royl, G., Megow, D., Dirnagl, U., Priller, J., and Wunder, A. (2009a). In vivo near-infrared fluorescence imaging of matrix metalloproteinase activity after cerebral ischemia. *J Cereb Blood Flow Metab*, 29(7):1284–92.

[Klohs et al., 2008] Klohs, J., Grafe, M., Graf, K., Steinbrink, J., Dietrich, T., Stibenz, D., Bahmani, P., Kronenberg, G., Harms, C., Endres, M., Lindauer, U., Greger, K., Stelzer, E. H., Dirnagl, U., and Wunder, A. (2008). In vivo imaging of the inflammatory receptor cd40 after cerebral ischemia using a fluorescent antibody. *Stroke*, 39(10):2845–52.

[Klohs et al., 2009b] Klohs, J., Steinbrink, J., Bourayou, R., Mueller, S., Cordell, R., Licha, K., Schirner, M., Dirnagl, U., Lindauer, U., and Wunder, A. (2009b). Near-infrared fluorescence imaging with fluorescently labeled albumin: a novel method for non-invasive optical imaging of blood-brain barrier impairment after focal cerebral ischemia in mice. *J Neurosci Methods*, 180(1):126–32.

[Klohs et al., 2006] Klohs, J., Steinbrink, J., Nierhaus, T., Bourayou, R., Lindauer, U., Bahmani, P., Dirnagl, U., and Wunder, A. (2006). Noninvasive near-infrared imaging of fluorochromes within the brain of live mice: an in vivo phantom study. *Mol Imaging*, 5(3):180–7.

[Kocsis et al., 2006] Kocsis, L., Herman, P., and Eke, A. (2006). The modified beer-lambert law revisited. *Physics in medicine and biology*, 51(5):N91.

[Koyama et al., 2007] Koyama, Y., Talanov, V. S., Bernardo, M., Hama, Y., Regino, C. A., Brechbiel, M. W., Choyke, P. L., and Kobayashi, H. (2007). A dendrimer-based nanosized contrast agent dual-labeled for magnetic resonance and optical fluorescence imaging to localize the sentinel lymph node in mice. *J Magn Reson Imaging*, 25(4):866–71.

[Kuhl et al., 2008] Kuhl, C. K., Traeber, F., and Schild, H. H. (2008). Whole-body high-field-strength (3.0-t) mr imaging in clinical practice part i. technical considerations and clinical applications1. *Radiology*, 246(3):675–696.

[Kukreti et al., 2008] Kukreti, S., Cerussi, A., Tromberg, B., and Gratton, E. (2008). Intrinsic near-infrared spectroscopic markers of breast tumors. *Dis Markers*, 25(6):281–90.

[Kumar, 2011] Kumar, A. T. (2011). Fluorescence lifetime-based optical molecular imaging. *Molecular Imaging - Methods in Molecular Biology Volume 680*, 12:165–180.

[Kumar et al., 2006] Kumar, A. T., Raymond, S. B., Boverman, G., Boas, D. A., and Bacskai, B. J. (2006). Time resolved fluorescence tomography of turbid media based on lifetime contrast. *Opt Express*, 14(25):12255–70.

[Kumar et al., 2005] Kumar, A. T., Skoch, J., Bacskai, B. J., Boas, D. A., and Dunn, A. K. (2005). Fluorescence-lifetime-based tomography for turbid media. *Opt Lett*, 30(24):3347–9.

[Lakowicz, 2009] Lakowicz, J. R. (2009). *Principles of fluorescence spectroscopy*. Springer.

[Lam et al., 2005] Lam, S., Lesage, F., and Intes, X. (2005). Time domain fluorescent diffuse optical tomography: analytical expressions. *Opt. Express*, 13(7):2263–2275.

[Landsman et al., 1976] Landsman, M., Kwant, G., Mook, G., and Zijlstra, W. (1976). Light-absorbing properties, stability, and spectral stabilization of indocyanine green. *Journal of applied physiology*, 40(4):575–583.

[Laufer et al., 2009] Laufer, J., Zhang, E., Raivich, G., and Beard, P. (2009). Three-dimensional noninvasive imaging of the vasculature in the mouse brain using a high resolution photoacoustic scanner. *Appl Opt*, 48(10):D299–306.

[Leblond et al., 2010] Leblond, F., Davis, S. C., Valdes, P. A., and Pogue, B. W. (2010). Pre-clinical whole-body fluorescence imaging: Review of instruments, methods and applications. *J Photochem Photobiol B*, 98(1):77–94.

[Leff et al., 2008] Leff, D. R., Warren, O. J., Enfield, L. C., Gibson, A., Athanasiou, T., Patten, D. K., Hebden, J., Yang, G. Z., and Darzi, A. (2008). Diffuse optical imaging of the healthy and diseased breast: a systematic review. *Breast cancer research and treatment*, 108(1):9–22.

[Liebert et al., 2012] Liebert, A., Wabnitz, H., and Elster, C. (2012). Determination of absorption changes from moments of distributions of times of flight of photons: optimization of measurement conditions for a two-layered tissue model. *J Biomed Opt*, 17(5):057005.

[Liebert et al., 2003] Liebert, A., Wabnitz, H., Grosenick, D., Moller, M., Macdonald, R., and Rinneberg, H. (2003). Evaluation of optical properties of highly scattering media by moments of distributions of times of flight of photons. *Appl Opt*, 42(28):5785–92.

[Liebert et al., 2006] Liebert, A., Wabnitz, H., Obrig, H., Erdmann, R., Moller, M., Macdonald, R., Rinneberg, H., Villringer, A., and Steinbrink, J. (2006). Non-invasive detection of fluorescence from exogenous chromophores in the adult human brain. *Neuroimage*, 31(2):600–8.

[Lorbeer et al., 2011] Lorbeer, R. A., Heidrich, M., Lorbeer, C., Ramirez Ojeda, D. F., Bicker, G., Meyer, H., and Heisterkamp, A. (2011). Highly efficient 3d fluorescence microscopy with a scanning laser optical tomograph. *Opt Express*, 19(6):5419–30.

[Lu et al., 2013] Lu, Y., Darne, C. D., Tan, I.-C., Wu, G., Wilganowski, N., Robinson, H., Azhdarinia, A., Zhu, B., Rasmussen, J. C., and Sevick-Muraca, E. M. (2013). In vivo imaging of orthotopic prostate cancer with far-red gene reporter fluorescence tomography and in vivo and ex vivo validation. *Journal of Biomedical Optics*, 18(10):101305–101305.

[Lux and Koblinger, 1991] Lux, I. and Koblinger, L. (1991). *Monte Carlo particle transport methods: neutron and photon calculations*, volume 102. CRC press Boca Raton.

[Madden et al., 2013] Madden, K. S., Zettel, M. L., Majewska, A. K., and Brown, E. B. (2013). Brain tumor imaging: live imaging of glioma by two-photon microscopy. *Cold Spring Harb Protoc*, 2013(3).

[Mahmud et al., 2013] Mahmud, M. S., Cadotte, D. W., Vuong, B., Sun, C., Luk, T. W., Mariampillai, A., and Yang, V. X. (2013). Review of speckle and phase variance optical coherence tomography to visualize microvascular networks. *J Biomed Opt*, 18(5):50901.

[Marcu, 2012] Marcu, L. (2012). Fluorescence lifetime techniques in medical applications. *Ann Biomed Eng*, 40(2):304–31.

[Marquardt, 1963] Marquardt, D. W. (1963). An algorithm for least-squares estimation of nonlinear parameters. *Journal of the Society for Industrial & Applied Mathematics*, 11(2):431–441.

[Massoud and Gambhir, 2003] Massoud, T. F. and Gambhir, S. S. (2003). Molecular imaging in living subjects: seeing fundamental biological processes in a new light. *Genes Dev*, 17(5):545–80.

[McCann et al., 2009] McCann, C. M., Waterman, P., Figueiredo, J. L., Aikawa, E., Weissleder, R., and Chen, J. W. (2009). Combined magnetic resonance and fluorescence imaging of the living mouse brain reveals glioma response to chemotherapy. *Neuroimage*, 45(2):360–9.

[MCX and MCXLAB, 2012] MCX and MCXLAB (2012). download. *Fang, Q. and Boas, D. URL http://sf.net/projects/mcx/files*.

[Meisel et al., 2004] Meisel, C., Prass, K., Braun, J., Victorov, I., Wolf, T., Megow, D., Halle, E., Volk, H. D., Dirnagl, U., and Meisel, A. (2004). Preventive antibacterial treatment improves the general medical and neurological outcome in a mouse model of stroke. *Stroke*, 35(1):2–6.

[Moré, 1978] Moré, J. J. (1978). *The Levenberg-Marquardt algorithm: implementation and theory*. Springer.

[Muller et al., 2001] Muller, K., Mika, S., Ratsch, G., Tsuda, K., and Scholkopf, B. (2001). An introduction to kernel-based learning algorithms. *Neural Networks, IEEE Transactions on*, 12(2):181–201.

[Ntziachristos, 2006] Ntziachristos, V. (2006). Fluorescence molecular imaging. *Annu Rev Biomed Eng*, 8:1–33.

[Ntziachristos, 2010] Ntziachristos, V. (2010). Going deeper than microscopy: the optical imaging frontier in biology. *Nature methods*, 7(8):603–614.

[Ntziachristos et al., 2003] Ntziachristos, V., Bremer, C., and Weissleder, R. (2003). Fluorescence imaging with near-infrared light: new technological advances that enable in vivo molecular imaging. *Eur Radiol*, 13(1):195–208. Journal Article Review Germany.

[Ntziachristos et al., 2002] Ntziachristos, V., Tung, C. H., Bremer, C., and Weissleder, R. (2002). Fluorescence molecular tomography resolves protease activity in vivo. *Nat Med*, 8(7):757–60.

[Nvidia, 2007] Nvidia, C. (2007). Compute unified device architecture programming guide. *http://de.scribd.com/doc/6315379/NVIDIA-CUDA-Programming-Guide-20*.

[Ogawa et al., 2009] Ogawa, M., Kosaka, N., Choyke, P. L., and Kobayashi, H. (2009). Tumor-specific detection of an optically targeted antibody combined with a quencher-conjugated neutravidin "quencher-chaser": a dual "quench and chase" strategy to improve target to nontarget ratios for molecular imaging of cancer. *Bioconjug Chem*, 20(1):147–54.

[Østergaard et al., 2013] Østergaard, L., Tietze, A., Nielsen, T., Drasbek, K. R., Mouridsen, K., Jespersen, S. N., and Horsman, M. R. (2013). The relationship between tumor blood flow, angiogenesis, tumor hypoxia, and aerobic glycolysis. *Cancer research*, 73(18):5618–5624.

[O'Sullivan et al., 2012] O'Sullivan, T. D., Cerussi, A. E., Cuccia, D. J., and Tromberg, B. J. (2012). Diffuse optical imaging using spatially and temporally modulated light. *J Biomed Opt*, 17(7):071311.

[Papadimitriou and Woods, 1975] Papadimitriou, J. and Woods, A. (1975). Structural and functional characteristics of the microcirculation in neoplasms. *The Journal of pathology*, 116(2):65–72.

[Papayannis et al., 2013] Papayannis, A. C., Cipher, D., Banerjee, S., and Brilakis, E. S. (2013). Optical coherence tomography evaluation of drug-eluting stents: a systematic review. *Catheter Cardiovasc Interv*, 81(3):481–7.

[Patel et al., 2008] Patel, J. K., Konda, S., Perez, O. A., Amini, S., Elgart, G., and Berman, B. (2008). Newer technologies/techniques and tools in the diagnosis of melanoma. *Eur J Dermatol*, 18(6):617–31.

[Patterson et al., 1989] Patterson, M. S., Chance, B., and Wilson, B. C. (1989). Time resolved reflectance and transmittance for the noninvasive measurement of tissue optical properties. *Applied Optics*, 28(12):2331–2336.

[Pei, 1999] Pei, Y. (1999). Optical tomographic imaging using the finite element method. *Thesis (PhD). POLYTECHNIC UNIVERSITY, Source DAI-B 60/06, p. 2805, Dec 1999, 151 pages. Publication Number: 9936233*.

[Pei et al., 2001] Pei, Y., Graber, H. L., and Barbour, R. L. (2001). Influence of systematic errors in reference states on image quality and on stability of derived information for dc optical imaging. *Applied Optics*, 40(31):5755–5769.

[Pei et al., 2003] Pei, Y., Graber, H. L., and Barbour, R. L. (2003). A fast reconstruction algorithm for implementation of time-series dc optical tomography. *Conference Proceedings: Biomedical Optics, July 2003*, pages 236–245.

[Pei et al., 2006] Pei, Y., Wang, Z., Xu, Y., Graber, H., Monteiro, R., and Barbour, R. (2006). Navi: A problem solving environment (pse) for nirs data analysis. *Fifth Inter-Institute Workshop on Optical Diagnostic Imaging from Bench to Bedside. Bethesda, MD.*

[Perry et al., 2012] Perry, D., Bharara, M., Armstrong, D. G., and Mills, J. (2012). Intra-operative fluorescence vascular angiography: during tibial bypass. *Journal of diabetes science and technology*, 6(1):204.

[Petty and Lo, 2002] Petty, M. A. and Lo, E. H. (2002). Junctional complexes of the blood-brain barrier: permeability changes in neuroinflammation. *Prog Neurobiol*, 68(5):311–23.

[Pierce et al., 2008] Pierce, M. C., Javier, D. J., and Richards-Kortum, R. (2008). Optical contrast agents and imaging systems for detection and diagnosis of cancer. *Int J Cancer*, 123(9):1979–90.

[Piper et al., 2010] Piper, S., Bahmani, P., Klohs, J., Bourayou, R., Brunecker, P., Muller, J., Harhausen, D., Lindauer, U., Dirnagl, U., Steinbrink, J., and Wunder, A. (2010). Non-invasive surface-stripping for epifluorescence small animal imaging. *Biomed Opt Express*, 1(1):97–105.

[Piper et al., 2014a] Piper, S., Elliott, J., Lawrence, K., Poellinger, A., and Schmitz, C. (2014a). Kinetic dot reconstruction of contrast-enhanced optical mammography data for reader-independent lesion detection. *Presentation BW4B.8 at the Conference on Biomedical Optics 2014.*

[Piper et al., 2013a] Piper, S., Fazli, S., and Schmitz, C. (2013a). Reader-independent classification of malignant and benign breast lesions based on delayed icg washout kinetics. *Presentation ETu1C.5 at the European Conferences on Biomedical Optics (Munich, Germany, May 12-16, 2013).*

[Piper et al., 2014b] Piper, S. K., Gosmann, J., Mehnert, J., Betz, T., and Steinbrink, J. (2014b). Towards determining the depth of fluorescent targets by time-domain reflectance imaging. *submitted to Physics in Medicine and Biology.*

[Piper et al., 2013b] Piper, S. K., Habermehl, C., Schmitz, C. H., Kuebler, W. M., Obrig, H., Steinbrink, J., and Mehnert, J. (2013b). Towards whole-body fluorescence imaging in humans. *PloS one*, 8(12):e83749.

[Piper et al., 2014c] Piper, S. K., Krueger, A., Koch, S. P., Mehnert, J., Habermehl, C., Steinbrink, J., Obrig, H., and Schmitz, C. H. (2014c). A wearable multi-channel fnirs system for brain imaging in freely moving subjects. *NeuroImage*, 85:64–71.

[Pisano et al., 2005] Pisano, E. D., Gatsonis, C., Hendrick, E., Yaffe, M., Baum, J. K., Acharyya, S., Conant, E. F., Fajardo, L. L., Bassett, L., D'Orsi, C., Jong, R., Rebner, M., and Digital Mammographic Imaging Screening Trial Investigators, G. (2005). Diagnostic performance of digital versus film mammography for breast-cancer screening. *N Engl J Med*, 353(17):1773–83.

[Poellinger, 2012] Poellinger, A. (2012). Near-infrared imaging of breast cancer using optical contrast agents. *J Biophotonics*, 5(11-12):815–26. Journal Article Germany.

[Poellinger et al., 2011a] Poellinger, A., Burock, S., Grosenick, D., Hagen, A., Ludemann, L., Diekmann, F., Engelken, F., Macdonald, R., Rinneberg, H., and Schlag, P. M. (2011a). Breast cancer: early- and late-fluorescence near-infrared imaging with indocyanine green–a preliminary study. *Radiology*, 258(2):409–16.

[Poellinger et al., 2011b] Poellinger, A., Persigehl, T., Mahler, M., Bahner, M., Ponder, S. L., Diekmann, F., Bremer, C., and Moesta, T. (2011b). Near-infrared imaging of the breast using omocianine as a fluorescent dye: results of a placebo-controlled, clinical, multicenter trial. *Invest Radiol*, 46(11):697–704.

[Pogue and Paulsen, 1998] Pogue, B. W. and Paulsen, K. D. (1998). High-resolution near-infrared tomographic imaging simulations of the rat cranium by use of *a priori* magnetic resonance imaging structural information. *Optics letters*, 23(21):1716–1718.

[Prahl, 2001] Prahl, S. A. (2001). http://omlc.ogi.edu/spectra/hemoglobin/index.html.

[Quaresima et al., 1998] Quaresima, V., Matcher, S. J., and Ferrari, M. (1998). Identification and quantification of intrinsic optical contrast for near-infrared mammography. *Photochem Photobiol*, 67(1):4–14.

[Rasmussen et al., 2009] Rasmussen, J. C., Tan, I., Marshall, M. V., Fife, C. E., Sevick-Muraca, E. M., et al. (2009). Lymphatic imaging in humans with near-infrared fluorescence. *Current opinion in biotechnology*, 20(1):74–82.

[Rice et al., 2013] Rice, W. L., Hou, S., and Kumar, A. T. (2013). Resolution below the point spread function for diffuse optical imaging using fluorescence lifetime multiplexing. *Opt Lett*, 38(12):2038–40.

[Rinneberg et al., 2005] Rinneberg, H., Grosenick, D., Moesta, K. T., Mucke, J., Gebauer, B., Stroszczynski, C., Wabnitz, H., Moeller, M., Wassermann, B., and Schlag, P. M. (2005). Scanning time-domain optical mammography: detection and characterization of breast tumors in vivo. *Technology in cancer research & treatment*, 4(5):483–496.

[Rubinstein and Kroese, 2011] Rubinstein, R. Y. and Kroese, D. P. (2011). *Simulation and the Monte Carlo method*, volume 707. Wiley. com.

[Sassaroli and Fantini, 2004] Sassaroli, A. and Fantini, S. (2004). Comment on the modified beer-lambert law for scattering media. *Physics in Medicine and Biology*, 49(14):N255.

[Schmitz et al., 2013] Schmitz, C., Piper, S., Schneider, P., Volkwein, N., Schreiter, N., and Poellinger, A. (2013). Comparison of extrinsic and intrinsic dynamic contrasts in fast 3d optical mammography. *Presentation ETu1C.4 at the European Conferences on Biomedical Optics (Munich, Germany, May 12-16, 2013).*

[Schmitz et al., 2005] Schmitz, C. H., Klemer, D. P., Hardin, R., Katz, M. S., Pei, Y., Graber, H. L., Levin, M. B., Levina, R. D., Franco, N. A., Solomon, W. B., and Barbour, R. L. (2005). Design and implementation of dynamic near-infrared optical tomographic imaging instrumentation for simultaneous dual-breast measurements. *Appl Opt*, 44(11):2140–53.

[Schnall et al., 2006] Schnall, M. D., Blume, J., Bluemke, D. A., DeAngelis, G. A., DeBruhl, N., Harms, S., Heywang-Köbrunner, S. H., Hylton, N., Kuhl, C. K., and Pisano, E. D. (2006). Diagnostic architectural and dynamic features at breast mr imaging: Multicenter study1. *Radiology*, 238(1):42–53.

[Schneider et al., 2011] Schneider, P., Piper, S., Schmitz, C. H., Schreiter, N. F., Volkwein, N., Ludemann, L., Malzahn, U., and Poellinger, A. (2011). Fast 3d near-infrared breast imaging using indocyanine green for detection and characterization of breast lesions. *Rofo*, 183(10):956–63.

[Schreiter et al., 2013] Schreiter, N. F., Volkwein, N., Schneider, P., Maurer, M. H., Piper, S., Schmitz, C., and Poellinger, A. (2013). Optical imaging of breast cancer using hemodynamic changes induced by valsalva maneuver. *Rofo*, 185(4):358–66.

[Schweiger and Arridge, 1999] Schweiger, M. and Arridge, S. R. (1999). Application of temporal filters to time resolved data in optical tomography. *Physics in medicine and biology*, 44(7):1699.

[Schweiger et al., 1995] Schweiger, M., Arridge, S. R., Hiraoka, M., and Delpy, D. T. (1995). The finite element method for the propagation of light in scattering media: boundary and source conditions. *Med Phys*, 22(11 Pt 1):1779–92.

[Shah et al., 2001] Shah, N., Cerussi, A., Eker, C., Espinoza, J., Butler, J., Fishkin, J., Hornung, R., and Tromberg, B. (2001). Noninvasive functional optical spectroscopy of human breast tissue. *Proceedings of the National Academy of Sciences*, 98(8):4420–4425.

[St Lawrence et al., 2013] St Lawrence, K., Verdecchia, K., Elliott, J., Tichauer, K., Diop, M., Hoffman, L., and Lee, T. (2013). Kinetic model optimization for characterizing tumour physiology by dynamic contrast-enhanced near-infrared spectroscopy. *Physics in medicine and biology*, 58(5):1591.

[Steinbrink et al., 2001] Steinbrink, J., Wabnitz, H., Obrig, H., Villringer, A., and Rinneberg, H. (2001). Determining changes in nir absorption using a layered model of the human head. *Phys Med Biol*, 46(3):879–96.

[Stemmer et al., 2012] Stemmer, N., Mehnert, J., Steinbrink, J., and Wunder, A. (2012). Noninvasive fluorescence imaging in animal models of stroke. *Curr Med Chem*, 19(28):4786–93.

[Tan et al., 2013] Tan, Y., Cao, Z., Sajja, H. K., Lipowska, M., Wang, Y. A., Yang, L., and Jiang, H. (2013). Dot corrected fluorescence molecular tomography using targeted contrast agents for small animal tumor imaging. *Journal of X-ray science and technology*, 21(1):43–52.

[Tichauer et al., 2013] Tichauer, K. M., Holt, R. W., El-Ghussein, F., Davis, S. C., Samkoe, K. S., Gunn, J. R., Leblond, F., and Pogue, B. W. (2013). Dual-tracer background subtraction approach for fluorescent molecular tomography. *Journal of biomedical optics*, 18(1):016003–016003.

[Tromberg et al., 2008] Tromberg, B. J., Pogue, B. W., Paulsen, K. D., Yodh, A. G., Boas, D. A., and Cerussi, A. E. (2008). Assessing the future of diffuse optical imaging technologies for breast cancer management. *Med Phys*, 35(6):2443–51.

[Tsutsui et al., 2003] Tsutsui, S., Kume, M., and Era, S. (2003). Prognostic value of microvessel density in invasive ductal carcinoma of the breast. *Breast Cancer*, 10(4):312–319.

[Turner et al., 2005] Turner, G. M., Zacharakis, G., Soubret, A., Ripoll, J., and Ntziachristos, V. (2005). Complete-angle projection diffuse optical tomography by use of early photons. *Opt Lett*, 30(4):409–11.

[Umezawa et al., 2009] Umezawa, K., Matsui, A., Nakamura, Y., Citterio, D., and Suzuki, K. (2009). Bright, color-tunable fluorescent dyes in the vis/nir region: establishment of new "tailor-made" multicolor fluorophores based on borondipyrromethene. *Chemistry*, 15(5):1096–106.

[Van der Sluis and Van der Vorst, 1990] Van der Sluis, A. and Van der Vorst, H. (1990). Sirt- and cg-type methods for the iterative solution of sparse linear least-squares problems. *Linear Algebra and its Applications*, 130:257–303.

[Van Lancker et al., 1995] Van Lancker, M., Goor, C., Sacre, R., Lamote, J., Van Belle, S., De Coene, N., Roelstraete, A., and Storme, G. (1995). Patterns of axillary lymph node metastasis in breast cancer. *Am J Clin Oncol*, 18(3):267–72.

[Wang and Jacques, 1992] Wang, L. and Jacques, S. L. (1992). Monte carlo modeling of light transport in multi-layered tissues in standard c. Technical report, University of Texas M. D. Anderson Cancer Center 1992.

[Wang et al., 1995] Wang, L., Jacques, S. L., and Zheng, L. (1995). Mcml–monte carlo modeling of light transport in multi-layered tissues. *Comput Methods Programs Biomed*, 47(2):131–46.

[Wang et al., 1997] Wang, L., Jacques, S. L., and Zheng, L. (1997). Conv–convolution for responses to a finite diameter photon beam incident on multi-layered tissues. *Comput Methods Programs Biomed*, 54(3):141–50.

[Weidner et al., 1991] Weidner, N., Semple, J. P., Welch, W. R., and Folkman, J. (1991). Tumor angiogenesis and metastasis-correlation in invasive breast carcinoma. *New England Journal of Medicine*, 324(1):1–8.

[Weinberg, 2007] Weinberg, R. A. (2007). *The biology of cancer*, volume 255. Garland Science New York.

[Weissleder and Pittet, 2008] Weissleder, R. and Pittet, M. J. (2008). Imaging in the era of molecular oncology. *Nature*, 452(7187):580–589.

[Werner et al., 2012] Werner, S. G., Langer, H.-E., Ohrndorf, S., Bahner, M., Schott, P., Schwenke, C., Schirner, M., Bastian, H., Lind-Albrecht, G., Kurtz, B., et al. (2012). Inflammation assessment in patients with arthritis using a novel in vivo fluorescence optical imaging technology. *Annals of the rheumatic diseases*, 71(4):504–510.

[White and Culver, 2010] White, B. R. and Culver, J. P. (2010). Quantitative evaluation of high-density diffuse optical tomography: in vivo resolution and mapping performance. *Journal of biomedical optics*, 15(2):026006–026006–14.

[Wolf et al., 2007] Wolf, M., Ferrari, M., and Quaresima, V. (2007). Progress of near-infrared spectroscopy and topography for brain and muscle clinical applications. *J Biomed Opt*, 12(6):062104.

[Wu et al., 1997] Wu, J., Perelman, L., Dasari, R. R., and Feld, M. S. (1997). Fluorescence tomographic imaging in turbid media using early-arriving photons and laplace transforms. *Proc Natl Acad Sci U S A*, 94(16):8783–8.

[Wunder and Klohs, 2008] Wunder, A. and Klohs, J. (2008). Optical imaging of vascular pathophysiology. *Basic Res Cardiol*, 103(2):182–90.

[Wunder et al., 2005] Wunder, A., Straub, R. H., Gay, S., Funk, J., and Muller-Ladner, U. (2005). Molecular imaging: novel tools in visualizing rheumatoid arthritis. *Rheumatology (Oxford)*, 44(11):1341–9.

[Yalavarthy et al., 2007] Yalavarthy, P. K., Pogue, B. W., Dehghani, H., and Paulsen, K. D. (2007). Weight-matrix structured regularization provides optimal generalized least-squares estimate in diffuse optical tomography. *Medical physics*, 34:2085.

[Yang et al., 2013] Yang, X., Pu, Y., Hsieh, C. L., Ong, C. A., Psaltis, D., and Stankovic, K. M. (2013). Two-photon microscopy of the mouse cochlea in situ for cellular diagnosis. *J Biomed Opt*, 18(3):031104.

[Yoneya et al., 1998] Yoneya, S., Saito, T., Komatsu, Y., Koyama, I., Takahashi, K., and Duvoll-Young, J. (1998). Binding properties of indocyanine green in human blood. *Investigative ophthalmology & visual science*, 39(7):1286–1290.

[Yuan et al., 2009] Yuan, B., Burgess, S. A., Iranmahboob, A., Bouchard, M. B., Lehrer, N., Bordier, C., and Hillman, E. (2009). A system for high-resolution depth-resolved optical imaging of fluorescence and absorption contrast. *Review of Scientific Instruments*, 80(4):043706–043706.

[Zavattini et al., 2006] Zavattini, G., Vecchi, S., Mitchell, G., Weisser, U., Leahy, R. M., Pichler, B. J., Smith, D. J., and Cherry, S. R. (2006). A hyperspectral fluorescence system for 3d in vivo optical imaging. *Phys Med Biol*, 51(8):2029–43.

[Zhang et al., 2011] Zhang, H., Uselman, R. R., and Yee, D. (2011). Exogenous near-infrared fluorophores and their applications in cancer diagnosis: biological and clinical perspectives. *Expert opinion on medical diagnostics*, 5(3):241–251.

[Zweig and Campbell, 1993] Zweig, M. H. and Campbell, G. (1993). Receiver-operating characteristic (roc) plots: a fundamental evaluation tool in clinical medicine. *Clinical chemistry*, 39(4):561–577.

Danksagung

Ich möchte allen ganz herzlich danken, die mich betreuend, konstruktiv und motivierend während der gesamten Promotionszeit unterstützt haben und ich bedanke ich mich bei der Charité Universitätsmedizin Berlin für die finanzielle Förderung zum Abschluss der Promotion.
Ein besonderer Dank gilt Herrn Prof. Dr. rer. nat. Klaus-Robert Müller für sein interdisziplinäres Interesse und seine Bereitschaft diese Arbeit zu betreuen sowie seiner freundlichen Unterstützung in allen Belangen. Dr. rer. nat. Jens Steinbrink hat meine Arbeit von Seiten der optischen Bildgebung der Charité Berlin betreut und wesentlich beeinflusst. Durch sein Vertrauen und seine breite wissenschaftliche Förderung konnte ich eigene Ideen ausprobieren und lernte selbstbewußt auf internationalen Konferenzen aufzutreten. Dafür bin ich ihm sehr dankbar. Ein weiterer herzlicher Dank gilt Herrn Prof. Dr. med. Hellmuth Obrig für seine Bereitschaft meine Doktorarbeit als externer Gutachter zu evaluieren sowie die großartigen Zusammenarbeit und Unterstützung bei der Umsetzung der Ganzkörperfluoreszenz am Menschen.
Für das ausgezeichnete Arbeitsklima möchte ich mich bei der ganzen NIRS-Gruppe an der Charité bedanken insbesondere nochmal bei Jens Steinbrink, sowie Christina Habermehl, Christoph Schmitz, Jan Mehnert, Arne Krüger und Stephan Paul Koch.
Ganz herzlich möchte ich mich auch bei den Kollegen aus der experimentellen Neurologie der Charité für die exzellente Zusammenarbeit am Kleintier-Fluoreszenz-Imager und die Versorgung der Versuchstiere bedanken: Jan Klohs, Andreas Wunder, Peyman Bahmani, Riad Bourayou, Denise Harrhausen und Jochen Müller. Peter Brunecker danke ich sehr für die Hilfe bei der Implementierung der Histogramm-Anpassung.
Des Weiteren gilt ein großer Dank Jan Gossmann für die Installation der MCX Software und die Hilfe bei den zeitaufgelösten Simulationen.
Bei den Kollegen aus der Radiologie der Charité, Alexander Pöllinger, Paul Schneider, Nils Schreiter und Nassia Volkwein möchte ich mich besonders herzlich für ihr enormes Engagement und die enge, freundschaftliche Zusammenarbeit bei dem Projekt der kontrastmittelgestützten optischen Mammographie bedanken.
Genauso herzlich möchte ich mich bei Daniel Bartz, Siamac Fazli und Benjamin Blankertz für motivierende Diskussionen und die Unterstützung bei der Umsetzung von weiterführenden Klassifizierungsansätzen in der optischen Mammographie bedanken.
Schließlich gilt ein besonders herzlicher Dank meinen lieben Eltern und Schwiegereltern für die Betreuung meiner Söhne während arbeitsintensiver Phasen und während Konferenzaufenthalten. Meinen Geschwistern Franz, Theodor und Pauline sowie meinen Freunden Daniel Bartz, Eike und Nadin Middell, Leandro Oteri und Christoph Schmitz danke ich für das abschnittsweise Korrekturlesen meiner Arbeit.
Abschließend möchte ich meinem geliebten Ehemann Mike für sein Vertrauen, sein Verständnis und den Rückhalt in jeder Lebenslage danken.